



## 저작자표시-비영리-변경금지 2.0 대한민국

이용자는 아래의 조건을 따르는 경우에 한하여 자유롭게

- 이 저작물을 복제, 배포, 전송, 전시, 공연 및 방송할 수 있습니다.

다음과 같은 조건을 따라야 합니다:



저작자표시. 귀하는 원저작자를 표시하여야 합니다.



비영리. 귀하는 이 저작물을 영리 목적으로 이용할 수 없습니다.



변경금지. 귀하는 이 저작물을 개작, 변형 또는 가공할 수 없습니다.

- 귀하는, 이 저작물의 재이용이나 배포의 경우, 이 저작물에 적용된 이용허락조건을 명확하게 나타내어야 합니다.
- 저작권자로부터 별도의 허가를 받으면 이러한 조건들은 적용되지 않습니다.

저작권법에 따른 이용자의 권리는 위의 내용에 의하여 영향을 받지 않습니다.

이것은 [이용허락규약\(Legal Code\)](#)을 이해하기 쉽게 요약한 것입니다.

[Disclaimer](#)

工學博士學位論文

**Fabrication of Polyaniline/Organic • Inorganic Composites  
for Supercapacitor Electrodes**

폴리아닐린/유기물 • 무기물 복합체 제조와 이의 슈퍼커패시터  
전극으로의 응용

2016年 2月

서울대학교 大學院

化學生物工學部

金 玟 奎

**Fabrication of Polyaniline/Organic • Inorganic Composites  
for Supercapacitor Electrodes**

폴리아닐린/유기물 • 무기물 복합체 제조와 이의 슈퍼커패시터  
전극으로의 응용

指導教授: 張 正 植

이 論文을 工學博士 學位論文으로 提出함

2015年 11月

서울대학교 大學院

化學生物工學部

金 玟 奎

金玟奎의 工學博士 學位論文을 認准함

2015年 11月

委 員 長 \_\_\_\_\_ (인)

副委員長 \_\_\_\_\_ (인)

委 員 \_\_\_\_\_ (인)

委 員 \_\_\_\_\_ (인)

委 員 \_\_\_\_\_ (인)

**Fabrication of Polyaniline/Organic • Inorganic Composites  
for Supercapacitor Electrodes**

by

Minkyu Kim

Submitted to the Graduate School of Seoul National University

in Partial Fulfillment of the Requirements

for the Degree of Doctor of Philosophy

February, 2016

Thesis Adviser: Jyongsik Jang



## ABSTRACT

A supercapacitor has widely been utilized in diverse vehicles needing rapid energy delivery because of its high power density: within automobile, trams, light-rails, and cranes. As smaller forms, they have also been utilized as memory backup for static random-access memory. Materials used for supercapacitor electrode possess their pros and cons. For example, carbon materials show a good cycling stability, but specific capacitance is relatively low. In the case of conducting polymers (CPs), in contrast to carbon materials, they possess high specific capacitance, but the cycling stability is relatively poor due to their poor mechanical strength. Thus, large efforts have been made to fabricate supercapacitor with high capacitance and good cycling stability.

In this dissertation, three different polyaniline (PANI)/organic • inorganic composites were prepared using self-stabilized dispersion polymerization (SSDP) method to achieve supercapacitors with high capacitance and good electrochemical stability. First, PANI/silicon dioxide ( $\text{SiO}_2$ ) nanocomposite was fabricated by SSDP method. Produced PANI/ $\text{SiO}_2$  nanocomposite exhibited improved electrochemical performances (specific capacitance: *ca.* 305 F g<sup>-1</sup>, cycling stability: maintaining 72 % of initial gravimetric capacitance

after 500 cycles) compared with PANI/SiO<sub>2</sub> nanocomposite synthesized by conventional polymerization method and other previously reported PANI nanomaterials owing to high electrical conductivity (*ca.* 25.6 S cm<sup>-1</sup>), large specific surface area (*ca.* 170 m<sup>2</sup> g<sup>-1</sup>), and improved crystallinity. Second, PANI/ molybdenum disulfide (MoS<sub>2</sub>) nanocomposite, synthesized by SSDP method, showed enhanced specific capacitance (*ca.* 400 F g<sup>-1</sup>) in comparison with both PANI (*ca.* 232 F g<sup>-1</sup>) and MoS<sub>2</sub> nanosheet (*ca.* 3 F g<sup>-1</sup>) due to high electrical conductivity (*ca.* 28.6 S cm<sup>-1</sup>) and pseudo capacitive characteristics of PANI and MoS<sub>2</sub>. Additionally, PANI/MoS<sub>2</sub> nanosheet exhibited good cycling stability (84 % after 500 cycles) due to honeycomb-like structured PANI on MoS<sub>2</sub> nanosheet and incorporation of MoS<sub>2</sub> nanosheet possessing good mechanical properties. Lastly, PANI/reduced graphene oxide (RGO) film was fabricated through solution processing for highly scalable and flexible supercapacitor electrodes. Produced PANI/RGO film exhibited extremely high electrical conductivity of *ca.* 906 S cm<sup>-1</sup> due to improved crystallinity. In the electrochemical tests, PANI/RGO film exhibited enhanced capacitance (*ca.* 431 F g<sup>-1</sup>) and cycling stability (74 % after after 500 cycles) in comparison with

pure PANI film (specific capacitance: *ca.* 256 F g<sup>-1</sup>, cycling stability: 60 % after 500 cycles). The PANI/RGO film also demonstrated excellent performance ability as a scalable and flexible electrode material. The strategies and specific synthetic methods described here can be useful tool for fabricating supercapacitor electrodes with high capacitance and good electrochemical stability.

**KEYWORDS:** Polyaniline; Silicon dioxide; Molybdenum disulfide; Graphene; Composite; Self-stabilized dispersion polymerization; Supercapacitors

**STUDENT NUMBER:** 2011–21015

## **List of Abbreviations**

Ag : silver

AgCl : silver chloride

APS : ammonium persulfate

Ar : argon

BET : Brunauer–Emmett–Teller

C<sub>area</sub> : area capacitance

CHCl<sub>3</sub> : chloroform

C<sub>m</sub> : gravimetric capacitance

CP : conducting polymer

CP-MAS : cross-polarization and magic-angle spinning

CSA : (±)-10-camphorsulfonic acid

Cu : copper

CV : cyclic voltammetry

De- : de-doped

EB : emeraldine base

EDL : electrical double layer

EDX : energy dispersive x-ray spectroscopy

ES : emeraldine salt

FE- : Field-Emission

FT-IR : Fourier-transform infrared

GO : graphite oxide

H<sup>+</sup> : proton

H<sub>2</sub>O : water

H<sub>2</sub>O<sub>2</sub> : hydrogen peroxide

H<sub>2</sub>SO<sub>4</sub> : sulfuric acid

HCl : hydrochloric acid

K<sub>2</sub>S<sub>2</sub>O<sub>8</sub> : potassium persulfate

KMnO<sub>4</sub> : potassium permanganate

Mo : molybdenum

MoS<sub>2</sub> : molybdenum disulfide

NaNO<sub>3</sub> : sodium nitrate

Ni : nickel

NMP : N-methyl-2-pyrrolidone

NMR : nuclear magnetic resonance

NP : nanoparticle

P<sub>2</sub>O<sub>5</sub> : phosphorus pentoxide

PANI : polyaniline

PARG : polyaniline/reduced graphene oxide

Pt : platinum

PTFE : poly(tetrafluoroethylene)

R : internal resistance

Re- : re-doped

RGO : reduced graphene oxide

S : sulphur

SEM : scanning electron microscope

SiO<sub>2</sub> : silicon dioxide

SP1 : polyaniline/silicon dioxide nanocomposite synthesized by self-stabilized  
dispersion polymerization

SP2 : polyaniline/silicon dioxide nanocomposite synthesized by conventional  
polymerization

SSDP : self-stabilized dispersion polymerization

TEM : transmission electron microscope

TGA : thermo-gravimetric analysis

XPS : X-ray photoelectron spectra

XRD : X-ray diffraction

## List of Figures

**Figure 1.** a) Schematic of a commercial spirally wound electric double layer (EDL) capacitor C); b) Assembled supercapacitors device; c) A small button cell supercapacitors; d) Specific power against specific energy, also called a Ragone plot, for various electrical energy storage devices. [1].

**Figure 2.** Schematic of two different charge storage mechanisms *via* a) EDL capacitor and b) pseudocapacitor. [2].

**Figure 3.** A typical cyclic voltammetry (CV) curve of polyaniline (PANI) in hydrochloric acid (HCl, pH 1) showing two sets of redox couples. The direction of potential scan is shown with the arrows. [7].

**Figure 4.** a) A schematic illustration of the synthesis of PANI nanofibers. 1) The oxidant (open circles) dopant solution is added into the aniline (solid circles) dopant solution and mixed. 2) A homogenous solution is obtained where all the aniline and oxidant molecules are evenly distributed, thus leading to fast polymerization across the entire solution. 3) PANI nanofibers are formed; b) A photopaper



image of the emblem of Seoul National University, printed with an inkjet printer using PANI–poly(4-styrenesulfonate) aqueous solution as ink; c) A scanning electron microscope (SEM) images of PANI nanomaterials synthesized at various initiator/aniline weight ratios. [8–10].

**Figure 5.** Diagram of the self-stabilized dispersion polymerization (SSDP) of PANI. [17].

**Figure 6.** Illustrations of the sequential steps for synthesis of PANI/SiO<sub>2</sub> nanocomposite.

**Figure 7.** Illustrations of the sequential steps for synthesis of PANI/SiO<sub>2</sub> nanocomposite.

**Figure 8.** FE-SEM images and TEM images (inset) of SP1 with the average size of a) 18 nm, b) 35 nm, c) 63 nm, and d) 130 nm. The scale bars of inset images represent 15 nm.

**Figure 9.** Size distribution histograms of SP1 with different diameters.

**Figure 10.** a) FT-IR spectra, b) XRD patterns, and c) Solid-state <sup>13</sup>C NMR spectra of the EB-state SP1 (red line) and SP2 (blue line).

**Figure 11.** Nitrogen adsorption/desorption isotherms of different sized SP1: 18 nm (red line), 35 nm (green line), 63 nm (black line), and 130 nm (purple line).

**Figure 12.** TEM image of the bulk PANI prepared by conventional polymerization method. Its diameter is *ca.* 1  $\mu\text{m}$ .

**Figure 13.** Cyclic voltammograms of SP1 (18, 35, 63, 130 nm) and SP2 (18 nm) at 30  $\text{mV s}^{-1}$  between 0 and 0.8 V in 1M  $\text{H}_2\text{SO}_4$  solution; b) Galvanostatic charge/discharge curve of SP1 (18 nm) at current density of 2.6  $\text{A g}^{-1}$  in 1M  $\text{H}_2\text{SO}_4$  solution; c) Specific capacitances of SP1 (18 nm) and SP2 (18 nm) as a function of cycle number at a current density of 2.6  $\text{A g}^{-1}$  in 1 M  $\text{H}_2\text{SO}_4$  solution; d) Specific capacitances of SP1 (18, 35, 63, 130 nm) and SP2 (18 nm) at 30  $\text{mV s}^{-1}$  between 0 and 0.8 V in 1M  $\text{H}_2\text{SO}_4$  solution.

**Figure 14.** SEM images of a)  $\text{MoS}_2$  nanosheets and b) PANI/ $\text{MoS}_2$  nanocomposite.

**Figure 15.** Raman spectra of a)  $\text{MoS}_2$  nanosheets, b) PANI, and c) PANI/ $\text{MoS}_2$  nanocomposite.

**Figure 16.** Electrical conductivity of the MoS<sub>2</sub> nanosheets, PANI, and PANI/MoS<sub>2</sub> nanocomposite.

**Figure 17.** SEM image of pure PANI synthesized by SSDP.

**Figure 18.** a) Cyclic voltammograms of MoS<sub>2</sub> nanosheet, PANI, and PANI/MoS<sub>2</sub> nanocomposite at a scan rate of 5 mV s<sup>-1</sup>, b) galvanostatic charge/discharge curves of MoS<sub>2</sub> nanosheet, PANI, and PANI/MoS<sub>2</sub> nanocomposite at a current density of 0.6 A g<sup>-1</sup>, c) gravimetric capacitances of MoS<sub>2</sub> nanosheet, PANI, and PANI/MoS<sub>2</sub> nanocomposite at a current density of 0.6 A g<sup>-1</sup>, and d) cycling stability of MoS<sub>2</sub> nanosheets, PANI, and PANI/MoS<sub>2</sub> nanocomposite at a current density of 0.6 A g<sup>-1</sup>.

**Figure 19.** CV curve of pristine MoS<sub>2</sub> nanosheet at a scan rate of 5 mV s<sup>-1</sup>.

**Figure 20.** Galvanostatic charge/discharge curve of pristine MoS<sub>2</sub> nanosheet at a current density of 0.6 A g<sup>-1</sup>.

**Figure 21.** Schematic illustration of the sequential steps for fabricating large-scale Re-PARG film.

**Figure 22.** Digital camera images of (left) electronic device (10.5 cm x 5.5 cm,

4.7 inch) and (right) Re-PARG film (16 cm x 13 cm, 8 inch) with a ruler below the electronic device and film for scale. The scale bars of ruler represent mm.

**Figure 23.** SEM images of a) Pristine RGO, b) PARG, c) Cross sectional view of Re-PANI film and d) Re-PARG film.

**Figure 24.** TEM images of a) Pristine RGO, b) PARG.

**Figure 25.** a) Raman spectra of GO, RGO, Re-PARG film, De-PARG, PARG and PANI (ES state), b) N 1s XPS spectra of PANI (ES state), PARG, De-PARG and Re-PARG film.

**Figure 26.** TGA curves of RGO, De-PARG 1-3 composites with different weight percentage of De-PANI, and De-PANI.

**Figure 27.** a) Electrical conductivity of Re-PANI film, Re-PARG 1-3 films, and RGO displayed as function of the weight percentage of PANI component; b) XRD patterns of graphite, GO, and RGO; c) XRD patterns of Re-PARG 1-3 films and Re-PANI film.

**Figure 28.** a) TGA curves of Re-PARG 2 powder, as-prepared Re-PARG 2 film and Re-PARG 2 film after storing for 150 days and b) XRD patterns

of as-prepared Re-PARG 2 film and Re-PARG 2 film after storing for 150 days.

**Figure 29.** Schematic representation of interaction between RGO and PANI chains leading to compact packing of the PANI chains with RGO and extensive three-dimensional delocalization of the charge.

**Figure 30.** a) CV curves of Re-PARG film, Re-PANI film and RGO electrodes at a scan rate of  $5 \text{ mV s}^{-1}$  between 0 and 0.8 V in 1M  $\text{H}_2\text{SO}_4$  solution; b) Galvanostatic charge/discharge curves of Re-PARG film, Re-PANI film and RGO electrodes at current density of  $0.45 \text{ A g}^{-1}$  in 1M  $\text{H}_2\text{SO}_4$  solution; c) Gravimetric capacitances of RGO, Re-PANI film and Re-PARG film electrodes at current density of  $0.45 \text{ A g}^{-1}$ ; d) Internal resistances of RGO, Re-PANI film and Re-PARG film electrodes estimated from the IR drop at a current density of  $0.45 \text{ A g}^{-1}$ ; e) Comparison of CV curves between different sized ( $1.2$  and  $36 \text{ cm}^2$ ) Re-PARG film electrodes at a scan rate of  $5 \text{ mV s}^{-1}$ ; f) Cyclic stability of Re-PARG film and Re-PANI film electrodes as a function of cycle number at a current density of  $0.45 \text{ A g}^{-1}$ .

**Figure 31.** a) Digital photographs of flexible Re-PARG film. The top image exhibits the folding characteristics of the film. The bottom images illustrate the high flexibility (bending and twisting) of the film; b) CV curves of Re-PARG film electrodes with two different bending angles of 0 ° and 180 ° at a scan rate of 5 mV s<sup>-1</sup>.

## **List of Tables**

**Table 1.** Weight ratio of the pristine  $\text{SiO}_2$  NPs and PANI/ $\text{SiO}_2$  nanocomposite measured by EDX.

**Table 2.** Electrical conductivities of the PANI/ $\text{SiO}_2$  nanocomposites.

## Table of Contents

<b>Abstract.....</b>	<b>i</b>
<b>List of Abbreviations.....</b>	<b>iv</b>
<b>List of Figures.....</b>	<b>viii</b>
<b>List of Tables.....</b>	<b>xv</b>
<b>Table of Contents.....</b>	<b>xvi</b>
<b>1. INTRODUCTION.....</b>	<b>1</b>
<b>1.1. Background.....</b>	<b>1</b>
1.1.1. Supercapacitors .....	1
1.1.2. PANI.....	5
1.1.2.1. Synthetic methods of PANI.....	5
<b>1.2. Objectives and Outlines.....</b>	<b>10</b>
1.2.1. Objectives.....	10
1.2.2. Outlines .....	10
<b>2. EXPERIMENTAL DETAILS .....</b>	<b>14</b>
<b>2.1. PANI/SiO<sub>2</sub> nanocomposite for supercapacitor electrodes .....</b>	<b>14</b>
2.1.1. Fabrication of PANI/SiO <sub>2</sub> nanocomposite .....	14
2.1.2. Supercapacitors based on PANI/SiO <sub>2</sub> nanocomposites .....	17
<b>2.2. PANI/MoS<sub>2</sub> nanocomposite for supercapacitor electrodes .....</b>	<b>19</b>
2.2.1. Fabrication of PANI/MoS <sub>2</sub> nanocomposite .....	19
2.2.2. Supercapacitor based on PANI/MoS <sub>2</sub> nanocomposite .....	20



<b>2.3. PANI/graphene film for flexible supercapacitor electrodes .....</b>	<b>22</b>
2.3.1. Fabrication of PANI/RGO film .....	22
2.3.2. Flexible supercapacitor based on PANI/RGO film .....	26
 <b>3. RESULTS AND DISCUSSION .....</b>	<b>29</b>
 <b>3.1. PANI/SiO<sub>2</sub> nanocomposite for supercapacitor electrodes .....</b>	<b>29</b>
3.1.1. Fabrication of PANI/SiO <sub>2</sub> nanocomposite .....	29
3.1.2. Supercapacitors based on PANI/SiO <sub>2</sub> nanocomposite .....	44
<b>3.2. PANI/MoS<sub>2</sub> nanocomposite for supercapacitor electrodes .....</b>	<b>50</b>
3.2.1. Fabrication of PANI/MoS <sub>2</sub> nanocomposite .....	50
3.2.2. Supercapacitor based on PANI/MoS <sub>2</sub> nanocomposite .....	57
<b>3.3. PANI/graphene film for flexible supercapacitor electrodes .....</b>	<b>65</b>
3.3.1. Fabrication of PANI/RGO film .....	65
3.3.2. Flexible supercapacitor based on PANI/RGO film .....	88
 <b>4. CONCLUSIONS .....</b>	<b>99</b>
 <b>REFERENCES .....</b>	<b>103</b>

# **1. INTRODUCTION**

## **1.1. Background**

### **1.1.1. Supercapacitors**

A supercapacitors have widely been utilized in diverse vehicles needing rapid energy delivery because of its high power density (Figure 1) [1]: within automobile, trams, light-rails, and cranes. As smaller forms, they have also been utilized as memory backup for static random-access memory. Supercapacitors can be classified into two types depending on their energy storage mechanisms: electric double layer (EDL) capacitor and pseudocapacitor (Figure 2) [1,2]. EDL capacitor stores electrical energy by electrostatically charging charge ions in electrical double layers generated on electrode surface. As electrode material for EDL capacitor, various carbon materials such as activated carbons and graphene have been employed. In case of pseudocapacitor, it stores electrical energy by charging the electron in the electrode through the fast reversible redox reaction. CPs (e.g., PANI, polypyrrole, and polythiophene), transition metal sulfides (e.g., MoS<sub>2</sub>, copper monosulfide, and nickel sulfide), transition metal oxides (e.g., manganese dioxide, cobalt oxide, and nickel oxide) belong to pseudocapacitor electrode material. Materials used for EDL capacitor and pseudocapacitor possess their pros and cons. For example, carbon materials show a good cycling stability

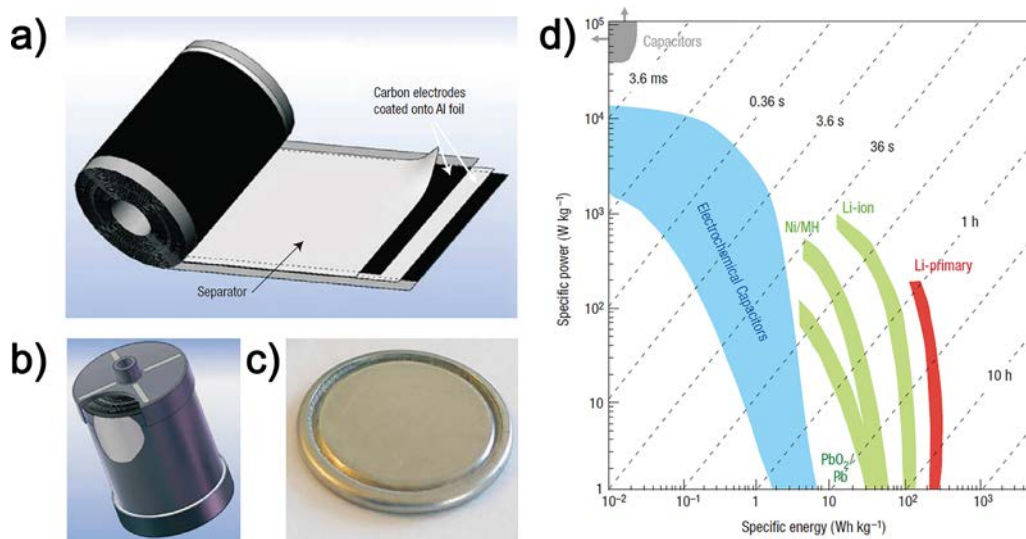


**Figure 1.** a) Schematic of a commercial spirally wound electric double layer (EDL) capacitor C); b) Assembled supercapacitors device; c) A small button cell supercapacitors; d) Specific power against specific energy, also called a Ragone plot, for various electrical energy storage devices. [1].

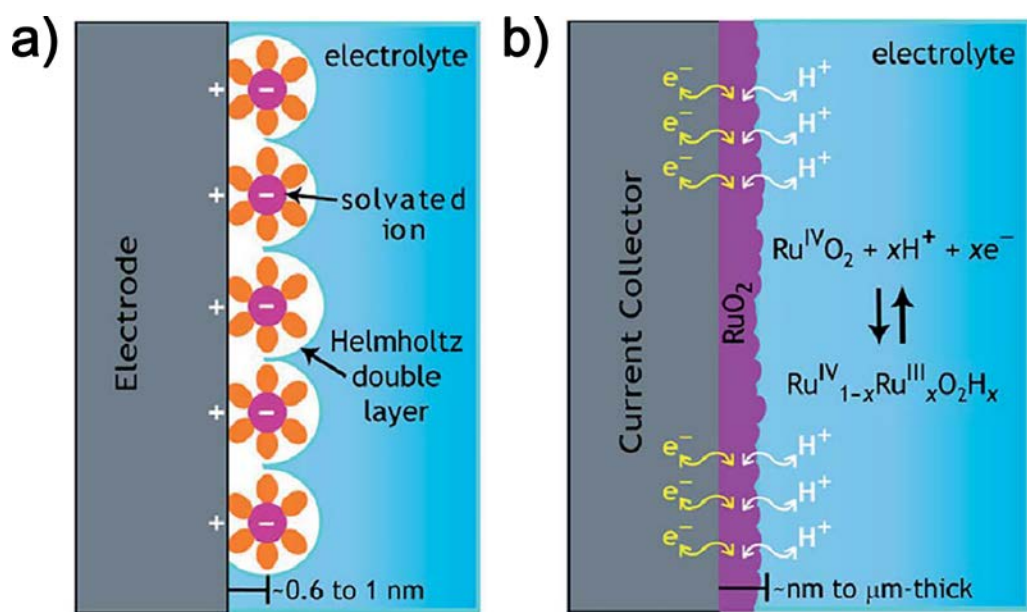


**Figure 2.** Schematic of two different charge storage mechanisms *via* a) EDL capacitor and b) pseudocapacitor. [2].

owing to its good mechanical properties, but specific capacitance is relatively low. In the cases of CPs, in contrast to carbon materials, they possess high specific capacitance, but cycling stability is relatively poor due to their poor mechanical strength [1,2]. Thus, large efforts have been made to fabricate supercapacitor with high capacitance and good cycling stability [1–6].

To achieve large capacitances from electrode materials, following three factors are needed to be considered: 1) energy storage-mechanisms. As described above, pseudo capacitive materials can obtain higher specific capacitances than EDL capacitive materials because larger charge ions can react with pseudo capacitive materials than EDL capacitive materials. 2) specific surface area. 3) electrical conductivity. Meanwhile, following factors must be considered to obtain good cycling stability from electrodes: 1) mechanical properties. 2) morphology. For CPs, they are repeatedly swelled and shrunk during cycling stability test, leading to cracking and breaking of polymer chains, gradual loss in electrical conductivity, and decrease in capacitance. In the case swelling/shrinkage volume is insufficient, the cracking and breaking of polymer chains accelerate, leading to rapid decrease in specific capacitance. Therefore, sufficient void volume must be needed to improve electrochemical stability of electrodes [1].

### 1.1.2. PANI

The PANI, a typical CP, has attracted great attention as supercapacitor electrode materials due to their fascinating properties such as pseudo capacitive characteristic, high electrical conductivity depending on synthetic method, controllable synthesis (e.g., morphology and specific surface area), mechanical flexibility, facile synthesis, and lower synthetic cost compared to other CPs (Figure 3 and 4) [1–3,7–10].

#### 1.1.2.1. Synthetic methods of PANI

Conventional PANI has been synthesized according to the MacDiarmid *et al.*, which includes the chemical oxidation of aniline in an acidic medium [11–15]. In the conventional method, the polymerization of aniline randomly occurs at the interfaces of growing PANI, swollen PANI, and aqueous medium, which making the obtained PANI to be vulnerable to the *ortho*-coupling and Michael reductive reactions. To prepare high-performance PANI without the undesirable reactions, an attempt that polymerizing aniline in a biphasic solvent system composed of aqueous and organic phases (distilled water (H<sub>2</sub>O)/chloroform (CHCl<sub>3</sub>) phase) has been made [16]. Lee *et al.* reported self-stabilized dispersion polymerization (SSDP) that the protonated anilinium ions, oligomers, and grown PANI chains serve as self-stabilizers: when the

temperature of the reaction solution dropped to  $-9\text{ }^{\circ}\text{C}$ , the solubility of the anilinium hydrochloride in the aqueous phase decreased and became distributed in both the aqueous (water) and organic (chloroform) phases. With both a hydrophilic part (amine group) and a hydrophobic part (phenyl ring), anilinium hydrochloride monomers acted as surfactant. After injection of water-soluble initiator, the growing PANI chains moved toward the interface between the aqueous and organic phases as result of insolubility in both aqueous and organic phases (Figure 5) [16]. This leads to *para*-directed polymerization and lower defects and higher conductivity of PANI compared to PANI prepared using conventional polymerization methods. In the case PANI synthesized by SSDP is secondary doped with  $(\pm)$ -10-camphorsulfonic acid (CSA) in *m*-Cresol/chloroform solution, and then, transformed to thin-film, it can exhibit high electrical conductivity as high as  $600\text{ S cm}^{-1}$  [16]. Although PANI synthesized by SSDP method possesses high electrical conductivity and pseudo capacitive characteristics, specific surface area is still low and the morphology is not suitable for swelling and shrinkage of PANI. Additionally, mechanical strength is still weak compared with EDL materials. Thus, to achieve high capacitance and good cycling stability, other factors such as specific surface area, morphology, and mechanical strength must be improved.

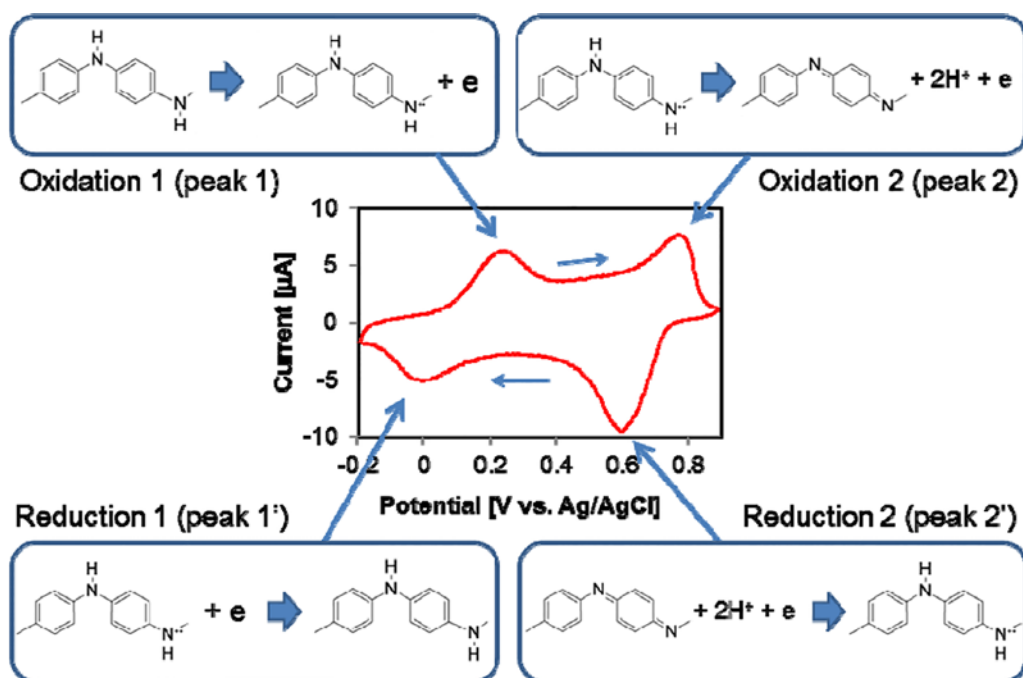


**Figure 3.** A typical cyclic voltammetry (CV) curve of polyaniline (PANI) in hydrochloric acid (HCl, pH 1) showing two sets of redox couples. The direction of potential scan is shown with the arrows. [7].



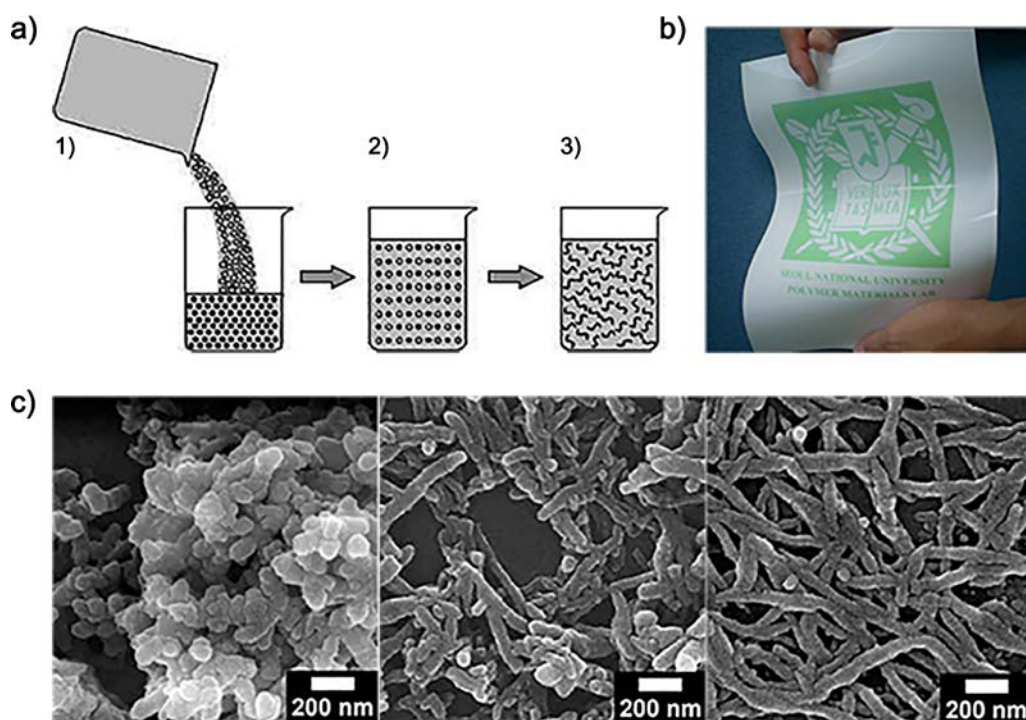


**Figure 4.** a) A schematic illustration of the synthesis of PANI nanofibers. 1) The oxidant (open circles) dopant solution is added into the aniline (solid circles) dopant solution and mixed. 2) A homogenous solution is obtained where all the aniline and oxidant molecules are evenly distributed, thus leading to fast polymerization across the entire solution. 3) PANI nanofibers are formed; b) A photopaper image of the emblem of Seoul National University, printed with an inkjet printer using PANI-poly(4-styrenesulfonate) aqueous solution as ink; c) A scanning electron microscope (SEM) images of PANI nanomaterials synthesized at various initiator/aniline weight ratios. [8–10].

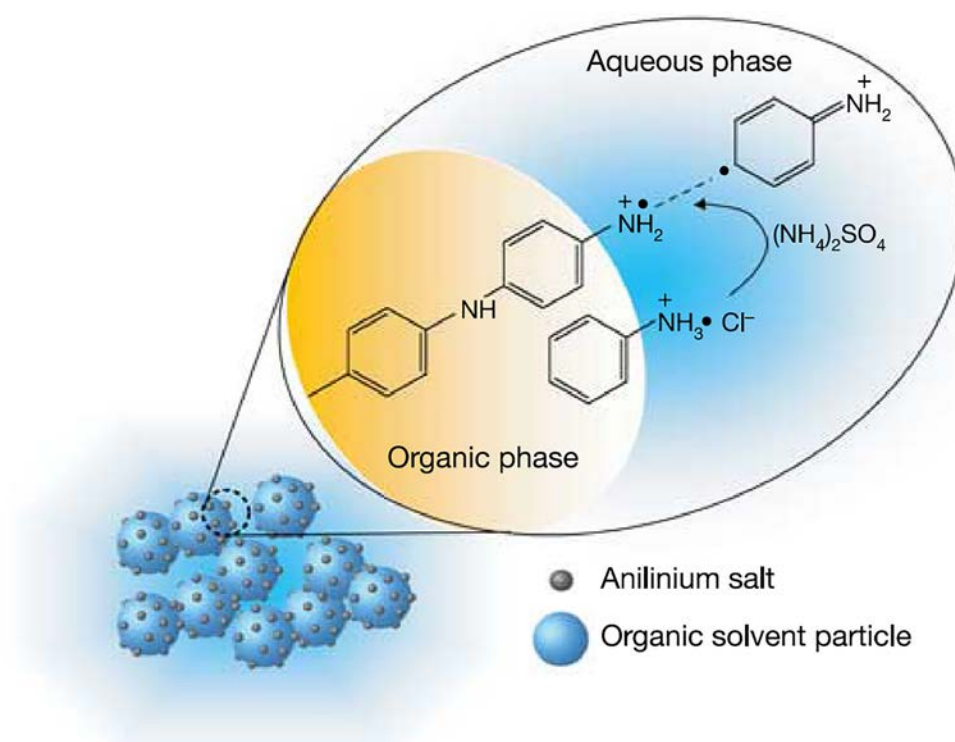


**Figure 5.** Diagram of the self-stabilized dispersion polymerization (SSDP) of PANI. [17].

## **1.2. Objectives and Outlines**

### **1.2.1. Objectives**

The aim of this dissertation is to fabricate supercapacitors with high capacitance and good electrochemical stability by synthesizing diverse PANI/organic inorganic • composite *via* SSDP method with considering five conditions for producing a high-performance supercapacitor. The morphological, spectroscopic, electrical, and electrochemical properties of the PANI/organic • inorganic composite are systematically and deeply studied.

### **1.2.2. Outlines**

This dissertation involves the following subtopics:

- I. PANI/SiO<sub>2</sub> nanocomposite for supercapacitor electrodes
  - 1. Fabrication of PANI/SiO<sub>2</sub> nanocomposite
  - 2. Supercapacitors based on PANI/SiO<sub>2</sub> nanocomposite
- II. PANI/MoS<sub>2</sub> nanocomposite for supercapacitor electrodes
  - 1. Fabrication of PANI/MoS<sub>2</sub> nanocomposite
  - 2. Supercapacitors based on PANI/MoS<sub>2</sub> nanocomposite
- III. PANI/graphene film for flexible supercapacitor electrodes
  - 1. Fabrication of PANI/RGO film
  - 2. Flexible supercapacitor based on PANI/RGO film

A detailed outline of the study is as follows:

1.1 Highly conductive PANI/SiO<sub>2</sub> nanocomposites were synthesized in various diameters (from 18 nm to 130 nm) using SSDP method. The polymerization was carried out in an aqueous/organic liquid system at -30 °C. In this system, biphasic solution plays a key role in directing *para*-direction oriented polymerization of the PANI on the surface of SiO<sub>2</sub> nanoparticles (NPs). Due to its *para*-direction polymerized structure, the synthesized PANI/SiO<sub>2</sub> nanocomposite exhibited enhanced electrical conductivity (ca. 25.6 S cm<sup>-1</sup>) compared with PANI/SiO<sub>2</sub> nanocomposite (ca. 1.4 S cm<sup>-1</sup>) prepared by homogeneous polymerization. The conductivities and Brunauer-Emmett-Teller (BET) surface areas were ca. 25.6 S cm<sup>-1</sup>/170 m<sup>2</sup> g<sup>-1</sup> (18 nm in diameter), ca. 22.5 S cm<sup>-1</sup>/111 m<sup>2</sup> g<sup>-1</sup> (35 nm in diameter), ca. 18.3 S cm<sup>-1</sup>/78 m<sup>2</sup> g<sup>-1</sup> (63 nm in diameter), and ca. 16.4 S cm<sup>-1</sup>/53 m<sup>2</sup> g<sup>-1</sup> (130 nm in diameter). In this series, increased *para*-coupling along the polymer backbone was elucidated using several characterization techniques, including Fourier-transform infrared (FT-IR), X-ray diffraction (XRD), and nuclear magnetic resonance (NMR) spectroscopy. Synthesized PANI/SiO<sub>2</sub> nanocomposite exhibited improved capacitance (ca. 305 F g<sup>-1</sup>) and enhanced cycle-life performance (maintains 72 % of initial gravimetric capacitance after 500 cycles)

compared to PANI/SiO<sub>2</sub> nanocomposite prepared by conventional polymerization method (ca. 112 F g<sup>-1</sup> and 60 % after 500 cycles).

2.1 PANI/MoS<sub>2</sub> nanocomposite was prepared using SSDP method.

Synthesized PANI/MoS<sub>2</sub> nanocomposite demonstrated remarkably high electrical conductivity of ca. 28.6 S cm<sup>-1</sup>. Additionally, PANI/MoS<sub>2</sub> nanocomposite showed high capacitance (ca. 400 F g<sup>-1</sup>) and good cycling stability (84 % after 500 cycles).

3.1 With developments in technology, tremendous effort has been devoted to produce flexible, scalable, and high-performance supercapacitor electrode material. This report presents a novel fabrication method of highly flexible and scalable electrode material for high-performance supercapacitors using solution-processed PANI/RGO hybrid film. Scanning electron microscope (SEM), transmission electron microscope (TEM), Raman, and X-ray photoelectron spectra (XPS) analyses showed that the PANI/RGO film was successfully synthesized. The percentages of the PANI component in the film were controlled (88, 76, and 60 %), and the maximum electrical conductivity (ca. 906 S cm<sup>-1</sup>) was observed at the PANI percentage of 76 %. Notably, electrical conductivity of the PANI/RGO film (ca. 906 S cm<sup>-1</sup>) was larger than both PANI (ca. 580 S cm<sup>-1</sup>) and RGO (ca. 46.5 S cm<sup>-1</sup>) components. XRD analysis demonstrated that the strong  $\pi$ - $\pi$  interaction

between the RGO and the PANI caused more compact packing of the PANI chains by inducing more fully expanded conformation of the PANI chains in the solution, leading to increase in the electrical conductivity and crystallinity of the film. The PANI/RGO film also displayed diverse advantages as a scalable and flexible electrode material (e.g., controllable size and great flexibility). During the electrochemical tests, the film exhibited high capacitance of ca. 431 F g<sup>-1</sup> and enhanced cycling stability (74 % after after 500 cycles) in comparison with pure PANI film synthesized by SSDP method (ca. 256 F g<sup>-1</sup> and 60 % after 500 cycles).

## 2. EXPERIMENTAL DETAILS

### 2.1. PANI/SiO<sub>2</sub> nanocomposite for supercapacitor electrodes

#### 2.1.1. Fabrication of PANI/SiO<sub>2</sub> nanocomposite

*Materials:* Aniline (C<sub>6</sub>H<sub>7</sub>N, ≥99.5%), ammonium persulfate (APS) ([NH<sub>4</sub>]<sub>2</sub>S<sub>2</sub>O<sub>8</sub>, 98%), hydrochloric acid (HCl, 37%), ammonia solution (28–30%), chloroform (CHCl<sub>3</sub>, ≥99.8%), and poly(tetrafluoroethylene) (PTFE; [C<sub>2</sub>F<sub>4</sub>]<sub>n</sub>, 60 wt % dispersion in H<sub>2</sub>O) were purchased from Aldrich Chemical Co. Deionized water was used as a chemical solvent for aniline. SiO<sub>2</sub> NPs (diameter: 12 nm and 22 nm) were purchased from Aldrich Chemical Co. The 50 and 100 nm SiO<sub>2</sub> NPs were synthesized using tetraethyl ortho silicate and ammonia solution.

*Fabrication of PANI/SiO<sub>2</sub> nanocomposite (SPI):* At first, the SiO<sub>2</sub> NPs (3.8 mmol) was added to deionized water (40 mL). An anilinium solution, aniline (2.1 mmol) and HCl (8.2 mmol) were added in deionized water (11 mL), was injected to the above-prepared solution under vigorous stirring condition (with magnetic stirring bar) and reaction proceeded for 1h at 0 °C. Then, the mixed solution was injected to the chloroform solution (80 mL) in Erlenmeyer flask with mechanical stirrer at −30 °C. Subsequently, APS solution (0.854 M, 2 mL) was injected to the mixture as initiator in a dropwise fashion. The reaction was performed until the color of the solution changed from opaque to

dark-green, which represents chemically doped PANI:emeraldine salt (ES). After the polymerization, PANI/SiO<sub>2</sub> nanocomposites were precipitated by centrifugal precipitation and washed with distilled water, ethanol, and acetone to remove residual agents. The size of PANI/SiO<sub>2</sub> nanocomposites were controlled by varying size of SiO<sub>2</sub> cores (from 12 to 100 nm). In each procedure, other reaction conditions are identical to those described above.

*Conventional polymerization for SP2 and bulk PANI:* SiO<sub>2</sub> NPs (3.8 mmol) was added to distilled water (40 mL). An anilinium solution, aniline (2.1 mmol) and HCl (8.2 mmol) were dissolved in deionized water (11 mL), was added as dropwise to the above-prepared solution, and stirred for 1 h under vigorous stirring. An APS solution (0.854 M, 2 mL) was added to the aniline/SiO<sub>2</sub> solution. The polymerization of aniline was carried out at room temperature (25 °C) for 12 h. After the polymerization, a dispersion solution of the PANI/SiO<sub>2</sub> nanocomposite was obtained by centrifugation and re-dispersion in distilled water, ethanol, and acetone. The size of the PANI/SiO<sub>2</sub> nanocomposites were controlled by varying the size of SiO<sub>2</sub> cores (from 12 to 100 nm). In each procedure, other reaction conditions are identical to those described above.

In the case of bulk PANI, aniline (0.01 M) was dissolved in HCl (0.9 M, 35 mL) solution at room temperature (25 °C) by magnetic stirring for 15 min. An



APS solution (0.5 M, 10 mL) was added to the solution which was magnetically stirred for 15 min and then stirring was kept for 6 h. The polymerization was stopped when the color of the solution changed to dark-green, which represents the ES states of chemically doped PANI. The prepared PANI was precipitated by centrifugal precipitation and washed with distilled water, ethanol, and acetone to remove residual agents. Finally the green colored PANI nanofibers were obtained.

*Instrumentation:* Photographs of TEM were obtained with a LIBRA 120 (Carl Zeiss, Germany). In the sample preparation, nanomaterials diluted in ethanol were cast onto a copper (Cu) grid. A JEOL 6700 (JEOL, Japan) was used to obtain Field-Emission SEM (FE-SEM) images and energy dispersive x-ray spectroscopy (EDX) graphs. The XRD was recorded on a New D8 Advance (Bruker, Germany). The FT-IR spectrum was recorded on a MB 100 spectroscope (Bomem, Canada) in the absorption mode. Avance II (Bruker, Germany) was used to obtain solid-state  $^{13}\text{C}$  NMR spectra. The measurement of the electrical conductivity was carried out with a KEITHLY 2400 by a four-probe method (KEITHLY, USA). Nitrogen adsorption/desorption isotherms were measured using Micromeritics ASAP 2000 at 77 K. The electrochemical measurements were performed with a Wonatech WBCS3000 potentiostat, which was measured in a conventional three-electrode beaker type cell in 1 M

sulfuric acid (H<sub>2</sub>SO<sub>4</sub>) solution as electrolyte at 25 °C.

### 2.1.2. Supercapacitors based on PANI/SiO<sub>2</sub> nanocomposites

*Electrochemical measurements:* The electrode for the supercapacitor was prepared as follows. The 2.2 mg of PANI/SiO<sub>2</sub> nanocomposite was mixed with polymeric binder (PTFE, 0.22 mg) and carbon black (0.22 mg). The mixture was coated on a stainless steel mesh (1 x 1 cm<sup>2</sup>) which is known to be stable in acidic condition. The coated mixture was rolled by a bar-coater to form a sheet type. Subsequently, the molded electrode was dried at 25 °C for 12 h before use. Cyclic voltammetry (CV) experiment was performed in the standard three-electrode system; silver (Ag)/silver chloride (AgCl) is used as the reference electrode, and a platinum (Pt) wire (6 cm) is used as the counter electrode in 1 M H<sub>2</sub>SO<sub>4</sub> solution as electrolyte at a sweep rate of 30 mV s<sup>-1</sup>. The galvanostatic charge/discharge tests at the current densities of 2.6 A g<sup>-1</sup> were performed within potential from 0 to 0.8 V in 1 M H<sub>2</sub>SO<sub>4</sub>. The specific capacitances of the electrodes were calculated according to the following equation from CV curves:

$$C_m = \frac{\int i dV}{(\nu \times m \times V)} \quad (1)$$

,where C<sub>m</sub> is the gravimetric capacitance based on the mass of electroactive materials (F g<sup>-1</sup>), i is the response current (mA), V is the potential (V),  $\nu$  is the

potential scan rate ( $\text{V s}^{-1}$ ), and  $m$  is the mass of the active electrode materials (mg).

## **2.2. PANI/MoS<sub>2</sub> nanocomposite for supercapacitor electrodes**

### **2.2.1. Fabrication of PANI/MoS<sub>2</sub> nanocomposite**

*Materials:* Aniline (C<sub>6</sub>H<sub>7</sub>N, ≥99.5%), ammonium persulfate ([NH<sub>4</sub>]<sub>2</sub>S<sub>2</sub>O<sub>8</sub>, 98%), molybdenum disulfide (MoS<sub>2</sub>, powder, < 2 μm, 99 %), and poly(tetrafluoroethylene) (PTFE; [C<sub>2</sub>F<sub>4</sub>]<sub>n</sub>, 60 wt % dispersion in H<sub>2</sub>O) were purchased from Sigma-Aldrich Chemical Co. Hydrochloric acid (HCl, 35.0-37.0 wt. %), chloroform (CHCl<sub>3</sub>, 99.8 %), and N-methyl-2-pyrrolidone (NMP, 99.5 %) were purchased from the Samchun Chemical Co. Mortar and pestle were acquired from Samwha ceramic.

*Preparation of MoS<sub>2</sub> nanosheets:* Exfoliation of MoS<sub>2</sub> was conducted by grinding 0.8 g of MoS<sub>2</sub> powder with 0.4 mL of NMP for 30 min in a mortar. The solvents were removed in a vacuum oven from gel-like mixtures. The powders were dispersed in 20 mL of ethanol/ deionized water (45 vol % of ethanol) and sonicated for 2 hr. Unexfoliated MoS<sub>2</sub> flakes were removed by centrifugation for several times and the supernatant was collected.

*Preparation of PANI/MoS<sub>2</sub> nanocomposite:* In the first step, aniline (0.2g) and HCl (35.0-37.0 wt. %, 1g) were added to deionized water (6 g) and then stirred for 10 min. Next, as-synthesized MoS<sub>2</sub> nanosheet (0.01 g) is added to above solution and then sonicated for 2hr. Next, chloroform (12 mL) was injected to mixture and then stirred for 1 min. Subsequently, the mixture was

sonicated for 1h. After sonication, the mixture was stirred under temperature of -43 °C at 400 rpm. When the temperature of solution dropped to -9 °C, initiator solution (H<sub>2</sub>O: 2 g, ammonium persulfate: 0.24 g, 35.0-37.0 wt. % HCl: 0.1 g), was injected to the mixture. After stirring solution under -43 °C for 12 h, fabricated PANI/MoS<sub>2</sub> nanocomposite was washed, centrifuged, and dried. In the case of pure PANI, it was prepared *via* identical synthetic procedure with PANI/MoS<sub>2</sub> nanocomposite except incorporation of MoS<sub>2</sub> nanosheet.

*Instrumentation:* FE-SEM images of samples were taken using a JSM-6701F (JEOL, Japan). Raman spectra of samples were obtained using a T64000 Raman spectrometer (Horiba Jobin Yvon, Japan) with a 514 nm argon (Ar) laser as the excitation source. The electrical conductivity measurements of samples were conducted with four-in-line probe method using a LORESTA-GP/MCP-T610 (MITSUBISHI, Japan).

### **2.2.2. Supercapacitor based on PANI/MoS<sub>2</sub> nanocomposite**

*Electrochemical measurements:* All electrochemical tests (CV and galvanostatic charge/discharge tests) were conducted in a three-electrode system (the reference and counter electrodes were Ag/AgCl and Pt, respectively) in 1 M H<sub>2</sub> SO<sub>4</sub> solution at a potential window of 0.0-0.8V. The working electrodes were prepared as follows. Firstly, The 1.5 mg of active

material (MoS<sub>2</sub> nanosheet, PANI, or PANI/MoS<sub>2</sub> nanocomposite) was mixed with PTFE (0.18 mg) and carbon black (0.18 mg). Next, the mixture was coated on stainless steel mesh (1 cm × 1 cm). Then, coated electrode was dried in at 25 °C for 24 h. The accurate gravimetric capacitance ( $C_m$ ) and internal resistance ( $R$ ) were calculated from galvanostatic charge/discharge curves using following equations.  $C_m$  (F g<sup>-1</sup>) = (I × t) / (m × V), where I is discharging current (mA), t is discharging time (s), m is mass of active material (mg), and V is potential window during discharging process (V).  $R$  (Ω g) = V / (I/g), where V is IR drop and (I/g) is discharging current density (A g<sup>-1</sup>).

## 2.3. PANI/graphene film for flexible supercapacitor electrodes

### 2.3.1. Fabrication of PANI/RGO film

*Materials:* Graphite powder (325 mesh), sodium nitrate ( $\text{NaNO}_3$ , 99 %), hydrazine monohydrate ( $\text{N}_2\text{H}_4\cdot\text{H}_2\text{O}$ , 98 %), aniline ( $\text{C}_6\text{H}_5\text{NH}_2$ ,  $\geq 99.5$  %), poly(tetrafluoroethylene) (PTFE;  $[\text{C}_2\text{F}_4]_n$ , 60 wt % dispersion in  $\text{H}_2\text{O}$ ), ( $\pm$ )-10-camphorsulfonic acid (CSA;  $\text{C}_{10}\text{H}_{16}\text{O}_4\text{S}$ , 98 %), and ammonium persulfate ( $[\text{NH}_4]_2\text{S}_2\text{O}_8$ , 98 %) were purchased from the Sigma-Aldrich Co. Sulfuric acid ( $\text{H}_2\text{SO}_4$ , 95 %), hydrogen peroxide ( $\text{H}_2\text{O}_2$ , 30~35.5 %), hydrochloric acid ( $\text{HCl}$ , 35~37 %), ammonia solution ( $\text{NH}_4\text{OH}$ , 28~30 %), and chloroform ( $\text{CHCl}_3$ , 99%) were purchased from the Samchun Chemical Co. Potassium permanganate ( $\text{KMnO}_4$ , 99.3 %) and phosphorus pentoxide ( $\text{P}_2\text{O}_5$ , extra pure) were purchased from the Junsei Chemical Co. *m*-Cresol ( $\text{C}_7\text{H}_8\text{O}$ ,  $\geq 98$  %) was purchased from the Tokyo Chemical Industry Co. Stainless steel mesh (SUS 304) was purchased from the Nilaco Corp. Potassium persulfate ( $\text{K}_2\text{S}_2\text{O}_8$ , 99 %) was purchased from the Kanto Chemical Co.

*Preparation of RGO:* Initially, graphene oxide solution was prepared by slightly modified Hummer's method. Before actual oxidation, graphite powder (5 g),  $\text{P}_2\text{O}_5$  (2.5 g) and  $\text{K}_2\text{S}_2\text{O}_8$  (2.5 g) were dissolved in  $\text{H}_2\text{SO}_4$  solution (30 ml) in a flask and the whole solution was heated at 80 °C for 6hr. The solution was filtered through mixed cellulose acetate filter (ADVANTEC) with excess

deionized water and remaining powder was kept in vacuum oven for 24 h. The  $\text{NaNO}_3$  (2.5g) was dissolved in  $\text{H}_2\text{SO}_4$  solution (115 ml) with vigorous stirring. The dried graphite powder was poured into well mixed  $\text{NaNO}_3/\text{H}_2\text{SO}_4$  solution with vigorous stirring, while kept in ice bath. In this state,  $\text{KMnO}_4$  (15g) was slowly poured into the solution in 10 min, keeping the temperature lower than  $20^\circ\text{C}$ . After 30 min, ice bath was removed and whole solution was heated at  $45^\circ\text{C}$  for 12hr, turning the color of solution to brownish gray paste. Then deionized water (230 ml) was poured into the paste, keeping the temperature below  $40^\circ\text{C}$ . Then deionized water (700 ml) was poured again and  $\text{H}_2\text{O}_2$  (25 ml) was slowly added to the solution, forming bright yellow particles in solution. This graphite oxide (GO) solution was washed with 10 wt %  $\text{HCl}$  solution three times and deionized water for several times until the pH of solution turns into 7. This solution was ultrasonicated for 1hr to exfoliate graphitic oxide into graphene oxide. Then the solution was centrifugated at 4000 rpm for 30 min to exclude residue. The graphene oxide solution was dried in vacuum oven and graphene oxide powder was obtained. The graphene oxide powder was dissolved in deionized water (3 mg/ml) and hydrazine monohydrate was added to the solution (the volume ratio of hydrazine monohydrate : water = 1 : 1000). And this solution was heated at  $80^\circ\text{C}$  for 12hr. After reduction process, the RGO solution was filtered by filter paper with



excess deionized water and was dried in vacuum oven, as in powder form, for further use.

*Preparation of PANI/RGO film:* As-prepared RGO powder was added to HCl solution (2.5 M, 40 ml) in Erlenmeyer flask. The solution was sonicated for 24 hr and aniline monomer was added, keeping vigorous stirring. After that, chloroform (60 ml) was added to the mixture, leading to the phase separation (chloroform phase at the bottom, aqueous phase on the top). Then the initiator, APS (the weight ratio of APS : aniline = 1.2:1) in HCl solution (3.75 M, 16 ml), was added to the above bi-phase solution and stirred for 24 hr at - 40 °C, resulting in the low-temperature interfacial polymerization. After polymerization process, the solution was centrifuged and dried. The feeding weight ratio of aniline to RGO was changed as 16:1, 12:1, and 8:1, and the obtained composites were named as PANI/RGO (PARG) 1, PARG 2, and PARG 3, respectively. The PARG powder was dispersed in ammonia solution (1.2 M, 215 ml) and vigorously stirred for 24 hr to de-dope the PANI chains on the RGO, resulting in de-doped PARG (De-PARG). This solution was centrifuged again and dried to collect powder. The real weight percentages of the PANI component in the De-PARG 1, 2 and 3 composites were calculated as 88 % for De-PARG 1, 76 % for De-PARG 2, and 60 % for De-PARG 3, respectively. The De-PARG powder was mixed with the CSA (the mole ratio of

PANI : CSA = 2:1) to re-dope the PANI chains on RGO, resulting in re-doped PARG (Re-PARG). The Re-PARG powder was added to the *m*-Cresol/chloroform solution (the volume ratio of *m*-cresol : chloroform = 7:3) to be as 2.38 wt % of total mass of solution and stirred for 3 hr and sonicated for 24 hr. The Re-PARG solution was drop-casted onto glass substrate and was annealed at 40 °C for 16 hr. Finally, the free standing film was obtained by detaching the annealed film from the glass substrate in the water. The Re-PARG films which were prepared by the De-PARG 1, 2 and 3 were named as the Re-PARG film 1, 2 and 3, respectively. The synthetic procedures of the PANI, De-PANI, and Re-PANI film were identical to those of the PARG, De-PARG, and Re-PARG film except incorporation of the RGO.

*Instrumentation:* SEM and TEM images were obtained with a JSM-6701F (JEOL, Japan) and LIBRA 120 (Carl Zeiss, Germany), respectively. Raman spectra were recorded using a Horiba-Jobin Yvon LabRam Aramis spectrometer with a 514 nm Ar-ion laser as the excitation source. The XPS were collected on Sigma probe (ThermoVG, U.K). Thermo-gravimetric analysis (TGA) was performed on a Perkin Elmer Pyris 6 TGA analyzer (USA) with a heating rate of 10 °C min<sup>-1</sup> under air flow of 20 ml min<sup>-1</sup>. The direct-current electrical conductivity measurements of samples were carried out with the four-probe method

using a KEITHLY 2400 (KEITHLY, USA). The XRD patterns were taken with a D8 Advance (Bruker, Germany) equipped with nickel (Ni)-filtered Cu K $\alpha$  radiation source ( $\lambda$ = 0.15406 nm).

### **2.3.2. Flexible supercapacitor based on PANI/RGO film**

*Electrochemical measurements:* The CV and galvanostatic charge/discharge tests were performed on a Wonatech WBCS 3000 potentiostat/galvanostat instrument to assess the electrochemical performances of the samples. All of the electrochemical measurements were performed in a three-electrode system in H<sub>2</sub>SO<sub>4</sub> solution (1 M) as the electrolyte at 25 °C, where the counter and reference electrodes were Pt and Ag/AgCl, respectively. The potential ranges for CV and galvanostatic charge/discharge tests were 0.0 to 0.8 V. The Re-PARG film and Re-PANI film were directly employed as the working electrodes. The pristine RGO was prepared for the working electrode as follows. The mixtures of the RGO (95 %) and PTFE (5 %) were coated onto the stainless steel mesh (1 x 1 cm<sup>2</sup>) and then dried in air at 25 °C for 24 h. The electrochemical behavior was first characterized by the CV test at a scan rate of 5 mV s<sup>-1</sup>. After that, the galvanostatic charge/discharge test was carried out at a current density of 0.45 A g<sup>-1</sup> to precisely evaluate the gravimetric capacitance, C<sub>m</sub> (F g<sup>-1</sup>), and internal resistance, R ( $\Omega$  g). The

mass of the Re-PARG film, Re-PANI film, and RGO for the CV and galvanostatic charge/discharge tests were 2 mg. The gravimetric capacitances ( $C_m$ ) were calculated by using the equation  $C_m = (i \times \Delta t) / (m \times \Delta V)$ , where  $C_m$  is the gravimetric capacitance in  $F g^{-1}$ ,  $i$  is the constant discharge current in mA,  $\Delta t$  is the discharge time in sec,  $m$  is the total mass of the active material in mg,  $\Delta V$  is the potential window in V. The internal resistances ( $R$ ) were estimated according to the  $R = \Delta V / (i/g)$ , where,  $R$  is the internal resistance in  $\Omega g$ ,  $\Delta V$  is the “IR drop (vertical voltage drop at the beginning of the discharge curve)” in V and  $(i/g)$  is the discharge current density in  $A g^{-1}$ . In order to study the electrochemical performance of the Re-PARG film depending on the size, the CV test was performed to the 2 and 60 mg of the Re-PARG film with the two different sizes (1.2 and 36  $cm^2$ ) in  $H_2SO_4$  (1M) solution at the scan rate of 5  $mV s^{-1}$ . The area capacitances,  $C_{area}$  ( $F cm^{-2}$ ), were calculated according to the following equation from the CV curves  $C_{area} = (\int i dV) / (v \times \Delta V)$ , where,  $C_{area}$  is the area capacitance in  $F cm^{-2}$ ,  $i$  is the response current density during the discharging in  $A cm^{-2}$ ,  $v$  is the scan rate in  $V s^{-1}$ , and  $\Delta V$  is the potential window in V. The cycle stability of the Re-PARG film (2 mg) and Re-PANI film (2 mg) were measured by the galvanostatic charge/discharge test at a current density of 0.45  $A g^{-1}$ .

in  $\text{H}_2\text{SO}_4$  solution (1M). For investigating the supercapacitor performance of the Re-PARG film under bending condition, the CV test was performed to the 6 mg of the Re-PARG films with two different bending angles of  $0^\circ$  and  $180^\circ$  at a scan rate of  $5 \text{ mV s}^{-1}$ .

### **3.1. PANI/SiO<sub>2</sub> nanocomposite for supercapacitor electrodes**

#### **3.1.1. Fabrication of PANI/SiO<sub>2</sub> nanocomposite**

PANI/SiO<sub>2</sub> nanocomposite (SP1) were synthesized by SSDP, as illustrated in Figure 6. First, SiO<sub>2</sub> NPs were dispersed in aqueous solution to serve as templates for adsorption of aniline monomers. Then, anilinium hydrochloride monomer ions were added to the SiO<sub>2</sub> NP solution. The monomer ions preferentially located on the surface of the SiO<sub>2</sub> NPs due to charge–charge interactions between the positively charged amine of the monomer and the negatively charged silica surface. After stirring for 1 h, chloroform was added to the monomer-impregnated SiO<sub>2</sub> NP solution to lower the melting temperature of the solution. When the temperature of the reaction solution dropped to –9 °C, the solubility of the anilinium hydrochloride in the aqueous phase decreased and became distributed in both the aqueous (water) and organic (chloroform) phases. [16]. Thus, through the  $\pi$ – $\pi$  stacking, additional anilinium hydrochloride monomer was adsorbed onto the surface of SiO<sub>2</sub> where monomer ions were pre-located [18,19]. After injection of APS as a water-soluble initiator, polymerization of monomer was initiated near the surface of the SiO<sub>2</sub> NPs. The growing PANI chains moved toward the interface between the aqueous and organic phases as result of insolubility in both aqueous and organic phases [20,21,22]. With both a hydrophilic part (amine

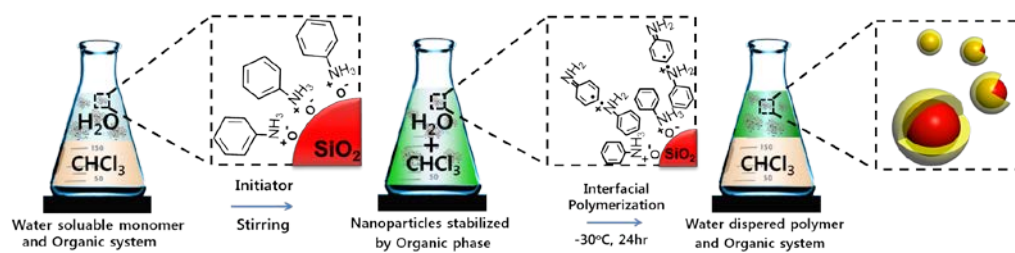
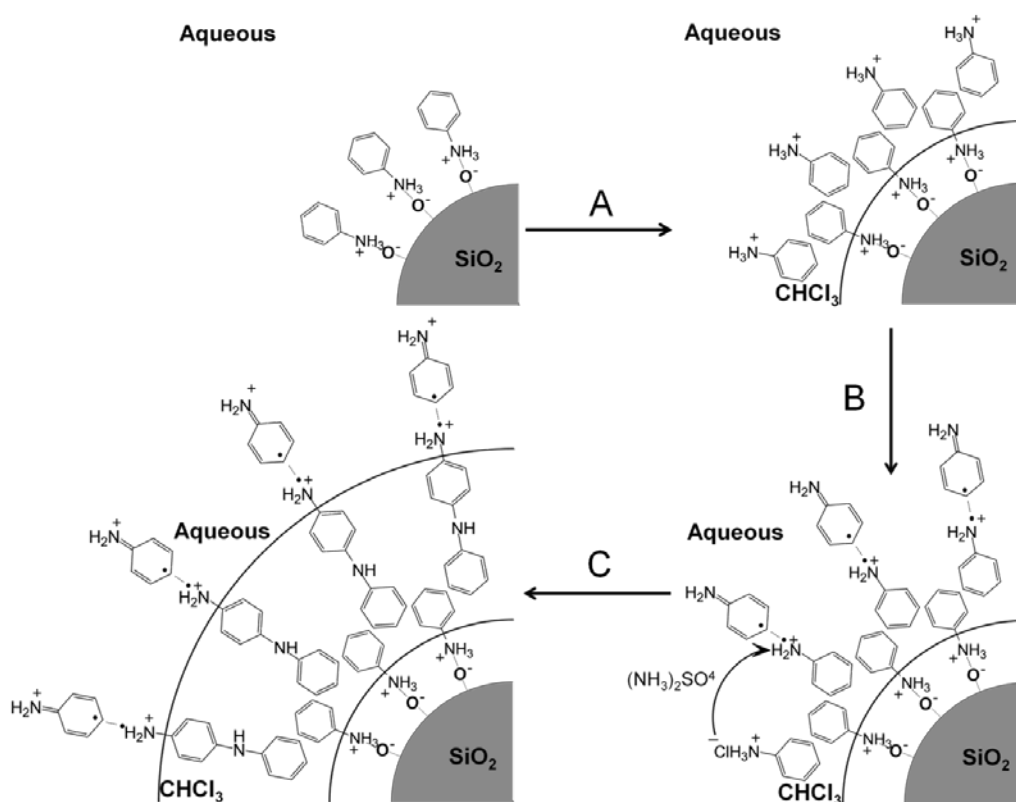


**Figure 6.** Illustrations of the sequential steps for synthesis of PANI/SiO<sub>2</sub> nanocomposite.

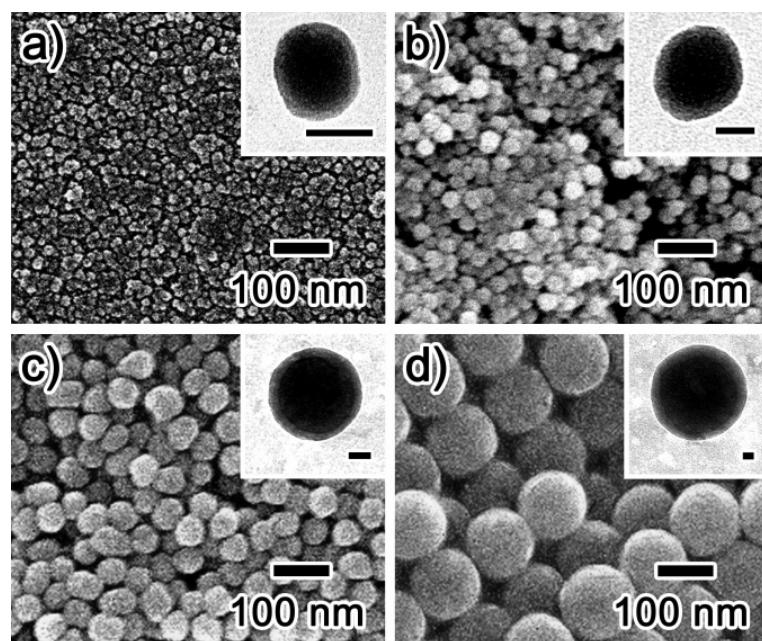
group) and a hydrophobic part (phenyl ring), anilinium hydrochloride monomers acted as surfactant [16,17,23]. Because the monomers and growing polymer chains acted as interfacial stabilizers, the organic phase could be well dispersed in the aqueous reaction medium. Additionally, the organic phase tended to separate the aniline monomers and grown PANI chains from the reactive ends of the chains in the aqueous phase. As a result, undesirable side reactions, such as ortho-coupling or Michael reductive additions, were suppressed, and the polymerization proceeded mainly in the para-direction (Figure 7) [16,21,22]. After 24 h of polymerization at  $-30\text{ }^{\circ}\text{C}$ , green SP1 was obtained.

Figure 8 shows FE-SEM and TEM images of SP1 particles of various diameters (*ca.* 18, 35, 63, and 130 nm). The size of the SP1 could be controlled by varying the size of  $\text{SiO}_2$  NPs. The histograms of the particle size distributions are shown in Figure 9. The core/shell structure of SP1 was confirmed by TEM observation. The insets in Figure 8 clearly show that the  $\text{SiO}_2$  NPs were encapsulated by a thin polymer shell. These results indicate that  $\text{SiO}_2$  NPs of various sizes were successfully coated with polymer shell *via* SSDP. Based on the microscopic images, it could be considered that the SP1 has the similar shape as the previously reported PANI/ $\text{SiO}_2$  nanocomposite synthesized by conventional polymerization method [20]. The compositions of





**Figure 7.** Illustrations of the sequential steps for synthesis of PANI/SiO<sub>2</sub> nanocomposite.



**Figure 8.** FE-SEM images and TEM images (inset) of SP1 with the average size of a) 18 nm, b) 35 nm, c) 63 nm, and d) 130 nm. The scale bars of inset images represent 15 nm.

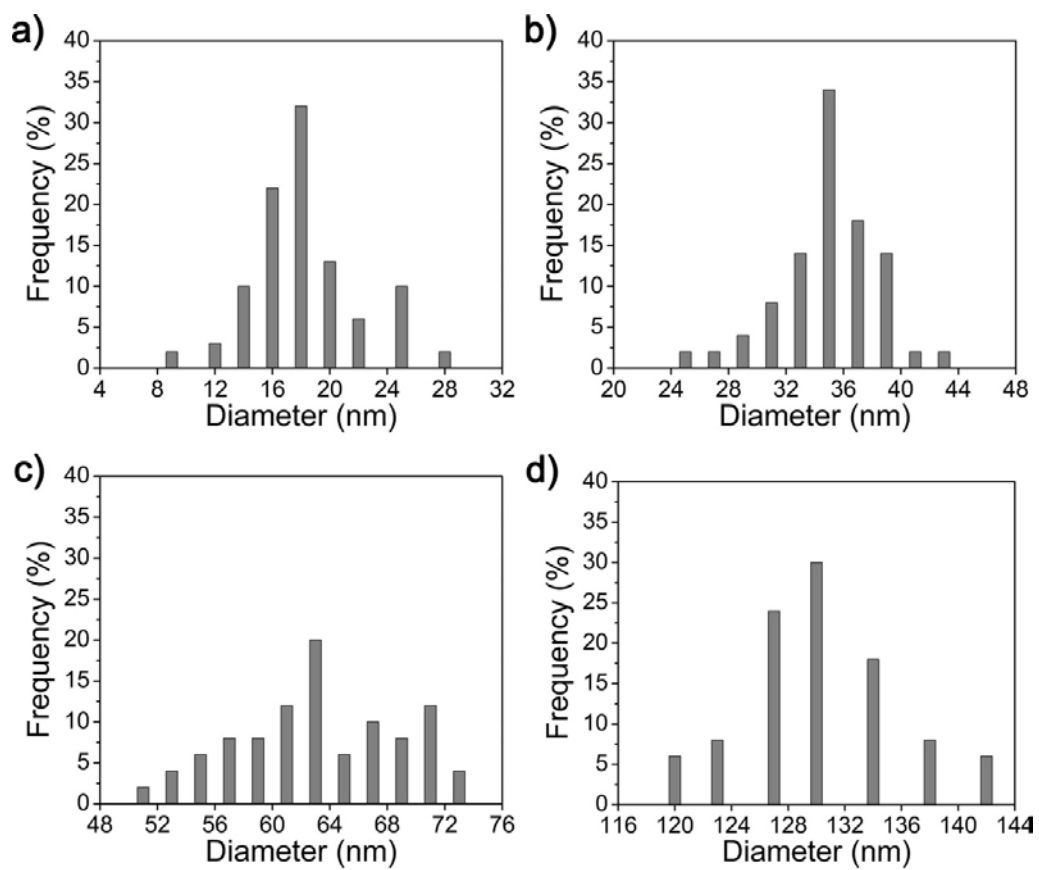


**Figure 9.** Size distribution histograms of SP1 with different diameters.

**Table 1.** Weight ratio of the pristine SiO<sub>2</sub> NPs and PANI/SiO<sub>2</sub> nanocomposite measured by EDX

Element percentage (wt%)	Pristine SiO <sub>2</sub> NPs	PANI/SiO <sub>2</sub> nanocomposite
C	7.99	37.47
O	64.69	35.98
Si	27.33	16.55
N	0.00	7.31
Cl	0.00	2.69
Totals	100	100

pristine SiO<sub>2</sub> NPs and SP1 were also investigated by EDX (Table 1). Compared to the pristine SiO<sub>2</sub> NPs, the %C values of the SP1 increased, whereas the %O and %Si values decreased due to adsorption of PANI on the silica surface. Notably, the detection of nitrogen, attributable to amine groups in PANI, confirms the existence of PANI on the surface of the SiO<sub>2</sub> NPs. In addition, the observation of chloride atoms in the SP1 indicates the hydrochloric acid doping state of the PANI. The detection of carbon in the pristine SiO<sub>2</sub> sample could be attributed to the carbon tape used for fixing the samples onto the EDX specimen mount. From these data, it was concluded that SP1 was successfully synthesized *via* the SSDP method, and the diameter of the SP1 could be controlled by varying the size of SiO<sub>2</sub> NP.

FT-IR spectroscopy of SP1 was also used to confirm the SSDP polymerization of PANI (Figure 10a). PANI/SiO<sub>2</sub> nanocomposite prepared by conventional polymerization method (SP2) were used for comparison. In the spectra of both SP1 and SP2, characteristic PANI peaks were observed at 1582, 1484, and 1310 cm<sup>-1</sup>, originating from quinone ring deformation, phenyl ring deformation, and C–N stretching of a secondary aromatic amine, respectively [21,22]. The existence of these peaks demonstrated the successful polymerization of PANI on the surface of the SiO<sub>2</sub> NPs.

XRD and NMR analyses were performed to investigate the *para*-direction

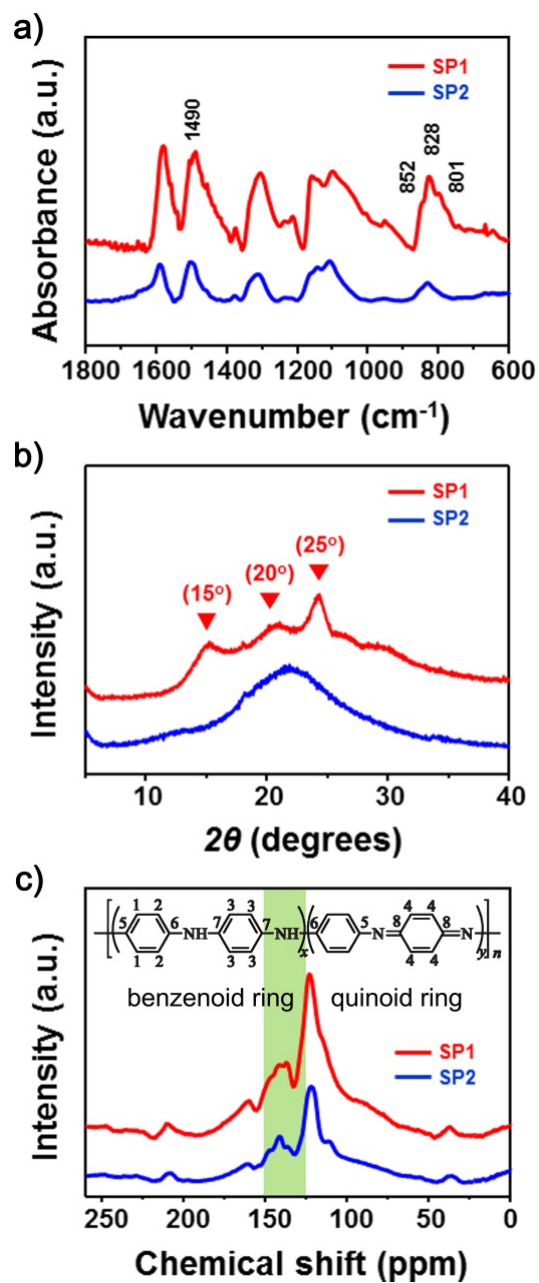


**Figure 10.** a) FT-IR spectra, b) XRD patterns, and c) Solid-state  $^{13}\text{C}$  NMR spectra of the EB-state SP1 (red line) and SP2 (blue line).

polymerization. XRD patterns of SP1 and SP2 in the emeraldine base (EB) state are shown in Figure 10b. EB-state PANI was obtained by deprotonation of the ES-state PANI using 0.8 M ammonia solution. The SP2, which was prepared *via* conventional polymerization method, exhibited a broad scattering background in its spectra, indicating that the amorphous region dominated the PANI of SP2 [17,23]. On the other hand, background peaks in the spectra of SP1 obviously decreased, and intense peaks at 15, 20, and 25° appeared. The *d*-spacing ( $\sim 3.5$  Å) associated with the diffraction peak at 25° corresponds to the face-to-face inter-chain stacking distance between phenyl rings [17,23]. Thus, the increased peak intensity at 25°, along with the decrease in background intensity, implies improved  $\pi$ - $\pi$  inter-chain stacking. These results suggest a more planar chain conformation with reduced torsion angles between the phenyl rings and the plane of the backbone, resulting in elongation of the effective conjugation length. Additionally, the increase crystallinity of SP1 also induces the improvement of conductivity. It is well known that CPs with higher conductivities are obtained in more homogeneous systems with a high degree of crystallinity [24–34]. In the conductivity model of CPs, electrons are transported along electronically isolated ordered regions through disordered regions where the electrons readily become localized. Consequently, the delocalization length of the electrons relies on the length of the ordered region

between the disordered regions. Based on previous studies [24–34] and XRD analysis, it is believed that the highly conductive and crystalline PANI was successfully fabricated on the SiO<sub>2</sub> NP.

Figure 10c shows the <sup>13</sup>C cross-polarization and magic-angle spinning NMR (<sup>13</sup>C CP–MAS NMR) spectra of the SP1 in the EB-state. The combined <sup>13</sup>C CP–MAS NMR technique is very powerful for resolving different microstructures present in the PANI shell. Four characteristic peaks were observed at 123, 137, 141, 148 (shoulder), and 158 ppm relative to tetramethylsilane. The clear peaks could be attributed to the ideal structure of PANI, as shown in the inset of Figure 10c: a peak at 158 (non-protonated carbon 8), a shoulder at 148 ppm (non-protonated carbon 5), peaks around 140 ppm (carbons 6, 7 and quinoid carbon 4), peak at 123 ppm (benzenoid carbons 1, 2), and a shoulder at 113 ppm (benzenoid carbon 3) [16]. It is important to note that the SP1 presented two distinct peaks around 137 ppm in its spectra, while the SP2 exhibited only one peak in this region. These two peaks in SP1 correspond to the idealized repeat structure of the EB-state PANI. The protonated carbons (C4) in the quinoid ring, without rotation around the bent linkage of the imine group (=N–), contributed two structures that appeared as two peaks around 137 ppm. [35,36]. In other words, the SP1 has an idealized EB repeat structure in its polymeric backbone, mainly oriented in the *para*-



direction. These results indicate that the PANI shell synthesized according to the SSDP method in this study had much greater *para*-direction-oriented aniline in its polymeric backbone compared to the PANI shell prepared by conventional polymerization method.

Nitrogen sorption experiments were performed to characterize the textural properties of different sized SP1. The nitrogen adsorption–desorption isotherms are displayed in Figure 11. The BET surface areas were *ca.* 170, 111, 78, and 53 m<sup>2</sup> g<sup>-1</sup> for diameters of 18, 35, 63, and 130 nm, respectively; thus, surface area was inversely proportional to the size of the SiO<sub>2</sub> NPs.

To investigate the electrical conductivity of the PANI, the material was pressed and prepared into disk-shape samples. The conductivity of bulk PANI (Figure 12) prepared *via* conventional polymerization was measured similarly for comparison. The electrical conductivities of the samples were measured by the four-probe method (Table 2). The electrical conductivity of the bulk PANI was found to be about 0.5 S cm<sup>-1</sup>. The conductivities of SP1 with diameters of 18, 35, 63, and 130 nm were measured to be *ca.* 25.6, 22.5, 18.3, and 16.4 S cm<sup>-1</sup>, respectively. On the other hand, the electrical conductivities of the SP2 were found to be *ca.* 1.42, 0.74, 0.58, and 0.32 S cm<sup>-1</sup> for samples with diameters of 18, 35, 63, and 130 nm, respectively. An improvement in the electrical conductivity of the SP1 samples (one order of magnitude higher than

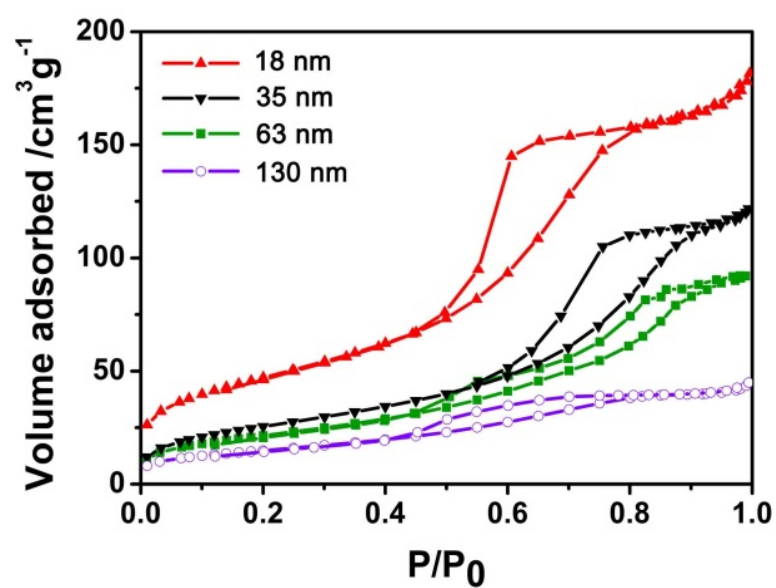


**Figure 11.** Nitrogen adsorption/desorption isotherms of different sized SP1: 18 nm (red line), 35 nm (green line), 63 nm (black line), and 130 nm (purple line).

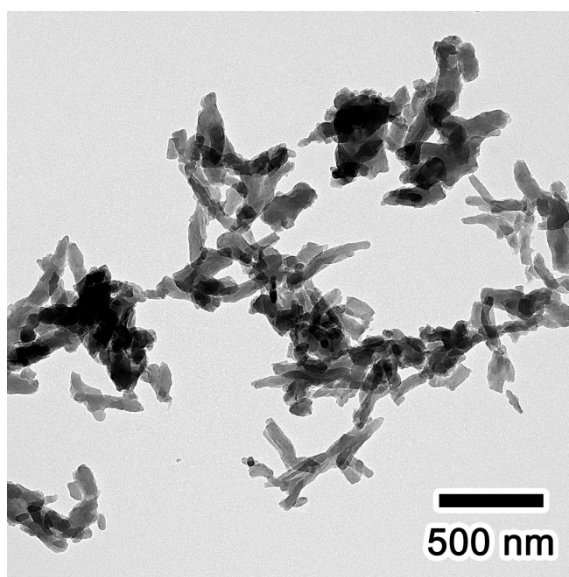


**Figure 12.** TEM image of the bulk PANI prepared by conventional polymerization method. Its diameter is *ca.* 1  $\mu\text{m}$ .

**Table 2.** Electrical conductivities of the PANI/SiO<sub>2</sub> nanocomposites.

Samples	Conductivity (S cm <sup>-1</sup> )			
	18 nm	35 nm	63 nm	130 nm
SP1 <sup>a</sup>	25.6	22.5	18.3	16.4
SP2 <sup>b</sup>	1.42	0.74	0.58	0.32

<sup>a</sup>The SSDP was applied for the fabrication of SP1 samples.

<sup>b</sup>The SP2 samples were synthesized by conventional polymerization.

for the SP2 and bulk PANI) was achieved by increasing the purity of the materials and by aligning the polymer chains. The electrical conductivity of CPs is strongly affected by the molecular structure and the polymer chain alignment [17,23]. Intramolecular electron transport is restricted by structural defects or impurities in conjugated structures, because CPs are principally one-dimensional systems with a typical conjugated backbone structure [17,23]. Therefore, the enhanced electrical conductivity of the SP1 originated from reduced structural defects in the polymer backbone and the *para*-direction-oriented polymerization. In addition, the electrical conductivities increased as the size of nanocomposite decreased in both SP1 and SP2 (from *ca.* 0.32 to *ca.* 1.42 S cm<sup>-1</sup> in SP1 and from *ca.* 16.4 to *ca.* 25.6 S cm<sup>-1</sup> in SP2). The smaller particles exhibited higher compactness and order when they were pressed into disks, thus leading to higher conductivity [37].

### **3.1.2. Supercapacitors based on PANI/SiO<sub>2</sub> nanocomposite**

The synthesized PANI/SiO<sub>2</sub> nanocomposite were prepared as electrodes for CV test, and galvanostatic charge/discharge was employed to evaluate the electrochemical properties and the capacitance performances. The specific capacitances of the electrodes were calculated from CV curves.

Figure 13a shows the CV curves of SP1 (18, 35, 63, 130 nm) and SP2 (18 nm) at a scan rate of 30 mV s<sup>-1</sup> in 1 M H<sub>2</sub>SO<sub>4</sub> solution. In the case of the SP1,

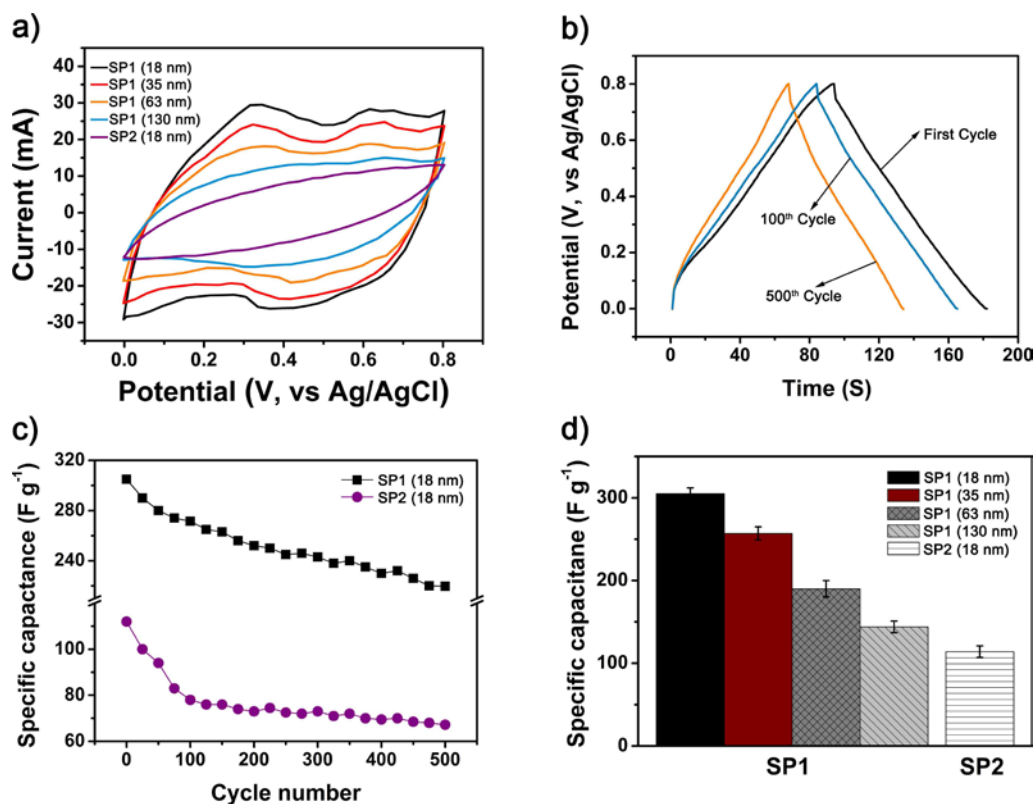


**Figure 13.** Cyclic voltammograms of SP1 (18, 35, 63, 130 nm) and SP2 (18 nm) at  $30 \text{ mV s}^{-1}$  between 0 and 0.8 V in 1M  $\text{H}_2\text{SO}_4$  solution; b) Galvanostatic charge/discharge curve of SP1 (18 nm) at current density of  $2.6 \text{ A g}^{-1}$  in 1M  $\text{H}_2\text{SO}_4$  solution; c) Specific capacitances of SP1 (18 nm) and SP2 (18 nm) as a function of cycle number at a current density of  $2.6 \text{ A g}^{-1}$  in 1 M  $\text{H}_2\text{SO}_4$  solution; d) Specific capacitances of SP1 (18, 35, 63, 130 nm) and SP2 (18 nm) at  $30 \text{ mV s}^{-1}$  between 0 and 0.8 V in 1M  $\text{H}_2\text{SO}_4$  solution.

there are two pairs of redox peaks, indicating the pseudo-capacitive characteristic of PANI. The first redox peak originated from the redox transition of PANI from a semiconducting state (leucoemeraldine state) to a conducting ES-state. Faradaic transformation from emeraldine to pernigraniline is ascribed to the second redox peak [38]. However, the SP2 (18 nm) exhibited a CV curve without obvious redox peaks, because the SP2 (18 nm) had relatively low conductivity, which reduced the conducting network available for facile redox reaction of PANI [39]. The CV curves for SP1 samples exhibited large rectangular areas and high current response, suggesting that SP1 supercapacitors could be made to have large capacitance [40]. Specific capacitance values of SP1 samples, calculated using equation 1, were found to be *ca.* 305, 257, 190, and 144 F g<sup>-1</sup> for materials with diameters of 18, 35, 63, and 130 nm respectively. The smaller (more conductive) SP1 exhibited higher specific capacitance. The high capacitance and capacitance tendency of SP1 samples were attributed to the following two factors: first, the smaller size of SP1 provided larger electrode/electrolyte interface areas, which could provide electrochemical accessibility to the electrolyte through the interface of PANI.<sup>46</sup> Thus, SP1 with large surface area could present the high capacitance performance by effective access of electrolyte to electrode in the redox mechanism [41]. second, the more highly conductive PANI offered a higher

conductivity path, facilitated a rapid charge/discharge process, and improved the redox activity [42]. The highly conductive path in SP1 originated from the enhanced conducting network that facilitated electron transfer in the electrode during the charge/discharge process [42]. The PANI network in SP1 is helpful for increasing electron transfer and the transport rate of electrolyte ions in the diffusion layer, both of which enhance the capacitance of the SP1 electrode [39]. Compared to SP1, the CV curve for SP2 (18 nm) exhibited small rectangular areas and a specific capacitance of  $112 \text{ F g}^{-1}$ . The SP1 (18 nm,  $305 \text{ F g}^{-1}$ ) exhibited enhanced specific capacitance compared with SP2 (18 nm,  $112 \text{ F g}^{-1}$ ). The SP1 (18 nm) presents high specific capacitance ( $305 \text{ F g}^{-1}$ ) compared to not only SP2 (18 nm,  $112 \text{ F g}^{-1}$ ) but also previously reported nanostructured-PANI [40, 42–47]. The specific capacitance of each nanocomposite studied by CV is summarized in Figure 13d.

The electrochemical stability of the SP1 (18 nm) was also investigated using cycled galvanostatic charge/discharge methods (Figure 13b). On the basis of the charge/discharge time, the charge storage capacity loss of SP1 was calculated as 12% loss after 100 cycles and 28% loss after 500 cycles. As shown in Figure 13c, the charge storage capacity of the SP2 (18 nm) decreased more rapidly (30% loss after 100 cycles and 40% loss after 500 cycles) compared with that of the SP1 (18 nm). At the cycle-life test, the dope or



dedope of  $H^+$  into or from the PANI chains on the  $SiO_2$  NP results in the mechanical degradation like a swelling, breaking, and shrinkage of the nanostructured PANI, thus, leading to fading of capacitance [48–51]. In comparison to the SP2 electrode, the better cycle life of SP1 maybe mainly caused by increase crystalline region at backbone of PANI, which provide higher density to PANI and improved resistance toward change of the nanostructure of PANI at the cycle-life test [52].

In conclusion, highly conductive and crystalline PANI was successfully coated onto various sized- $SiO_2$  NPs using the SSDP. The diameter of the nanocomposite was controlled from 18 nm to 130 nm by varying the size of the  $SiO_2$  NP. As the diameter of the PANI/ $SiO_2$  nanocomposite decreased (from 130 to 18 nm), the electrical conductivity increased (from 16.4 to 25.6  $S\ cm^{-1}$ ). When applied as potential electrode materials for supercapacitors, synthesized PANI/ $SiO_2$  nanocomposite exhibited capacity as high as 305  $F\ g^{-1}$  and had enhanced cycle-life performance compared to nanocomposite prepared by conventional polymerization method. The high conductivity and large surface area facilitated the charge/discharge of PANI, and the increased crystalline structure of PANI prevented severe deterioration of the polymer structure. The highly conductive and crystalline PANI/ $SiO_2$  nanocomposites prepared by SSDP can be used in various applications, such as batteries, sensors, actuators,

corrosion protection, electro-chromic devices, and dye-sensitized solar cells.

## **3.2. PANI/MoS<sub>2</sub> nanocomposite for supercapacitor electrodes**

### **3.2.1. Fabrication of PANI/MoS<sub>2</sub> nanocomposite**

The PANI/MoS<sub>2</sub> nanocomposite was synthesized as follows. First, prepared MoS<sub>2</sub> nanosheet was added to aniline hydrochloride solution and then sonicated for 2h. Next, chloroform was injected to mixture, and then, stirred and sonicated for 1 min and 1h, respectively. After sonication process, the mixture was stirred under temperature of  $-43^{\circ}\text{C}$ . When the temperature of solution decreased to  $-9^{\circ}\text{C}$ , initiator solution was injected to the mixture. After stirring solution for 12 h under  $-43^{\circ}\text{C}$ , as-synthesized PANI/MoS<sub>2</sub> nanocomposite was washed, centrifuged, and dried. Figure 14 depicts FE-SEM images of the MoS<sub>2</sub> nanosheets and obtained PANI/MoS<sub>2</sub> nanocomposite. Figure 14a illustrates that MoS<sub>2</sub> nanosheets possesses smooth surface. In contrast, PANI/MoS<sub>2</sub> nanocomposite shows that honeycomb-like structured PANI is polymerized on the MoS<sub>2</sub> nanosheets (Figure 14b), which is characteristic morphology of the PANI synthesized by SSDP to be distinguished from the PANI which has been polymerized by other polymerization processes [16]. This result reflects that PANI has been successfully polymerized on the MoS<sub>2</sub> nanosheet *via* SSDP. Figure 15 displays the Raman spectra of pristine MoS<sub>2</sub> nanosheets, pure PANI, and PANI/MoS<sub>2</sub> nanocomposite. The MoS<sub>2</sub> nanosheets demonstrates its characteristic peaks

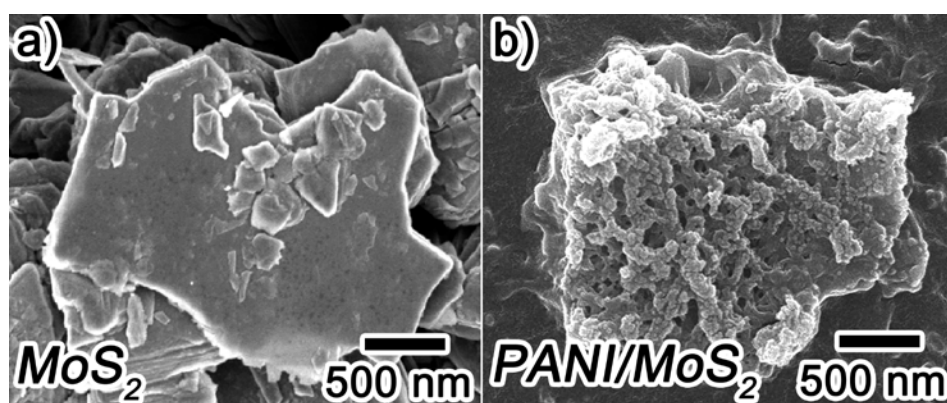


**Figure 14.** SEM images of a)  $\text{MoS}_2$  nanosheets and b)  $\text{PANI}/\text{MoS}_2$  nanocomposite.

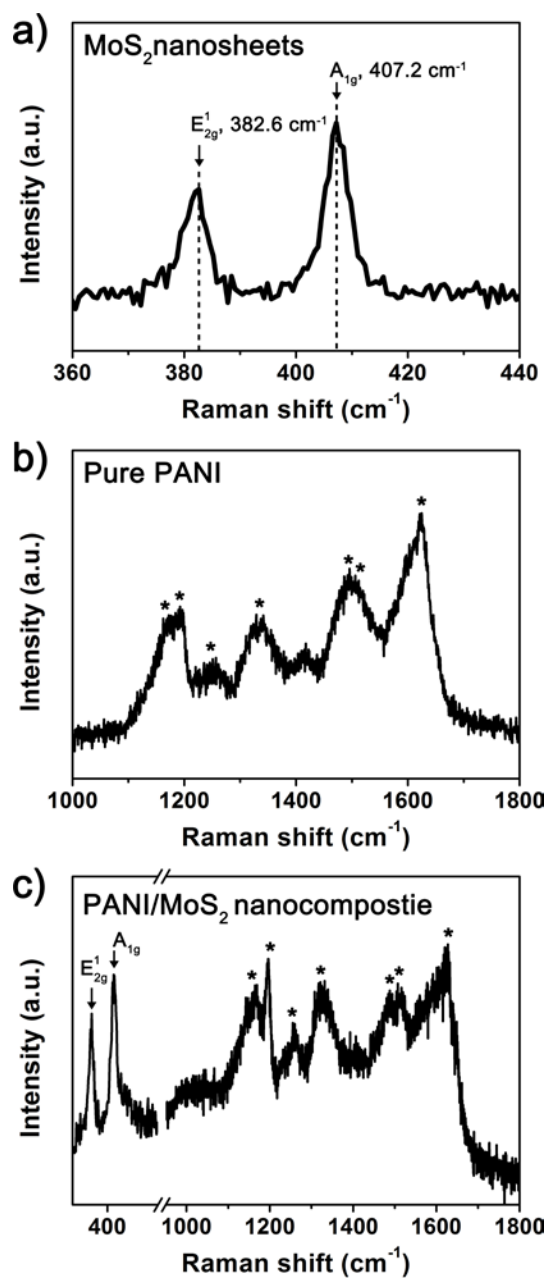


**Figure 15.** Raman spectra of a) MoS<sub>2</sub> nanosheets, b) PANI, and c) PANI/MoS<sub>2</sub> nanocomposite.

at 382.6 and 407.2  $\text{cm}^{-1}$  (Figure 15a), corresponding to  $E_{2g}^1$  mode vibration originated from in-plane vibration of molybdenum (Mo) atom and sulphur (S) atoms in opposite directions and  $A_{1g}$  mode vibration related with the out-of-plane vibration of only S atoms in opposite directions [53,54]. It has been reported that layer number of  $\text{MoS}_2$  sample can be simply determined by measuring frequency difference between  $E_{2g}^1$  and  $A_{1g}$  modes because two Raman modes are very sensitive to thickness of the  $\text{MoS}_2$  sample [53]. The frequency difference of the  $\text{MoS}_2$  nanosheets prepared here was found to be 24.6  $\text{cm}^{-1}$ , corresponding to five-to-six-layered  $\text{MoS}_2$  nanosheet. This result indicates that bulk  $\text{MoS}_2$  has been completely exfoliated to five-to-six-layered  $\text{MoS}_2$  nanosheet [53]. Pure PANI shows its own intrinsic peaks at 1169, 1192, 1253, 1343, 1495, 1516, and 1623  $\text{cm}^{-1}$  (Figure 15b), assigned to C-H bending of benzenoid ring, C-H bending of benzenoid ring, symmetric C-N stretching, C-N<sup>+</sup> stretching, C=N stretching of the quinoid ring, C=C stretching vibration of quinoid ring, and C-C bending of benzenoid ring [3,55–57]. For PANI/ $\text{MoS}_2$  nanocomposite (Figure 15c), it displays Raman peaks of both  $\text{MoS}_2$  (382.1 and 406.8  $\text{cm}^{-1}$ ) and PANI components (1169, 1192, 1253, 1343, 1495, 1516, and 1623  $\text{cm}^{-1}$ ). The frequency difference of  $\text{MoS}_2$  in the PANI/ $\text{MoS}_2$  nanocomposite was measured to 25.2  $\text{cm}^{-1}$ , corresponding to five-

to-six-layered MoS<sub>2</sub>. These peaks point out that PANI has been polymerized on the five-to-six-layered MoS<sub>2</sub> nanosheet during the polymerization process. Next, electrical conductivity and electrochemical properties of the MoS<sub>2</sub> nanosheet, pure PANI, and PANI/MoS<sub>2</sub> nanocomposite were investigated. Firstly, the electrical conductivities of the samples were measured using the four-in-line probe method (measuring the voltage differences between horizontally separated two probes by applying constant current to horizontally separated two other probes). Pristine MoS<sub>2</sub> nanosheet and pure PANI exhibited the electrical conductivities of *ca.* 5.6x10<sup>-5</sup> and *ca.* 10.6 S cm<sup>-1</sup>, respectively (Figure 16). Interestingly, after the PANI is coated on the MoS<sub>2</sub> nanosheets, PANI/MoS<sub>2</sub> nanocomposite showed increased electrical conductivity of *ca.* 28.6 S cm<sup>-1</sup> (Figure 16), which is higher electrical conductivity than those of pristine MoS<sub>2</sub> and pure PANI. It has been clearly proven that the electrical conductivity of CPs is strongly affected by the alignment of the polymer chains [23]. When electron migrates in pelletized PANI/MoS<sub>2</sub> nanocomposite sample, the electron would majorly moves along the horizontally aligned PANI chains (Figure 14b). In contrast, for the case pure PANI, electrons would evenly diffuse along the both horizontal and vertical directions because the pure PANI interconnected randomly along horizontal and vertical directions (Figure 17). In this case, the vertical direction plays a role as obstacles for electron

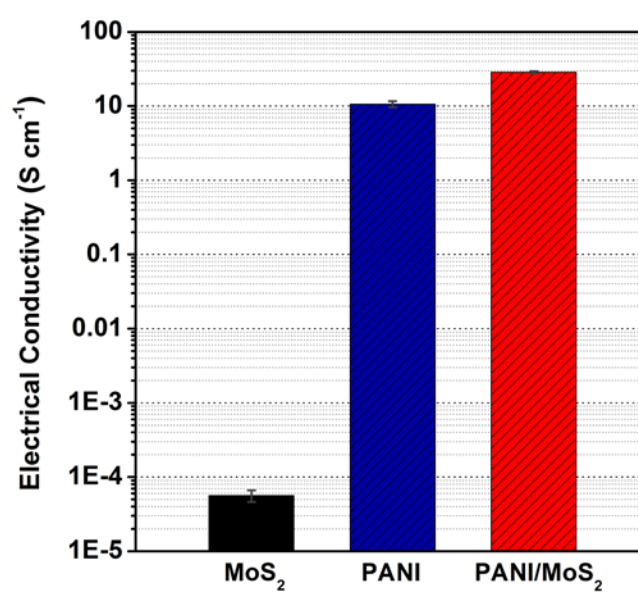


**Figure 16.** Electrical conductivity of the MoS<sub>2</sub> nanosheets, PANI, and PANI/MoS<sub>2</sub> nanocomposite.



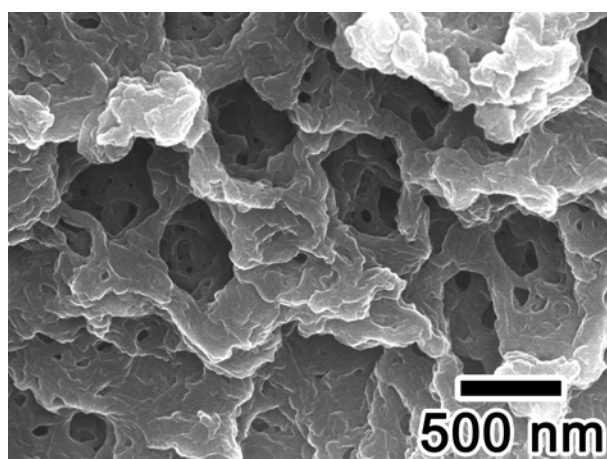


**Figure 17.** SEM image of pure PANI synthesized by SSDP.

migration in comparison with the case of PANI/MoS<sub>2</sub> nanocomposite. Thus, improved high electrical conductivity of PANI/MoS<sub>2</sub> nanocomposite might be attributed to well structural alignment of PANI chains along the horizontal direction on the flat MoS<sub>2</sub> nanosheet.

### **3.2.2. Supercapacitor based on PANI/MoS<sub>2</sub> nanocomposite**

Figure 18a presents the CV curves of MoS<sub>2</sub> nanosheet, PANI, and PANI/MoS<sub>2</sub> nanocomposite within a potential window from 0.0 to 0.8 V (vs AgCl/Ag) at a scan rate of 5 mV s<sup>-1</sup>. The MoS<sub>2</sub> nanosheet presents the low current response with distinctive peak at 0.8 V (Figure 19), reflecting low pseudo-capacitance behaviour. This peak might be attributed to the reduction of Mo atoms at the edge of the nanosheet. During the cathodic scan, holes are migrated from the electrolyte into n-type MoS<sub>2</sub> and recombined with electrons, resulting in sharp cathodic reduction peak at 0.8 V. In contrast, intensity of anodic current was very small due to the small number of holes in an n-type material MoS<sub>2</sub> [58]. In the case of the PANI, it exhibits larger current response than MoS<sub>2</sub> nanosheet with a couple of redox peaks (faradaic transformation of emeraldine to pernigraniline) [59] revealing the higher pseudo-capacitance of the PANI than MoS<sub>2</sub> nanosheet. For PANI/MoS<sub>2</sub> nanocomposite, it demonstrates highest current response with redox peaks, representing the

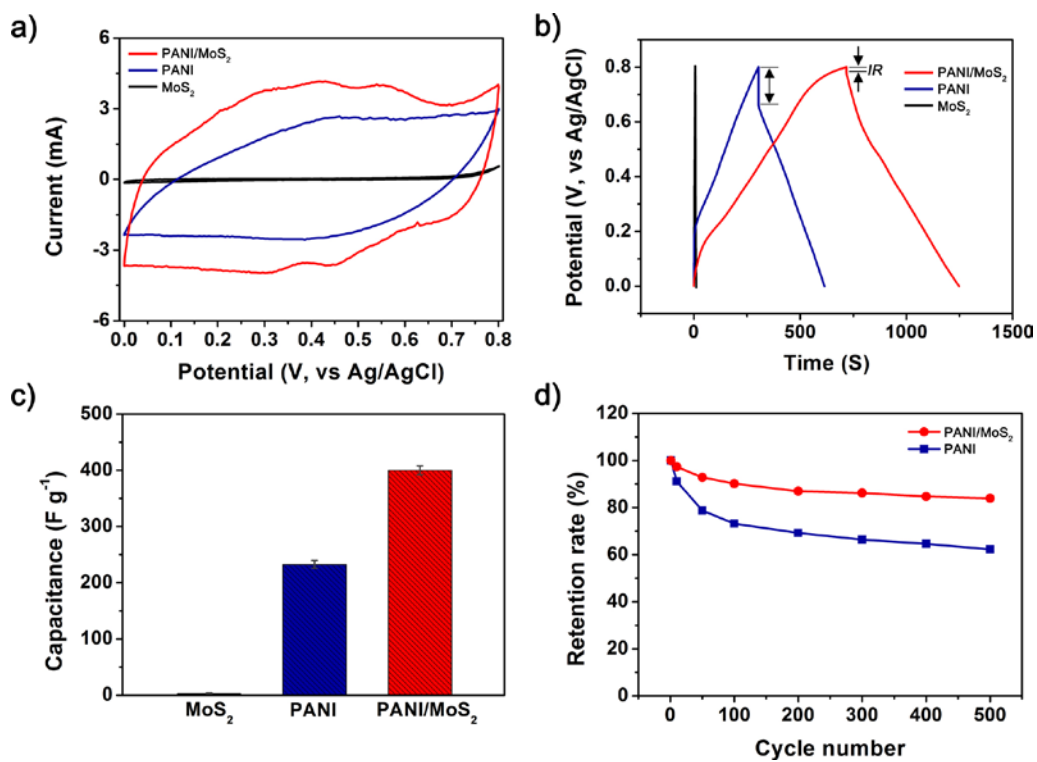


**Figure 18.** a) Cyclic voltammograms of MoS<sub>2</sub> nanosheet, PANI, and PANI/MoS<sub>2</sub> nanocomposite at a scan rate of 5 mV s<sup>-1</sup>, b) galvanostatic charge/discharge curves of MoS<sub>2</sub> nanosheet, PANI, and PANI/MoS<sub>2</sub> nanocomposite at a current density of 0.6 A g<sup>-1</sup>, c) gravimetric capacitances of MoS<sub>2</sub> nanosheet, PANI, and PANI/MoS<sub>2</sub> nanocomposite at a current density of 0.6 A g<sup>-1</sup>, and d) cycling stability of MoS<sub>2</sub> nanosheets, PANI, and PANI/MoS<sub>2</sub> nanocomposite at a current density of 0.6 A g<sup>-1</sup>.

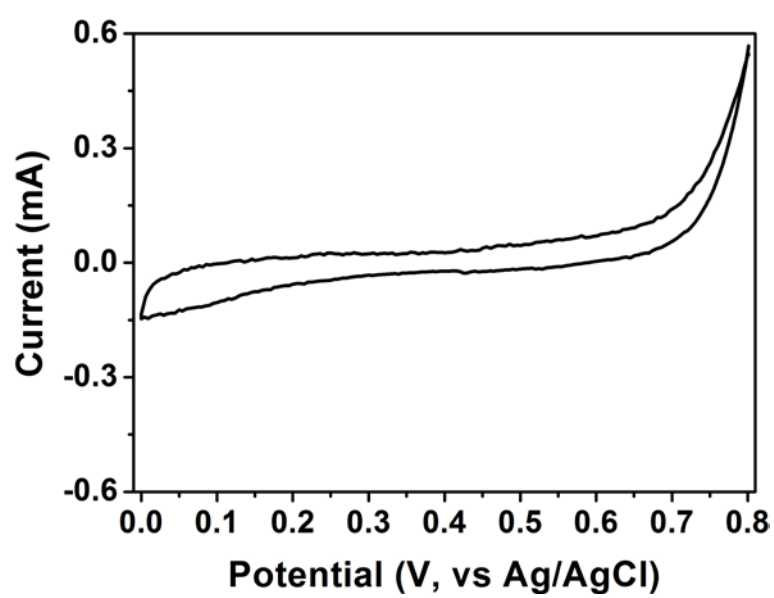


**Figure 19.** CV curve of pristine MoS<sub>2</sub> nanosheet at a scan rate of 5 mV s<sup>-1</sup>.

highest pseudo-capacitance of the PANI/MoS<sub>2</sub> nanocomposite.

Figure 18b illustrates galvanostatic charge/discharge curves of MoS<sub>2</sub> nanosheet, PANI, and PANI/MoS<sub>2</sub> nanocomposite within a potential window from 0.0 to 0.8 V (vs AgCl/Ag) at a current density of 0.6 A g<sup>-1</sup>. In accordance with the CV curves, galvanostatic charge/discharge curves show the highest capacitance of the PANI/MoS<sub>2</sub> nanocomposite and pseudo-capacitance behaviour of the all samples by representing longest discharging time of the PANI/MoS<sub>2</sub> nanocomposite and nonlinear-shaped galvanostatic charge/discharge curves of all samples (Figure 20). Additionally, galvanostatic charge/discharge curves depicts the lower “IR drop” of PANI/MoS<sub>2</sub> nanocomposite than pristine PANI, indicating that PANI/MoS<sub>2</sub> nanocomposite possesses lower internal resistance than PANI. Precise internal resistances of PANI/MoS<sub>2</sub> nanocomposite and PANI were calculated based on the “IR drop” and it was founded to be *ca.* 0.03 and 0.23 Ω g, respectively. For MoS<sub>2</sub> nanosheet, no “IR drop” was observed, indicating that internal resistance of MoS<sub>2</sub> nanosheet is extremely low. The charging and discharging process of supercapacitor electrode is related with migration of charge ions from electrolyte to the electrode and inter-electrode. During this migration, losses take place and these losses are expressed as internal resistance. [60]. From this point of view, it can be deduced that the extremely low internal resistance of

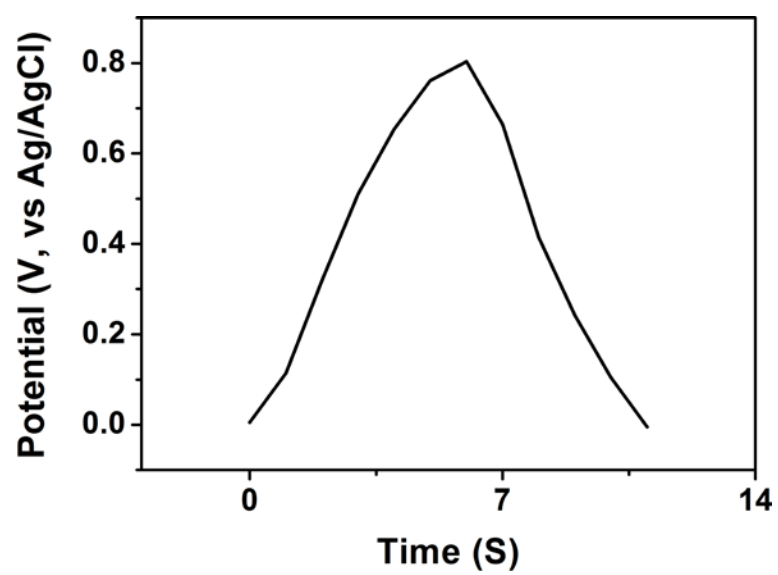


**Figure 20.** Galvanostatic charge/discharge curve of pristine MoS<sub>2</sub> nanosheet at a current density of 0.6 A g<sup>-1</sup>.

MoS<sub>2</sub> nanosheet is originated from the multilayer structure of MoS<sub>2</sub> nanosheets stacked in van der Waals force, enabling facile intercalation of proton (H<sup>+</sup>) ions [61]. In the cases for PANI/MoS<sub>2</sub> nanocomposite, the improved internal resistance would be owing to (1) well aligned honeycomb-like structure PANI on MoS<sub>2</sub> nanosheet and (2) introduce of MoS<sub>2</sub> nanosheet possessing extremely low internal resistance, both facilitating migration of charge carriers. Possessing low internal resistance is extremely important in supercapacitor electrode application for the long-lifetime. The higher internal resistance of electrode induces larger unwanted Joule-heating, resulting in short-lifetime of electrodes [42,62]. Therefore, this result implies that the PANI/MoS<sub>2</sub> nanocomposite can be suitably used as long-life time supercapacitor electrode.

In addition to internal resistance, accurate gravimetric capacitance was also measured from the galvanostatic discharging curves (Figure 18c). The MoS<sub>2</sub> nanosheet and PANI exhibited gravimetric capacitances of *ca.* 3 and *ca.* 232 F g<sup>-1</sup>, respectively. When MoS<sub>2</sub> nanosheet is combined with the PANI, PANI/MoS<sub>2</sub> nanocomposite demonstrates significantly improved gravimetric capacitance of *ca.* 400 F g<sup>-1</sup>, which is much higher value than pristine MoS<sub>2</sub> nanosheet and pure PANI. The capacitance of the supercapacitor electrode is crucially depends on following three factors: (1) types of the materials, (2)

electrical conductivity, and (3) specific surface area [1]. The PANI/MoS<sub>2</sub> nanocomposite consists of MoS<sub>2</sub> and PANI possessing pseudo-capacitance, thus, this nanocomposite possesses high potential that could exhibits large pseudo-capacitance. In this condition, highly electrical conductive PANI in the PANI/MoS<sub>2</sub> nanocomposite would provide high conductivity path to MoS<sub>2</sub> nanosheet and this would promote fast redox reaction of MoS<sub>2</sub> nanosheet, giving rise to improved high pseudo-capacitance of the PANI/MoS<sub>2</sub> nanocomposite.

Figure 18d plots cycling stabilities of the PANI, MoS<sub>2</sub> nanosheet, and PANI/MoS<sub>2</sub> nanocomposite. The retention rate of PANI decreased from 100 % to 62 % after 500 cycles. On the contrast, PANI/MoS<sub>2</sub> nanocomposite shows the improved charge retention rate of 84 %. The enhanced electrochemical stability of PANI/MoS<sub>2</sub> nanocomposite might be due to following reasons: (1) it has been known that MoS<sub>2</sub> possesses outstanding electrochemical stability like graphene, which is originated from the excellent mechanical strength of MoS<sub>2</sub> [61,63]. Consequently, improved electrochemical stability of PANI/MoS<sub>2</sub> nanocomposite might be originated from existence of highly electrochemically stable MoS<sub>2</sub> component in the PANI/MoS<sub>2</sub> nanocomposite. (2) while the PANI electrode is repeatedly charged and discharged during cycling stability test, the PANI chains are repeatedly bumped each other by



repeated swelling and shrinkage, leading to cracking and breaking of PANI chains, gradual loss in electrical conductivity, and decrease in capacitance [64]. For the case of PANI/MoS<sub>2</sub> nanocomposite, well aligned honeycomb-like structure PANI on flat MoS<sub>2</sub> nanosheet offers sufficient swelling volume along both vertical and horizontal directions, which would impede the cracking and breaking of PANI chains and enhance the cycling stability.

### **3.3. PANI/graphene film for flexible supercapacitor electrodes**

#### **3.3.1. Fabrication of PANI/RGO film**

Figure 21 shows a schematic illustration of the synthetic procedure of PANI/RGO film. First, the RGO powder was added to HCl solution and sonicated for 24 hr to obtain homogeneous dispersion. Then aniline monomer was added, keeping vigorous stirring. After stirring the above solution for 1 hr, chloroform was mixed to prevent the freezing of the reaction solution. When the temperature of the solution decreased to -9 °C in the chiller, the anilinium hydrochloride became partially insoluble in the aqueous phase and co-existed in both the aqueous and organic phase [16]. Thus, the hydrophobic part of the anilinium hydrochloride (phenyl group) adsorbed on the aromatic surface of the RGO by the  $\pi$ - $\pi$  interaction in the organic phase [65]. After addition of initiator, APS, the polymerization of aniline occurred on the surface of the RGO, and then PARG was obtained. After washing and drying, the primary dopant of ES-state PANI in PARG was removed by ammonia solution, resulting in De-PARG. After additional washing and drying, De-PARG was re-doped by CSA, and then Re-PARG was dissolved in *m*-Cresol/chloroform solvent. This secondary doping process is very helpful in changing the conformation of PANI chains from a compact coil to an expanded structure in

the solvent [66]. Furthermore, it is expected that RGO also induced the more

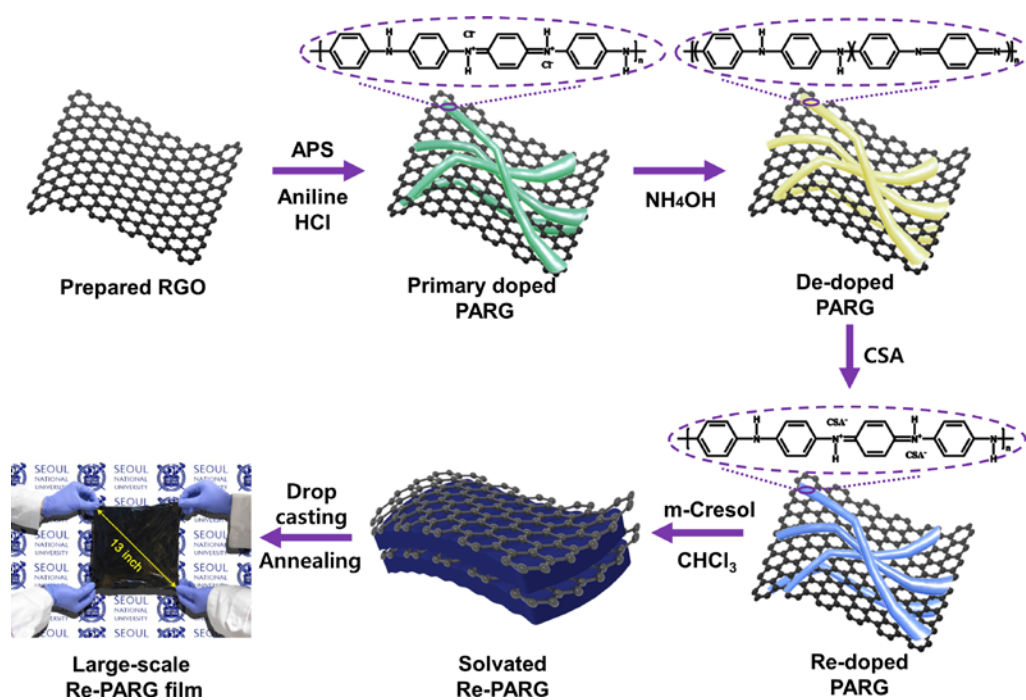
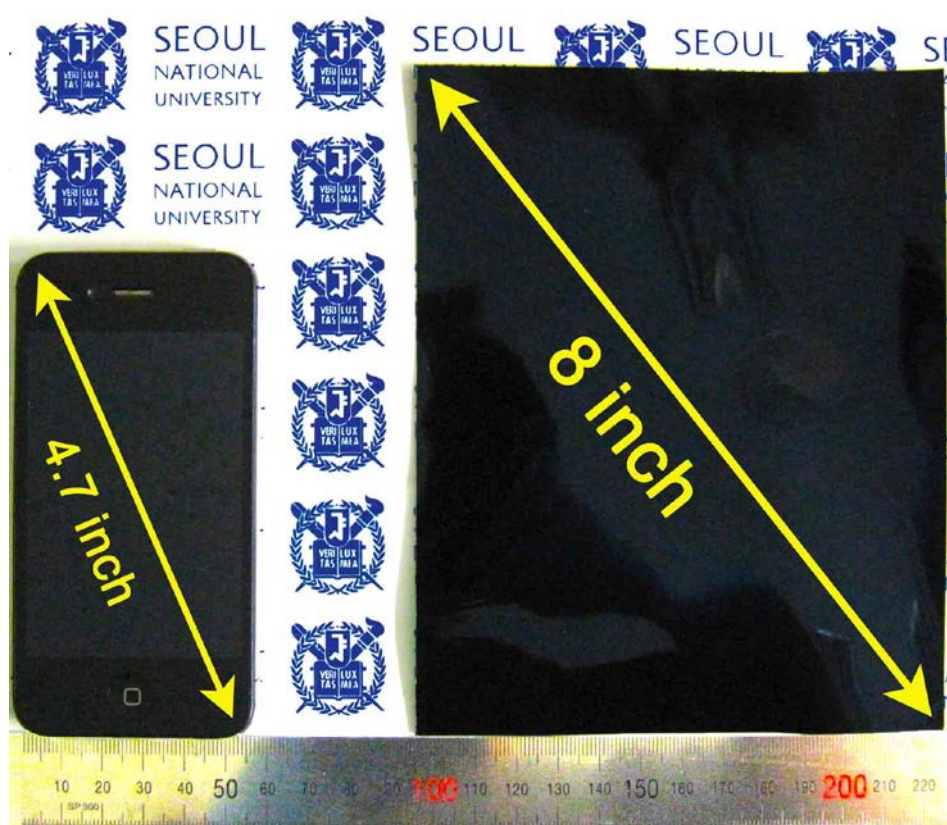


**Figure 21.** Schematic illustration of the sequential steps for fabricating large-scale Re-PARG film.

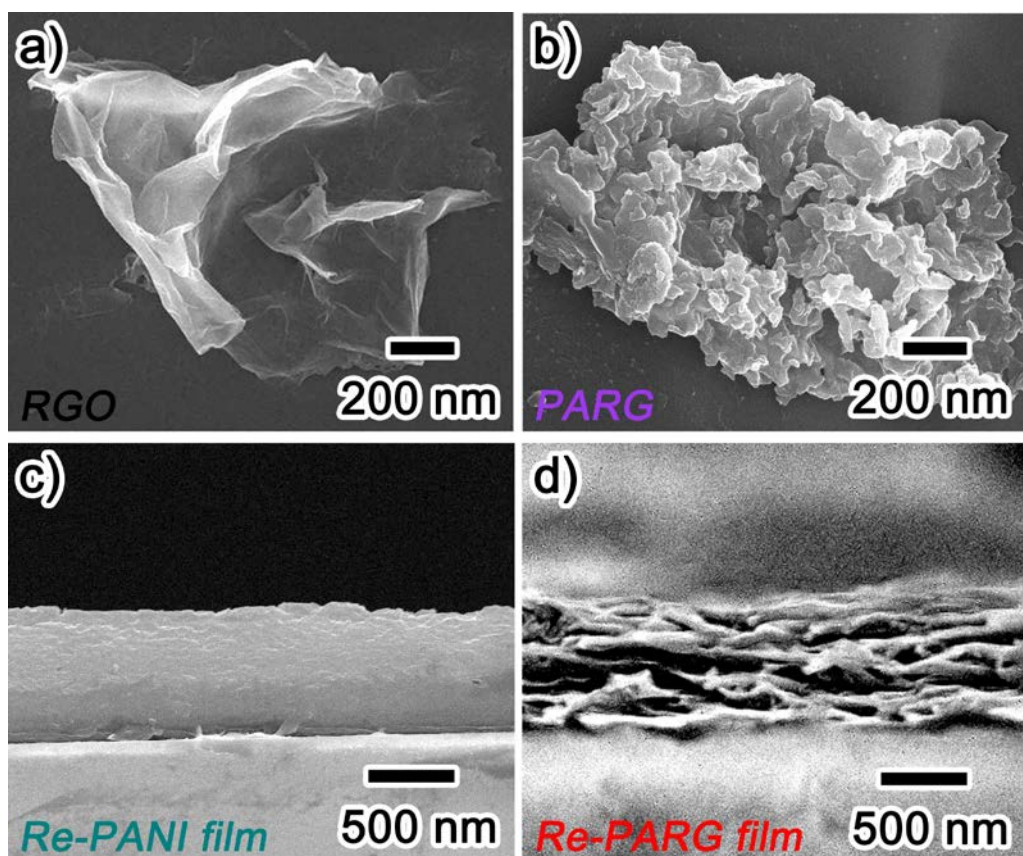
expanded coil conformation of PANI chains in the solution *via* strong  $\pi$ - $\pi$  interactions between the quinoid rings of the PANI chains and the basal planes of RGO. Finally, the prepared solution was cast onto a large-sized glass substrate (23 cm x 23 cm, 13 inch) and placed on a heat source to evaporate any residual solvent. Due to the high surface polarity and wettability of the m-cresol solvent, the prepared solution was well attached to the glass substrate [66,67]. After the annealing process, as shown in the last picture of Figure 21, we obtained the large-scale Re-PARG film (23 cm x 23 cm, 13 inch). Additionally, we were able to fabricate the smaller sized film (16 cm x 13 cm, 8 inch) easily by changing the size of the glass substrate (Figure 22), demonstrating the great advantage of the solution process for producing the scalable film.

Figure 23a–d illustrate the SEM images of pristine RGO, PARG, Re-PANI film, and Re-PARG film, respectively. As shown in Figure 23a, pristine RGO exhibits the wrinkled and silk-like structure related with the intrinsic characteristics of graphene [59,68]. The TEM images of RGO (Figure 24a) additionally show the thin and transparent two-dimensional morphology with the size of several micrometers, suggesting that few layers of RGO were utilized to synthesize the Re-PARG film. The SEM and TEM images of the

PARG (Figure 23b and Figure 24b) clearly show that the PANI was uniformly



**Figure 22.** Digital camera images of (left) electronic device (10.5 cm x 5.5 cm, 4.7 inch) and (right) Re-PARG film (16 cm x 13 cm, 8 inch) with a ruler below the electronic device and film for scale. The scale bars of ruler represent mm.



**Figure 23.** SEM images of a) Pristine RGO, b) PARG, c) Cross sectional view of Re-PANI film and d) Re-PARG film.

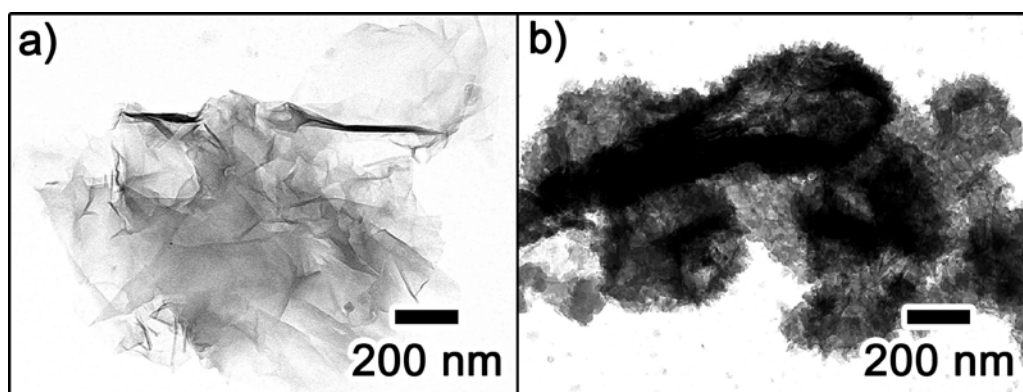


**Figure 24.** TEM images of a) Pristine RGO, b) PARC.

and successfully polymerized on the surface of the few micrometer sized-RGO, which could be beneficial for the homogeneous dispersion of the Re-PARG in the solution. The cross-sectional image of the Re-PARG film (Figure 23d) clearly shows that the RGO components are laterally intercalated with the PANI component, while the Re-PANI film displays a relatively smooth cross-section (Figure 23c). The RGO-intercalated structure of the Re-PARG film is probably attributable to the homogeneous dispersion of the Re-PARG in the solution and the strong  $\pi$ - $\pi$  interactions between the graphitic surface of the RGO and the quinoid rings of the PANI backbone.

Raman spectroscopy was used to analyse the structural changes of the PANI component during de-doping and re-doping processing and to measure the vibrational spectra of nonpolar bonds, such as carbon-carbon interactions between the PANI backbone and the basal planes of RGO. The Raman spectra of the GO, RGO, Re-PARG film, De-PARG, PARG and PANI (ES-state) samples are shown in Figure 25a (the important peaks are marked with black dots). As shown in Figure 25a, structural changes occurred during the chemical processing from GO to RGO in the exfoliation/reduction step and during the transition of PARG to Re-PARG film in the de-doping/re-doping process. Both GO and RGO display two prominent Raman-active peaks at  $1330\text{ cm}^{-1}$



assigned to D mode corresponding to the structural defects and at  $1590\text{ cm}^{-1}$

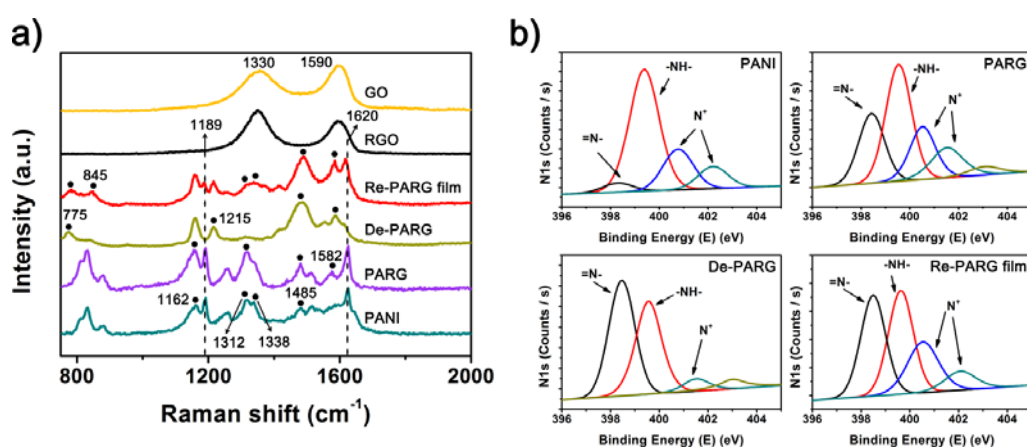


**Figure 25.** a) Raman spectra of GO, RGO, Re-PARG film, De-PARG, PARG and PANI (ES state), b) N 1s XPS spectra of PANI (ES state), PARG, De-PARG and Re-PARG film.

corresponding to the G mode related to the first-order scattering of the  $E_{2g}$  mode observed for  $sp^2$ -carbon domains [69,70]. The Raman spectra of RGO exhibit the increased intensity ratio of the D band to G band ( $I_D/I_G$ ) compared to that of GO, suggesting that the reduction process increased the defect content or edge area in RGO sheets [69]. In addition to the reduction process, the decreased size of the graphene sheets might also cause the structural defect, leading to an increase of  $I_D/I_G$  [59,69]. The Raman spectra of pure PANI show the distinctive vibrations of C-C stretching of the para-distributed benzenoid ring, C=N stretching of the quinoid ring, C=N stretching of the quinoid ring, C-N<sup>+</sup> stretching in polaron form (cationic amine units of the benzenoid ring), C-N<sup>+</sup> stretching in bipolaron form (cationic imine units of the quinoid ring), C-N stretching, C-H bending of the benzenoid ring, C-H bending of the quinoid ring, benzenoid ring deformation, and C-H bending of the quinoid ring and quinoid ring deformation at 1620  $cm^{-1}$ , 1513  $cm^{-1}$ , 1485  $cm^{-1}$ , 1338  $cm^{-1}$ , 1312  $cm^{-1}$ , 1255  $cm^{-1}$ , 1189  $cm^{-1}$ , 1162  $cm^{-1}$ , 878  $cm^{-1}$ , and 832  $cm^{-1}$ , respectively [69,71–75]. These peaks show the coexistence of quinoid and benzenoid structures in PANI ES. After aniline monomers were polymerized on the RGO, the PARG presented four distinguishable peaks that differed from those seen in pure PANI: Increase in the intensity of quinoid ring-related vibrations at 1485, 1312,

and  $1162\text{ cm}^{-1}$  corresponding to the C=N stretching of the quinoid ring, C-N<sup>+</sup> stretching in bipolaron form and C-H bending of the quinoid ring, and appearance of the C=C stretching vibrational mode of the quinoid ring at  $1582\text{ cm}^{-1}$  [73]. These peaks in the PARG probably result from the strong intermolecular  $\pi$ - $\pi$  stacking, which causes the overlapping of P<sub>z</sub> orbitals between the basal planes of the RGO and the quinoid rings of the PANI backbone [76]. Thus, it can be assumed that the aniline monomers were successfully polymerized on the RGO *via* the strong  $\pi$ - $\pi$  stacking between RGO and PANI. In the Raman spectra of De-PARG, the peaks of C-N<sup>•+</sup> and C-N<sup>+</sup> corresponding to  $1338$  and  $1312\text{ cm}^{-1}$  almost disappeared, whereas the peaks at  $1215$  and  $775\text{ cm}^{-1}$  were newly appeared. The vibrational bands at  $1215$  and  $775\text{ cm}^{-1}$  were attributed to C-N stretching in the EB form of PANI and quinoid ring deformation. [76,77]. Additionally, it was also observed that the peak at  $1620\text{ cm}^{-1}$  corresponding to the C-C stretching of the para-distributed benzenoid ring significantly decreased, while the C=C stretching band of the quinoid ring and the C=N stretching vibration of the quinoid ring, corresponding to  $1582\text{ cm}^{-1}$  and  $1485\text{ cm}^{-1}$ , increased considerably. The EB form of PANI is known to have a higher imine/amine and quinoid ring/benzenoid ring ratio than the ES form [66,69,78–81]. Moreover, it should also be noted that PANI ES significantly losses its bipolaronic and polaronic structure by de-protonation [69,82,83].

Consequently, with the emergence of the new vibration related with the EB form of PANI ( $1215\text{ cm}^{-1}$ ), the observed peaks in De-PARG clearly reveal that the ES-state of PANI on the RGO turned to the EB-state by the de-doping process. After De-PARG was re-doped by CSA, four different features appeared in the spectra of Re-PARG film: (1) Re-emerged bands of the bipolaron and polaron form and C-H bending of the benzenoid ring at  $1310\text{--}1340$  and  $1189\text{ cm}^{-1}$ ; (2) New appearance of an amine deformation peak at  $845\text{ cm}^{-1}$ ; (3) Increase in the intensity of the C-C stretching vibrational mode of the para-distributed benzenoid ring and the C=C stretching band of the quinoid ring at  $1620$  and  $1582\text{ cm}^{-1}$ ; (4) Up-shifted peaks of the C=N stretching of the quinoid ring and quinoid ring deformation at  $1489$  and  $782\text{ cm}^{-1}$  from the peaks at  $1485$  and  $775\text{ cm}^{-1}$ . The re-emerged benzenoid ring peak ( $1189\text{ cm}^{-1}$ ), newly appeared amine deformation peak ( $845\text{ cm}^{-1}$ ), [71] and increased benzenoid ring peak ( $1620\text{ cm}^{-1}$ ) obviously reflect the increased doping level of PANI in the Re-PARG film. Additionally, the re-emerged bipolaron and polaron bands provide crucial evidence of the successful re-protonation of the PANI component in the Re-PARG film. Thus, it can be assumed that the up-shift of the two quinoid ring vibrations at  $782$  and  $1489\text{ cm}^{-1}$  can be attributed to the changed backbone structures of PANI in the Re-PARG film. It is known that the quinoid ring and imine nitrogen atoms in the PANI backbone are substantially converted to

benzenoid ring and amine nitrogen atoms when the EB state of the PANI turns to the ES state. [66,79,80] However, the quinoid ring vibrations at 1582, 1489, 1162 and 782  $\text{cm}^{-1}$  did not disappear even after the re-doping process, but dominated the overall Raman spectrum of the Re-PARG film. Furthermore, the peak at 1582  $\text{cm}^{-1}$  corresponding to the C=C stretching band of the quinoid ring was slightly increased. As described above, the graphitic surface of the RGO interacts strongly with the quinoid ring of the PANI through the  $\pi$ - $\pi$  stacking. Consequently, the overlapping of the  $P_z$  orbitals of the quinoid rings of the PANI with the aromatic surface of RGO would result in the strong quinoid ring peaks in the Re-PARG film.

XPS analysis was also conducted to investigate the structural change of PANI in the de-doping/re-doping process and the specific interaction between RGO and the PANI backbone (Figure 25b). In this study, N1s spectra of PANI (ES state), PARG, De-PARG and Re-PARG film samples were collected. In the N1s spectra of PANI sample, the peak at 398.5 eV (black line) corresponds to quinoid imine (-N=), and the more prominent peak at 399.5 eV (red line) corresponds to benzenoid amine (-NH-) in the PANI backbone [84,85]. An additional two minor peaks at 400.8 eV and 402.2 eV (blue and dark cyan lines) correspond to positively charged imine in the bipolaron state and protonated amine in the polaron state [86,87]. These spectra demonstrate the

typical structure of the PANI in ES form.

After the polymerization of PANI on RGO, some structural changes were observed in the PARG. Increased XPS peak signal area of the quinoid imine peak at 398.4 eV, from 0.38 % of the overall PANI signal area to 1.57 % of the PARG signal area, was observed. The peak at 400.5 eV, which represents charged imine, is also slightly increased. The strong  $\pi$ - $\pi$  stacking between the PANI backbone and RGO might have caused an increase in the quinoid imine peaks.

The N1s spectra of De-PARG sample shows increased peak at 398.5 eV and diminished peak at 399.5 eV, which correspond to quinoid imine and benzenoid amine in the backbone, while only one minor peak at 401.5 eV for the protonated amine part [69] is shown. Increased imine peak is due to the ammonium hydroxide addition and following de-protonation of amine in the PANI ES backbone [66,69,78–81]. Additionally, when the ES form of PANI changed to the EB form, it possessed almost no charge in the backbone [69,82,83], resulting in the disappearance of the positively charged imine peak at 400.5 eV and the attenuated peak of protonated amine at 401.5 eV.

After De-PARG was re-doped by CSA, the XPS analysis on the Re-PARG film suggests that the charged bipolaron structure (re-emerged blue peak at 400.5 eV) and polaron structure (increased dark cyan peak at 402.2 eV) were

restored. Thus, it could be assumed that the ES form of the PANI backbone was successfully re-established [82,88]. The re-doping of the EB state of PANI is known to induce a substantial transition of imine nitrogen atoms to amine nitrogen atoms in the PANI backbone [66,79,80]. However, the quinoid imine (-N=) peak at 398.5 eV considerably remained even after the re-doping process. Therefore, this result suggests that the specific  $\pi$ - $\pi$  interaction between the quinoid ring of the PANI and the graphitic surface of the RGO exists and the interaction leads to preservation of the quinoid imine structure in the Re-PARG sample, which is in accordance with the previous Raman analysis.

As described above, it has been found that PANI chains re-doped by CSA could change their molecular conformation possessing the mobility with its counter-ion in the *m*-Cresol/chloroform co-solutions [66]. Additionally, it is known that when the interaction between polymer and solvent is larger than the interaction between polymer and polymer, more linear polymer chain conformation is preferred due to the increased possibility that the polymer chains will interact with the solvent [66]. Thus, considering these facts, it is expected that the strong interaction between the PANI and RGO ( $\pi$ - $\pi$  interaction) effectively helps PANI chains possess the more linear conformation, leading to increased crystallinity along with improved electrical conductivity. In the next step, we measure the electrical conductivity and

crystalline structure of the films to achieve an in-depth insight into the role of the RGO in determining the conformation of PANI chains and overall crystalline structure and electrical conductivity of the films.

In order to elucidate the role of the RGO in determining the electrical properties and crystalline structure of the composite film, the De-PARG samples (De-PARG 1-3) were first prepared with various mass ratio of De-PANI to RGO. The prepared De-PARG 1-3 samples were used in producing the Re-PARG 1-3 films without any weight ratio change of either component. TGA was performed to assess the precise weight percentages of the PANI component in the De-PARG 1-3 samples under air flow at a heating rate of  $10\text{ }^{\circ}\text{C min}^{-1}$  (Detailed description in Figure 26). Based on these TGA data, the weight percentage of PANI component was calculated as 88, 76 and, 60 % for De-PARG 1, 2, and 3, respectively. The four-probe method was conducted to measure the electrical conductivity of the samples. The Re-PANI film and RGO were prepared as control materials. Figure 27a presents the electrical conductivities of the Re-PARG films and control samples. The electrical conductivities of Re-PANI film, Re-PARG 1 film, Re-PARG 2 film, Re-PARG 3 film, and RGO were measured as *ca.* 580, 762, 906, 298, and  $46.5\text{ S cm}^{-1}$ , respectively. Starting from the Re-PANI film, the electrical conductivity of the film increased to the maximum of  $906\text{ S cm}^{-1}$  (Re-PARG 2 film) as the weight



percentage of the RGO increased to 24 %, while decreased value of

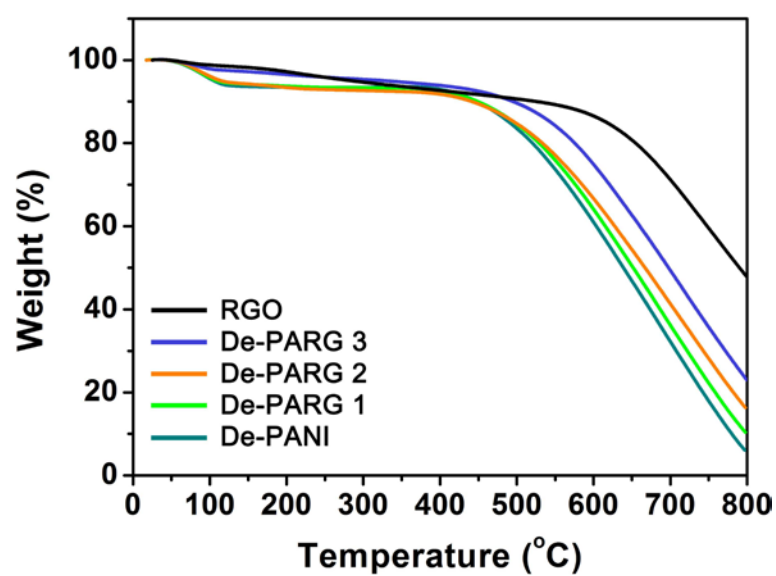


**Figure 26.** TGA curves of RGO, De-PARG 1-3 composites with different weight percentage of De-PANI, and De-PANI.

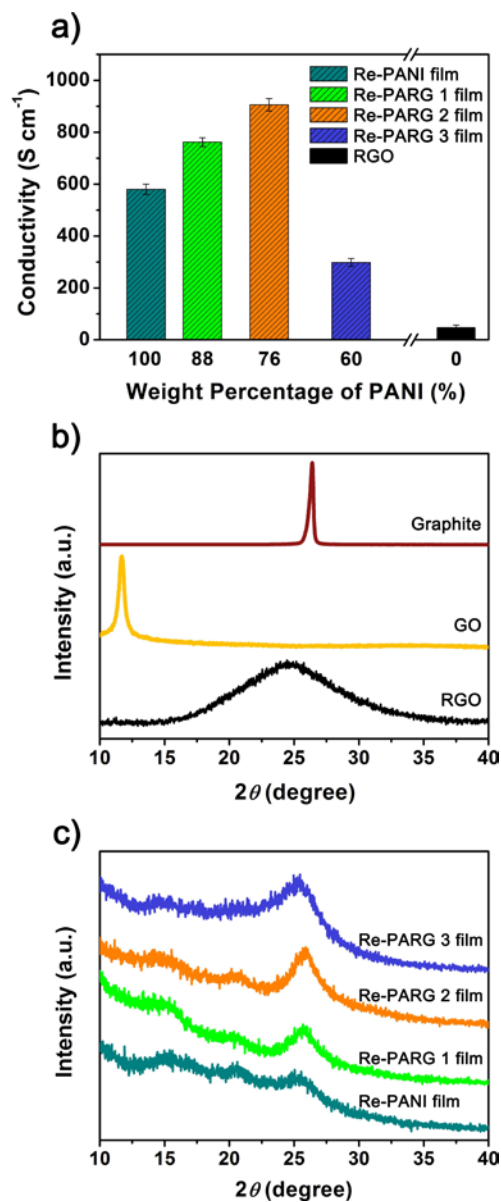


**Figure 27.** a) Electrical conductivity of Re-PANI film, Re-PARG 1-3 films, and RGO displayed as function of the weight percentage of PANI component; b) XRD patterns of graphite, GO, and RGO; c) XRD patterns of Re-PARG 1-3

films and Re-PANI film.

conductivity was measured in Re-PARG 3 film. Additional TGA and XRD analysis were conducted to measure the remaining solvent in the film and ascertain the effect of the solvent evaporation on the electrical performance of the film over time. The as-prepared Re-PARG 2 film and Re-PARG 2 film after keeping for 150 days were used in both TGA and XRD analysis and the Re-PARG 2 powder before mixing with m-cresol and chloroform was used as a control in TGA test (Detailed description in Figure 28). The weight percentage of the as-prepared Re-PARG 2 film and the Re-PARG 2 film after keeping for 150 days were measured to be as *ca.* 1.25 wt % and *ca.* 0 wt %, indicating that negligible amount of solvent was remained on the film after annealing process and solvent evaporation is occurred with time. The XRD analysis illustrates that enhanced crystalline structure of the film was maintained even after storing for 150 days. Therefore, it is considered that crystalline structure was not affected by solvent evaporation and performance of the material is well maintained over time.

Figure 27b shows the XRD patterns of the graphite, GO and RGO. The XRD pattern of graphite presented a typical (002) narrow peak [89] at  $2\theta = 26.5^\circ$ , corresponding to a d-spacing of *ca.* 3.36Å. In the case of GO, a sharp diffraction peak was observed at  $2\theta = 11.65^\circ$  (d-spacing = *ca.* 7.59Å), which

can be assigned to the (001) reflection peak [59]. The increase in the interlayer

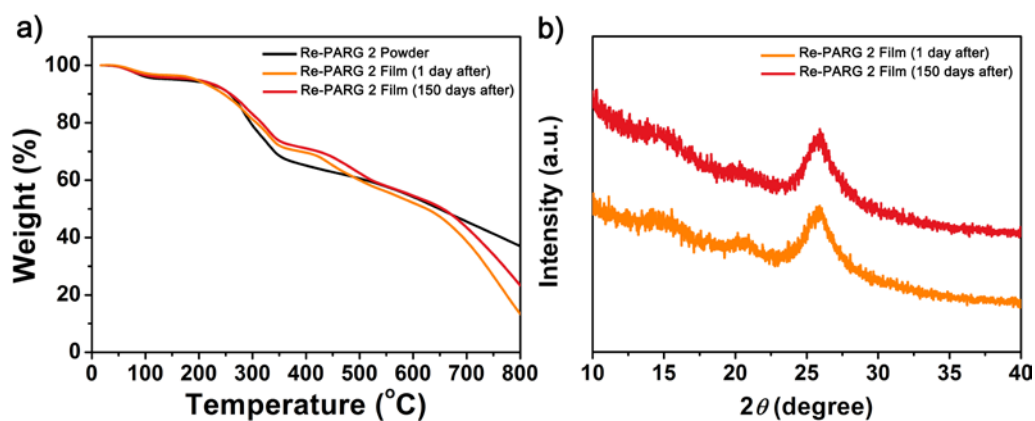


**Figure 28.** a) TGA curves of Re-PARG 2 powder, as-prepared Re-PARG 2 film and Re-PARG 2 film after storing for 150 days and b) XRD patterns of as-prepared Re-PARG 2 film and Re-PARG 2 film after storing for 150 days.

distance from *ca.* 3.36 Å for graphite to *ca.* 7.59 Å for GO reflects successful oxidation of graphite [70]. After ultra-sonication and reduction steps, the (001) reflection peak of GO disappeared, and one broad peak centered at 24.58° (d-spacing = *ca.* 3.62Å) appeared in the XRD spectra of RGO, illustrating that the GO was efficiently reduced into RGO [64].

Figure 27c represents the XRD patterns of Re-PARG 1-3 films and Re-PANI film. The Re- PANI film shows three peaks centered at  $2\theta = 15.3^\circ$ ,  $20.5^\circ$ , and  $25.6^\circ$  (d-spacings= *ca.* 5.8, 4.3, and 3.5 Å) on the broad background, revealing the semi-crystalline nature of the PANI. By increasing the weight percentage of RGO from 0 % (Re-PANI film) to *ca.* 12 % (Re-PARG 1 film), the peaks at  $15.3^\circ$  and  $20.5^\circ$  decreased along with the decrease in the broad background, whereas the peak at  $25.6^\circ$  increased. When the weight percentage of RGO reached 24 % (Re-PARG 2 film), with the maximum electrical conductivity ( $906 \text{ S cm}^{-1}$ ) among the films, the peaks at  $15.3^\circ$ ,  $20.4^\circ$  and the broad background mostly disappeared and the diffraction pattern of the Re-PARG 2 film was dominated by the peak at  $25.6^\circ$ . This indicates an increase in the crystalline phase of the film and strengthened stacking along the specific direction. More specifically, these results have following three implications. First, the disappearance of the intrinsic peak of RGO ( $24.58^\circ$ ) in the XRD

patterns of the Re-PARG 1 and 2 films clearly indicates that the RGO is properly intercalated into PANI chains. Second, it is known that the d-spacing of *ca.* 3.5 Å (25.6°) is the face-to-face  $\pi$ - $\pi$  stacking distance between neighboring phenyl rings in the crystalline structure of the PANI [17,90]. Thus, the increase in the intensity of the peak at 25.6° along with the decrease in the intensity of the peaks at 15.3°, 20.5° and the broad background reflect that  $\pi$ - $\pi$  inter-chain stacking between the phenyl rings of the PANI chains was intensified. Third, based on the strengthened peak (25.6°) of the Re-PARG 1 and 2 films with the increase of RGO contents, it is considered that the basal planes of RGO and phenyl rings also form  $\pi$ - $\pi$  stacking with a distance of 3.5 Å. Considering these results, the mechanism of improved electrical conductivity of Re-PARG 1 and 2 films could be explained in the following manner: The chemical structure of the micro-meter sized RGO consists of a number of aromatic rings. Thus, when PANI and RGO co-exist in the solution, it is expected that the PANI chains would strongly interact with the aromatic structure of RGO by the  $\pi$ - $\pi$  overlapping of the basal planes of the RGO and the quinoid rings of the PANI, resulting in more expanded coil conformation of the PANI chains. Then, the PANI chains expanded by the RGO would induce more planar stacking with nearby PANI chains sequentially. In this way, the PANI chains would form the more planar chain conformation and compact

packing structure. This compact packing of PANI chains would inhibit the considerable ring rotations ( $\pi$ -conjugation defects) of the phenyl rings from the plane of the backbone, leading to the improved  $\pi$ - $\pi$  interactions, extensive three-dimensional delocalization of charge, and increase in the crystallinity and electrical conductivity [66,88]. This compact crystalline structure of PANI chains with RGO is proposed as a pictorial scheme in Figure 29 where PANI chains are located between RGO.

However, as the weight percentage of RGO further increase to 40 % in the Re-PARG 3 film, the XRD pattern showed an increase in broad background, re-emerged peaks at  $15.3^\circ$  and  $20.5^\circ$ , and a weak change in peak intensity at  $25.6^\circ$ . This indicates that an overall decrease in the crystallinity of the film has occurred, and the PANI chains are not aligned in one direction after the specific weight percentage of RGO (40%). Based on the highly disordered crystalline structure of the pristine RGO (Figure 27b), the increase in the amorphous region in the Re-PARG 3 film is considered as a result of the increased influence of the poorly ordered structure of the RGO. This increase in the amorphous region of the film would result in a shorter mean free path and worsened carrier transport, leading to the decrease in the electrical conductivity of the film [23,90]. Consequently, the XRD analysis demonstrates that RGO in the composite favorably or unfavorably changes the crystalline structure of

PANI depending on PANI/RGO weight ratios, leading to the increase or

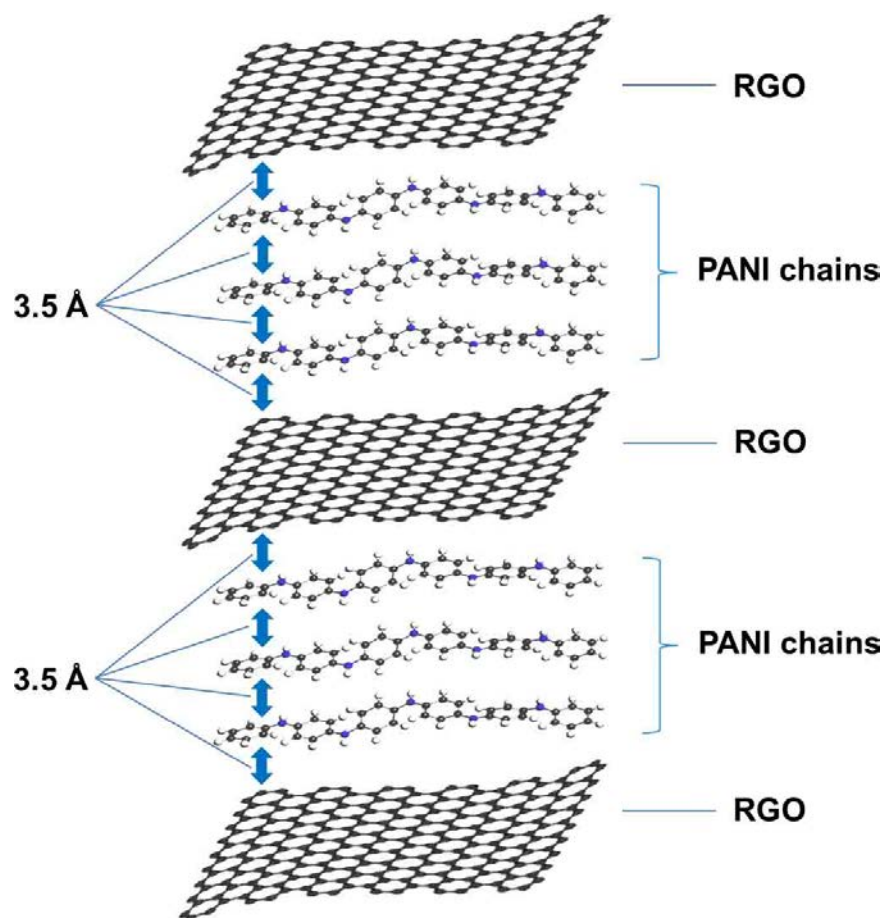


**Figure 29.** Schematic representation of interaction between RGO and PANI chains leading to compact packing of the PANI chains with RGO and extensive three-dimensional delocalization of the charge.



decrease in the electrical conductivities of PANI/RGO hybrid films. Most interesting part of XRD analysis is that the strong  $\pi$ - $\pi$  interactions of RGO with the quinoid rings of the PANI chains increase the electrical conductivity and crystallinity of the PANI/RGO hybrid film, which is greater than both RGO and PANI. To investigate the advantages of enhanced electrical conductivity and crystallinity of Re-PARG film as a supercapacitor electrode, electrochemical analysis was performed to the Re-PARG 2 film.

### **3.3.2. Flexible supercapacitor based on PANI/RGO film**

CV and galvanostatic charge/discharge analysis were conducted in 1 M H<sub>2</sub>SO<sub>4</sub> electrolyte with three-electrode system to evaluate electrode performance. For a comparison, the Re-PANI film and pristine RGO were also used as electrodes for supercapacitor. Figure 30a illustrates the CV curves of the Re-PARG film, Re-PANI film and RGO at a scan rate of 5 mV s<sup>-1</sup> from 0 to 0.8 V. The CV curve of RGO shows the rectangular shape without any redox peaks, reflecting the good charge propagation and EDL capacitance of the carbon materials [40,64,69]. On the contrary, two pairs of broad redox peaks were observed for the Re-PARG and Re-PANI films, revealing the existence of the pseudo-capacitive PANI component in the Re-PARG film. [69]. The two observed redox peaks originated from its redox transitions between the

leucoemeraldine form (semiconducting state), the ES form (conducting state)

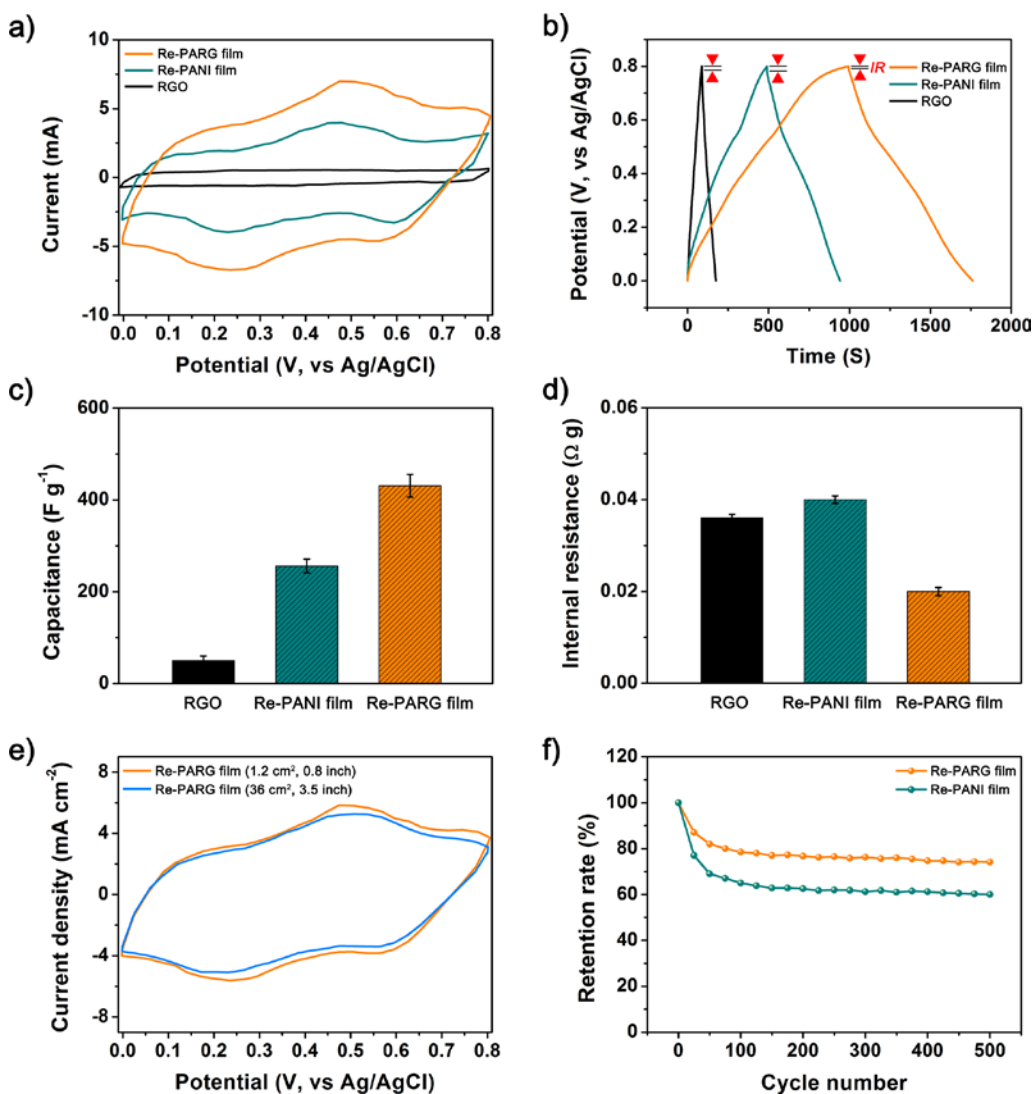


**Figure 30.** a) CV curves of Re-PARG film, Re-PANI film and RGO electrodes at a scan rate of  $5 mV s^{-1}$  between 0 and 0.8 V in 1M  $H_2SO_4$  solution; b) Galvanostatic charge/discharge curves of Re-PARG film, Re-PANI film and

RGO electrodes at current density of  $0.45 \text{ A g}^{-1}$  in  $1\text{M H}_2\text{SO}_4$  solution; c) Gravimetric capacitances of RGO, Re-PANI film and Re-PARG film electrodes at current density of  $0.45 \text{ A g}^{-1}$ ; d) Internal resistances of RGO, Re-PANI film and Re-PARG film electrodes estimated from the IR drop at a current density of  $0.45 \text{ A g}^{-1}$ ; e) Comparison of CV curves between different sized ( $1.2$  and  $36 \text{ cm}^2$ ) Re-PARG film electrodes at a scan rate of  $5 \text{ mV s}^{-1}$ ; f) Cyclic stability of Re-PARG film and Re-PANI film electrodes as a function of cycle number at a current density of  $0.45 \text{ A g}^{-1}$ .

and the Faradic transformation of emeraldine/permanganine [59,64,90]. Additionally, the CV curve of the Re-PARG film showed the largest CV loop area with the highest current response, demonstrating the larger specific capacitance of the Re-PARG film than the RGO and the Re-PANI film [40,91]. This phenomenon suggests that the RGO in the Re-PARG film is a crucial factor for enhanced capacitance compared with that of the RGO and the Re-PANI film.

To further elucidate the electrochemical behavior of the Re-PARG film, Re-PANI film and RGO, the galvanostatic charge/discharge test was carried out at a current density of  $0.45 \text{ Ag}^{-1}$  from 0 to 0.8 V in 1M  $\text{H}_2\text{SO}_4$  electrolyte. As shown in Figure 30b, the galvanostatic charge/discharge curve of the RGO exhibits a symmetric triangular shape, indicating that its capacitance originates from the EDL capacitance, [42] as described above. In contrast, the discharge curve of the Re-PARG film exhibits two distinct voltage stages: *ca.* 0.8–0.6 V and *ca.* 0.6–0 V, respectively. The first stage, with a relatively short discharging duration, is attributed to EDL capacitance, whereas the second stage, with a much longer discharging duration, is due to the combination of EDL and faradaic capacitances of the PANI component in the film [42]. The discharge curve of the Re-PANI film also represents a shape similar to that of

the Re-PARG film. However, the Re-PARG film exhibits a much longer discharging time and less vertical voltage drop at the beginning of the discharge curve than the Re-PANI film, indicating that the Re-PARG film possesses much higher specific capacitance and smaller internal resistance than the Re-PANI film [90,92]. Possessing low internal resistance as a supercapacitor is a crucial factor for improving the capacitance of the materials and reducing unwanted power consumption [68,93].

The precise gravimetric capacitances (Figure 30c) and internal resistances (Figure 30d) of all samples were calculated from the galvanostatic discharge curves [64,94] and vertical voltage drop at the initial point of each discharge curve [90] (Detailed description in experimental section). The RGO, Re-PANI film, and Re-PARG film exhibit the gravimetric capacitances of 50, 256, and 431 F g<sup>-1</sup> and internal resistances of 0.036, 0.04, and 0.02 Ω g, respectively. The Re-PARG film and the Re-PANI film show much higher gravimetric capacitances than the RGO electrode. Generally, pseudo-capacitance is much higher than EDL capacitance, because pseudo-capacitive materials take advantage of fast redox reactions by utilizing whole mass [1,95–97]. Thus, though the RGO displays lower internal resistance than the Re-PANI film electrode, the RGO illustrates the lowest gravimetric capacitance among all the samples due to the absence of pseudo-capacitive materials [42]. Interestingly,

without any specific nanostructure, the Re-PANI film shows a relatively small internal resistance and a high gravimetric capacitance. This high gravimetric capacitance and low internal resistance of the Re-PANI film are perhaps due to its high electrical conductivity, [40,98] which is one of the highest among those reported in the literature [16,23,40]. Notably, when the PANI component is incorporated with the RGO in film form, the Re-PARG film exhibits the highest gravimetric capacitance and the lowest internal resistance among all the samples, indicating the synergistic effect of PANI and RGO. This effect originates from the following two factors: (1) the combining effect of the EDL and faradaic capacitances, [92,93] in agreement with the two voltage stages of *ca.* 0.8–0.6 V and 0.6–0 V and (2) the extremely high electrical conductivity [40] from improved conducting networks of PANI chains by the RGO and the strong  $\pi$ – $\pi$  interactions between the RGO and the PANI chains. PANI, in its leucoemeraldine or pernigraniline form, is an insulator; accordingly, the supercapacitors possessing the PANI component suffer from large internal resistance, as it is close to the fully charged or discharged state [42,59,64,90]. However, the Re-PARG film possesses the RGO component, which could act as a good current collector, and the strong  $\pi$ – $\pi$  interactions between the RGO and the PANI chains in the Re-PARG film could provide a good conducting network even though PANI is close to the insulating form,

which facilitates the redox reaction of PANI and leads to the increase in the pseudo-capacitance [40,42,94]. Concurrently, the Re-PARG film with enhanced conducting networks decrease the internal resistance, leading to the improvement in effective energy storage by reducing the energy consumption caused by internal resistance [93].

The CV test was also performed on the Re-PARG film of two different sizes in 1M H<sub>2</sub>SO<sub>4</sub> at a scan rate of 5 mV s<sup>-1</sup> (Figure 30e). The size of one film (36 cm<sup>2</sup>, 3.5 inch) was 30 times larger than that of the other one (1.2 cm<sup>2</sup>, 0.8 inch). Both films were light-weight (2 and 60 mg) and thin (14.5 μm). Remarkably, even after the size of the film was increased 30 times, the larger sized film demonstrated an area capacitance of 0.655 F cm<sup>-2</sup> (393 F g<sup>-1</sup>), which is only 9 % smaller than that of the smaller sized film (0.718 F cm<sup>-2</sup>, 431 F g<sup>-1</sup>), suggesting a promising electrochemical property for large-scale supercapacitors.

The typical poor long-term stability of supercapacitors based on the CPs during cycling is one of the greatest obstacles in producing low-cost electrode materials for commercially available supercapacitors [46]. As shown in Figure 30f, the Re-PANI film shows a rapid initial drop on capacitance retention and maintains 60 % of initial gravimetric capacitance (from 256 to 153 F g<sup>-1</sup>) after 500 charging/discharging cycles at a current density of 0.45 A g<sup>-1</sup> because

PANI suffers from swelling and shrinkage during charging/discharging cycling [42,46,64,93]. The capacitance retention of the Re-PARG film also displays a rapid initial drop due to the large portion of PANI component (76 wt %) in the Re-PARG film. However, in the case of the Re-PARG film, it exhibits improved capacitance retention of 74 % (from 431 to 318 F g<sup>-1</sup>) after 500 charging/discharging cycles under the same conditions, due to suppression of the shrinking and swelling of the PANI chains by the mechanically strong RGO [94]. In addition to the enhanced mechanical property of the film by RGO, the enhanced cycling stability of the film is probably attributed to the increased electrical conductivity of the Re-PARG film. It is known that low electrical conductivity of a device causes the large resistance and joule heating while the device is working, which substantially diminishes the life of the organic device [23]. Therefore, for the Re-PARG film, increased electrical conductivity would lead to the improved cycling stability of the film by reducing the large resistance and joule heating of the electrode during the charging/discharging cycling. To obtain the film with less initial drops on capacitance retention and more enhanced capacitance retention, following method could be used in current PANI-graphene composite system. It has been reported that improvement in mechanical properties of graphene (e.g., from graphene oxide to reduced graphene oxide) could increase the retention rate of



PANI-graphene composite by enhancing the restraint of shrinkage and swelling of PANI chains during charging/discharging processes [69]. From this point of view, possible improvement can be realized by using mechanically stronger single-layer graphene sheet (e.g., fabricated by chemical vapor deposition or arc-discharge method) [70,99] or graphene nanoribbon [100] than RGO prepared by Hummers' method. The enhanced mechanical resilience by mechanically stronger graphene sheet or graphene nanoribbon might result in cycling performance improvement with the enhanced electrical conductivity and crystallinity due to the  $\pi$ - $\pi$  stacking between PANI structure and graphitic surface of single-graphene sheet or graphene nanoribbon. Using this method, the cyclability of the PANI-RGO system electrode can probably be increased even in long cycles. Finally, all of these results suggest the great potential of the PANI/RGO film to be used as an electrode material for high-performance scalable supercapacitors.

Figure 31a depicts the great flexibility of the Re-PARG film, which can endure bending, twisting, and even folding without any destruction. This high flexibility of the Re-PARG film is attributed to the inherent flexibility of the CPs [23,40,101,102]. Additionally, in order to test the supercapacitor performance of the Re-PARG film under bending conditions, the CV test was also performed on the films with two different bending angles of  $0^\circ$  and  $180^\circ$  at

a scan rate of  $5 \text{ mV s}^{-1}$ . As shown in Figure 31b, the Re-PARG films represent

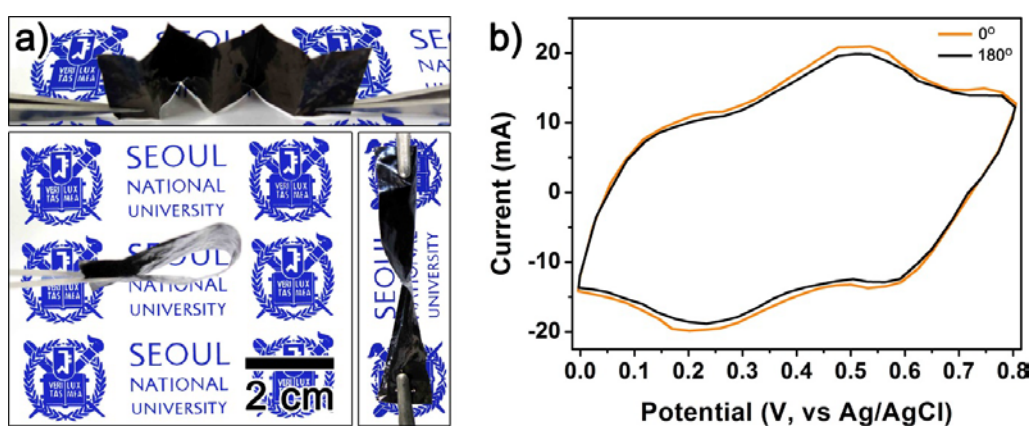


**Figure 31.** a) Digital photographs of flexible Re-PARG film. The top image exhibits the folding characteristics of the film. The bottom images illustrate the high flexibility (bending and twisting) of the film; b) CV curves of Re-PARG film electrodes with two different bending angles of  $0^\circ$  and  $180^\circ$  at a scan rate of  $5 \text{ mV s}^{-1}$ .

the non-substantial difference between the CV curves with bending angles of  $0^\circ$  and  $180^\circ$ , indicating the superior performance ability of the Re-PARG film as a flexible supercapacitor. Therefore, the Re-PARG film can potentially be applied in producing flexible electronic equipment such as bendable displays, intelligent clothes, and various flexible devices.

#### 4. CONCLUSIONS

1. Highly conductive PANI/SiO<sub>2</sub> nanocomposites with large surface area have been made using the SSDP method. The diameter of the nanocomposites were controlled from 18 nm to 130 nm by varying the size of the SiO<sub>2</sub> NPs. As the diameter of the PANI/SiO<sub>2</sub> nanocomposite decreased (from 130 to 18 nm), the electrical conductivity increased (from 16.4 to 25.6 S cm<sup>-1</sup>). When applied as electrode materials for supercapacitors, PANI/SiO<sub>2</sub> nanocomposite prepared by SSDP method exhibited improved specific capacitance (*ca.* 305 F g<sup>-1</sup>) and cycle-life performance (72 % after 500 cycles) compared to PANI/SiO<sub>2</sub> nanocomposite (*ca.* 112 F g<sup>-1</sup> and 60 % after 500 cycles) synthesized by conventional polymerization method. The high conductivity and large surface area facilitated the charge/discharge of PANI, and the increased crystalline structure of PANI prevented severe deterioration of the polymer structure. The highly conductive and crystalline PANI/SiO<sub>2</sub> nanocomposite prepared by SSDP can be used in various applications, such as batteries, sensors, actuators, corrosion protection, electro-optics, electro-chromic devices, and dye-sensitized solar cells.
2. PANI/MoS<sub>2</sub> nanocomposite has been prepared using SSDP and electrical and electrochemical properties of PANI/MoS<sub>2</sub> nanocomposite have been

revealed. Produced PANI/MoS<sub>2</sub> nanocomposite demonstrated remarkably high electrical conductivity of *ca.* 28.6 S cm<sup>-1</sup>. In the electrochemical tests, PANI/MoS<sub>2</sub> nanocomposite demonstrated high capacitance of *ca.* 400 F g<sup>-1</sup> and good cycling stability (84 % after 500 cycles). All these results suggest great potential of the PANI/MoS<sub>2</sub> nanocomposite as practical supercapacitor electrode.

3. Flexible PANI/RGO film was successfully fabricated through solution processing. The strong  $\pi$ - $\pi$  interactions of RGO with the quinoid rings of the PANI chains in the solution induced the more expanded conformation of the PANI chains, leading to the extremely high electrical conductivity of the film (*ca.* 906 S cm<sup>-1</sup>) (greater than the pristine PANI film :*ca.* 580 S cm<sup>-1</sup>) and RGO (*ca.* 45.6 S cm<sup>-1</sup>)). Additionally, the film demonstrated the high capacitance of *ca.* 431 F g<sup>-1</sup> and enhanced cycling stability (74 % after after 500 cycles) in comparison with pure PANI film (*ca.* 256 F g<sup>-1</sup> and 60 % after 500 cycles). The PANI/RGO film also demonstrated excellent performance ability as a scalable and flexible electrode material for high-performance supercapacitors with various film sizes and even under bending conditions. This approach will offer a valuable and promising tool for producing highly flexible, scalable, and high-performance supercapacitor electrodes.

In summary, three different PANI/organic • inorganic composites were prepared *via* SSDP method with considering five conditions for producing a high-performance supercapacitor to achieve supercapacitors with high capacitance and good electrochemical stability. First, PANI/SiO<sub>2</sub> nanocomposite was fabricated by SSDP method. Produced PANI/SiO<sub>2</sub> nanocomposite exhibited enhanced electrochemical performances (specific capacitance: *ca.* 305 F g<sup>-1</sup>, cycling stability: maintaining 72 % of initial gravimetric capacitance after 500 cycles) compared with PANI/SiO<sub>2</sub> nanocomposite prepared by conventional polymerization method and other previously reported PANI owing to high electrical conductivity (*ca.* 25.6 S cm<sup>-1</sup>), large specific surface area (*ca.* 170 m<sup>2</sup> g<sup>-1</sup>), and improved crystallinity. Second, PANI/MoS<sub>2</sub> nanocomposite, synthesized by SSDP method, showed improved specific capacitance (*ca.* 400 F g<sup>-1</sup>) in comparison with both PANI (*ca.* 232 F g<sup>-1</sup>) and MoS<sub>2</sub> nanosheet (*ca.* 3 F g<sup>-1</sup>) due to high electrical conductivity (*ca.* 28.6 S cm<sup>-1</sup>) and pseudo capacitive characteristics of PANI and MoS<sub>2</sub>. Additionally, PANI/MoS<sub>2</sub> nanosheet exhibited enhanced cycling stability (84 % after 500 cycles) compared with pristine PANI (62 % after 500 cycles) due to honeycomb-like structured PANI on MoS<sub>2</sub> nanosheet and incorporation of MoS<sub>2</sub> nanosheet possessing good mechanical properties. Lastly, flexible PANI/RGO film was fabricated through solution processing.

Produced PANI/RGO film exhibited extremely high electrical conductivity of *ca.*  $906 \text{ S cm}^{-1}$  due to improved crystallinity. In the electrochemical tests, PANI/RGO film exhibited enhanced capacitance (*ca.*  $431 \text{ F g}^{-1}$ ) and cycling stability (74 % after after 500 cycles) compare with pristine PANI film (specific capacitance: *ca.*  $256 \text{ F g}^{-1}$ , cycling stability: 60 % after 500 cycles). The PANI/RGO film also demonstrated excellent performance ability as a scalable and flexible electrode material. The strategies and specific synthetic methods described here can be useful tool for fabricating supercapacitor electrodes with high capacitance and good electrochemical stability.

## REFERENCES

- [1] P. Simon, Y. Gogotsi, *Nat. Mater.*, **2008**, 7, 845.
- [2] M. Huang, F. Li, F. Dong, Y. X. Zhang, L. L. Zhang, *J. Mater. Chem. A*, DOI: 10.1039/C5TA05523G.
- [3] M. Kim, C. Lee, J. Jang, *Adv. Funct. Mater.*, **2014**, 24, 2489.
- [4] S. Cho, M. Kim, J. Jang, *ACS Appl. Mater. Interfaces*, **2015**, 7, 10213.
- [5] J. Jun, J. S. Lee, D. H. Shin, S. G. Kim, J. Jang, *Nanoscale*, **2015**, 7, 16026.
- [6] J. S. Lee, D. H. Shin, J. Jang, *Energy Environ. Sci.*, **2015**, 8, 3030.
- [7] E. Song, J.-W. Choi, *Nanomaterials*, **2013**, 3, 498.
- [8] J. Huang, R. B. Kaner, *Angew. Chem.*, **2004**, 116, 5941.
- [9] J. Jang, J. Ha, J. Cho, *Adv. Mater.*, **2007**, 19, 1772.
- [10] S. Cho, O. S. Kwon, S. A. You, J. Jang, *J. Mater. Chem. A*, **2013**, 1, 5679.
- [11] A. G. Macdiarmid, *Angew. Chem. Int. Ed.*, **2001**, 40, 2581.
- [12] K. Matyjaszewski, Oxidative polymerization. In *Encyclopedia of polymer science and technology*. H. Higashimura, S. Kobayashi, 4th ed., John Wiley & Sons, Inc.: New York, 2004, pp 740–764.
- [13] J. Jang, *Adv. Polym. Sci.*, **2006**, 199, 189.
- [14] H. Bai, G. Shi, *Sensors*, **2007**, 7, 267.



- [15] S. Bhadra, D. Khastgir, N. K. Singha, J. H. Lee, *Prog. Polym. Sci.*, **2009**, *34*, 783.
- [16] S. Lee, D. Lee, K. Lee, C. Lee, *Adv. Funct. Mater.*, **2005**, *15*, 1495.
- [17] K. Lee, S. Cho, S. H. Park, A. J. Heeger, C.-W. Lee, S.-H. Lee, *Nature*, **2006**, *441*, 65.
- [18] P. D. McNaughter, J. C. Bear, D. C. Steytler, A. G. Mayes, T. Nann, *Angew. Chem. Int. Ed.*, **2011**, *50*, 10384.
- [19] E. E. Lees, T. L. Nguyen, A. H. A. Clayton, P. Mulvaney, *ACS Nano*, **2009**, *3*, 1121.
- [20] J. Jang, J. Ha, B. Lim, *Chem. Commun.*, **2006**, 1622.
- [21] H. Tadokoro, S. Seki, I. Nitta, *Bull. Chem. Soc. Jpn.*, **1995**, *28*, 559.
- [22] E. Dmitrieva, L. Dunsch, *J. Phys. Chem. B*, **2011**, *115*, 6401.
- [23] B. H. Lee, S. H. Park, H. Back, K. Lee, *Adv. Funct. Mater.*, **2011**, *21*, 487.
- [24] K. Lee, in *Encyclopedia of Nanoscience and Nanotechnology* (Ed: Nalwa, H. S.), American Scientific Publications, San Diego, CA 2003.
- [25] J. Tsukamoto, *Adv. Phys.*, **1992**, *41*, 509.
- [26] M. Yamaura, K. Sato, T. Hagiwara, K. Iwata, *Synth. Met.*, **1992**, *48*, 337.
- [27] Y. Nogami, J. P. Pouget, T. Ishiguro, *Synth. Met.*, **1994**, *62*, 257.

- [28] J. Joo, Z. Oblakowski, G. Du, J. P. Pouget, E. J. Oh, J. M. Wiesinger, Y. Min, A. G. MacDiarmid, A. J. Epstein, *Phys. Rev. B*, **1994**, 49, 2977.
- [29] J. P. Pouget, Z. Oblakowski, Y. Nogami, P. A. Albouy, M. Laridjani, E. J. Oh, Y. Min, A. G. MacDiarmid, J. Tsukamoto, T. Ishiguro, A. J. Epstein, *Synth. Met.*, **1994**, 65, 131.
- [30] Z. H. Wang, E. M. Scherr, A. G. MacDiarmid, A. J. Epstein, *Phys. Rev. B*, **1992**, 45, 4190.
- [31] R. Menon, C. O. Yoon, D. Moses, A. J. Heeger, Y. Cao, *Phys. Rev. B*, **1993**, 48, 17685.
- [32] R. Menon, C. O. Yoon, D. Moses, A. J. Heeger, in *Handbook of Conducting Polymers*, 2nd edition (Ed: T. A. Skotheim, R. L. Elsenbaumer, J. R. Reynolds, Dekker, New York 1998).
- [33] C. O. Yoon, R. Menon, D. Moses, A. J. Heeger, *Phys. Rev. B*, **1994**, 49, 10851.
- [34] Y. Chang, K. Lee, R. Kiebooms, A. Aleshin, A. J. Heeger, *Synth. Met.*, **1999**, 105, 203.
- [35] A. Raghunathan, G. Rangarajan, D. C. Trivedi, *Synth. Met.*, **1996**, 81, 39.
- [36] C. Lee, Y. H. Seo, S. H. Lee, *Macromolecules*, **2004**, 37, 4070.
- [37] R. Gangopadhyay, A. De, *Chem. Mater.*, **2000**, 12, 608.

- [38] J. Li, H. Xie, Y. Li, J. Liu, Z. Li, *J. Power Source*, **2011**, 196, 10775.
- [39] Y. Li, X. Zhao, Q. Xu, Q. Zhang, D. Chen, *Langmuir*, **2011**, 27, 6458.
- [40] J. Yan, T. Wei, B. Shao, Z. Fan, W. Qian, M. Zhang, F. Wei, *Carbon*, **2010**, 48, 487.
- [41] S. R. Sivakkumar, W. J. Kim, J. A. Choi, D. R. MacFarlane, M. Forsyth, D. W. Kim, *J. Power Source*, **2007**, 171, 1062.
- [42] Q. Wu, Y. Xu, Z. Yao, A. Liu, G. Shi, *ACS Nano*, **2010**, 4, 1963.
- [43] K. S. Ryu, K. M. Kim, N. G. Park, Y. J. Park, S. H. Chang, *J. Power Source*, **2002**, 103, 305.
- [44] L. Li, E. Liu, J. Li, Y. Yang, H. Shen, Z. Huang, X. Xiang, W. Li, *J. Power Source*, **2010**, 195, 1561.
- [45] J. Li, J. Fang, M. Cui, H. Lu, Z. A. Zhang, Y. A. Lai, *J. Cent. South Univ. Technol*, **2011**, 18, 78.
- [46] J. Xu, K. Wang, S. Z. Zu, B. H. Han, Z. Wei, *ACS Nano*, **2010**, 4, 5019.
- [47] Y. Zhao, H. Bai, Y. Hu, Y. Li, L. Qu, S. Zhang, G. Shi, *J. Mater. Chem.*, **2011**, 21, 13978.
- [48] L. Z. Fan, Y. S. Hu, J. Maier, P. Adelhelm, B. Smarsly, M. Antonietti, *Adv. Funct. Mater.*, **2007**, 17, 3083.
- [49] L. Li, H. Song, Q. Zhang, J. Yao, X. Chen, *J. Power Sources*, **2009**, 187, 268.

- [50] Q. Liu, M. H. Nayfeh, S. T. Yau, *J. Power Sources*, **2010**, 195, 3956.
- [51] Y. Li, X. Zhao, Q. Xu, Q. Zhang, D. Chen, *Langmuir*, **2011**, 27, 6458.
- [52] G. Y. Chen, Y. H. Cheng, Y. J. Chou, M. S. Su, C. M. Chen, K. H. Wei, *Chem. Commun.*, **2011**, 47, 5064.
- [53] C. Lee, H. Yan, L. E. Brus, T. F. Heinz, J. Hone, S. Ryu, *ACS Nano*, **2010**, 4, 2695.
- [54] H. Li, Q. Zhang, C. C. R. Yap, B. K. Tay, T. H. T. Edwin, A. Olivier, D. Baillargeat, *Adv. Funct. Mater.*, **2012**, 22, 1385.
- [55] P. Sambyal, A. P. Singh, M. Verma, M. Farukh, B. P. Singh, S. K. Dhawan, *RSC Adv.*, **2014**, 4, 12614.
- [56] R. Islam, R. Chan-Yu-King, J.-F. Brun, C. Gors, A. Addad, M. Depriester, A. Hadj-Sahraoui, F. Roussel, *Nanotechnology*, **2014**, 25, 475705.
- [57] Z. Tai, X. Yan, Q. Xue, *J. Electrochem. Soc.*, **2012**, 159, A1702.
- [58] J. M. Soon, K. P. Loh, *Electrochem. Solid State Lett.*, **2007**, 10, A250.
- [59] N. A. Kumar, H.-J. Choi, Y. R. Shin, D. W. Chang, L. Dai, J.-B. Baek, *ACS Nano*, **2012**, 6, 1715.
- [60] G. Xiong, C. Meng, R. G. Reifengerger, P. P. Irazoqui, T. S. Fisher, *Energy Technol.*, **2014**, 2, 897.

- [61] L. Cao, S. Yang, W. Gao, Z. Liu, Y. Gong, L. Ma, G. Shi, S. Lei, Y. Zhang, S. Zhang, R. Vajtai, P. M. Ajayan, *Small*, **2013**, 9, 2905.
- [62] Z. Zhou, X.-F. Wu, *J. Power Sources*, **2013**, 222, 410.
- [63] A. Castellanos-Gomez, R. van Leeuwen, M. Buscema, H. S. J. van der Zant, G. A. Steele, W. J. Venstra, *Adv. Mater.*, **2013**, 25, 6719.
- [64] K. Zhang, L. L. Zhang, X. S. Zhao, J. Wu, *Chem. Mater.*, **2010**, 22, 1392.
- [65] M. Ginic-Markovic, J. G. Matison, R. Cervini, G. P. Simon, P. M. Fredericks, *Chem. Mater.*, **2006**, 18, 6258.
- [66] A. G. MacDiarmid, A. J. Epstein, *Synth. Met.*, **1994**, 65, 103.
- [67] U. J. Lee, S.-H. Lee, J. J. Yoon, S. J. Oh, S. H. Lee, J. K. Lee, *Sol. Energy Mater. Sol. Cells*, **2013**, 108, 50.
- [68] J. Zhang, J. Jiang, H. Li, X. S. Zhao, *Energy Environ. Sci.*, **2011**, 4, 4009.
- [69] H. Wang, Q. Hao, X. Yang, L. Lu, X. Wang, *Nanoscale*, **2010**, 2, 2164.
- [70] Z.-S. Wu, W. Ren, L. Gao, J. Zhao, Z. Chen, B. Liu, D. Tang, B. Yu, C. Jiang, H.-M. Cheng, *ACS Nano*, **2009**, 3, 411.
- [71] M. -I. Boyer, S. Quillard, E. Rebourt, G. Louarn, J. P. Buisson, A. Monkman, S. Lefrant, *J. Phys. Chem. B*, **1998**, 102, 7382.
- [72] M. Jain, S. Annapoorni, *Synth. Met.*, **2010**, 160, 1727.

- [73] J. E. Pereira da Silva, D. L. A. de Faria, S. I. Córdoba de Torresi, M. L. A. Temperini, *Macromolecules*, **2000**, *33*, 3077.
- [74] G. Louarn, M. Lapkowski, S. Quillard, A. Pron, J. P. Buisson, S. Lefrant, *J. Phys. Chem.*, **1996**, *100*, 6998.
- [75] G. Niaura, R. Mažeikienė, A. Malinauskas, *Synth. Met.*, **2004**, *145*, 105.
- [76] S. Bourdo, Z. Li, A. S. Biris, F. Watanabe, T. Viswanathan, I. Pavel, *Adv. Funct. Mater.*, **2008**, *18*, 432.
- [77] R. Mažeikienė, V. Tomkutė, Z. Kuodis, G. Niaura, A. Malinauskas, *Vib. Spectrosc.*, **2007**, *44*, 201.
- [78] S. Quillard, G. Louarn, S. Lefrant, A. Macdiarmid, *Phys. Rev. B*, **1994**, *50*, 12496.
- [79] A. Ray, G. E. Asturias, D. L. Kershner, A. F. Richter, A. G. MacDiarmid, A. J. Epstein, *Synth. Met.*, **1989**, *29*, 141.
- [80] K. L. Tan, E. T. Kang, K. G. Neoh, *Polym. Adv. Technol.*, **1994**, *5*, 171.
- [81] Z. Ping, *J. Chem. Soc., Faraday Trans.*, **1996**, *92*, 3063.
- [82] M. C. Bernard, A. Hugot-Le Goff, *Electrochim. Acta*, **2006**, *52*, 595.
- [83] S. Bhadra, N. K. Singha, D. Khastgir, *Polym. Int.*, **2007**, *56*, 919.
- [84] L. Dauginet-De Pra, S. Demoustier-Champagne, *Thin Solid Films*, **2005**, *479*, 321.
- [85] E. T. Kang, K. G. Neoh, K. L. Tan, *Prog. Polym. Sci.*, **1998**, *23*, 277.

- [86] A. Belmokhtar, A. Benyoucef, A. Zehhaf, A. Yahiaoui, C. Quijada, E. Morallon, *Synth. Met.*, **2012**, *162*, 1864.
- [87] A. Meneguzzi, M. C. Pham, J.-C. Lacroix, B. Piro, A. Adenier, C. A. Ferreira, P.-C. Lacaze, *J. Electrochem. Soc.*, **2001**, *148*, B121.
- [88] J. P. Pouget, M. E. Jozefowicz, A. J. Epstein, X. Tang, A. G. MacDiarmid, *Macromolecules*, **1991**, *24*, 779.
- [89] Z. Luo, X. Ma, D. Yang, L. Yuwen, X. Zhu, L. Weng, L. Wang, *Carbon*, **2013**, *57*, 470.
- [90] H.-W. Park, T. Kim, J. Huh, M. Kang, J. E. Lee, H. Yoon, *ACS Nano*, **2012**, *6*, 7624.
- [91] X. Yan, J. Chen, J. Yang, Q. Xue, P. Miele, *ACS Appl. Mater. Interfaces*, **2010**, *2*, 2521.
- [92] Y. Zhao, H. Bai, Y. Hu, Y. Li, L. Qu, S. Zhang, G. Shi, *J. Mater. Chem.*, **2011**, *21*, 13978.
- [93] J. Yan, T. Wei, Z. Fan, W. Qian, M. Zhang, X. Shen, F. Wei, *J. Power Sources*, **2010**, *195*, 3041.
- [94] X. Lu, H. Dou, S. Yang, L. Hao, L. Zhang, L. Shen, F. Zhang, X. Zhang, *Electrochim. Acta*, **2011**, *56*, 9224.
- [95] M. D. Stoller, S. Park, Y. Zhu, J. An, R. S. Ruoff, *Nano Lett.*, **2008**, *8*, 3498.

- [96] H. Mi, X. Zhang, X. Ye, S. Yang, *J. Power Sources*, **2008**, 176, 403.
- [97] B. C. Kim, J. S. Kwon, J. M. Ko, J. H. Park, C. O. Too, G. G. Wallace, *Synth. Met.*, **2010**, 160, 94.
- [98] X.-M. Feng, R.-M. Li, Y.-W. Ma, R.-F. Chen, N.-E. Shi, Q.-L. Fan, W. Huang, *Adv. Funct. Mater.*, **2011**, 21, 2989.
- [99] H. J. Park, J. Meyer, S. Roth, V. Skákalová, *Carbon*, **2010**, 48, 1088.
- [100] L. Li, A. -R. O. Raji, H. Fei, Y. Yang, E. L. G. Samuel, J. M. Tour, *ACS Appl. Mater. Interfaces*, **2013**, 5, 6622.
- [101] J. Cho, K.-H. Shin, J. Jang, *Synth. Met.*, **2010**, 160, 1119.
- [102] H. Yoon, M. Chang, J. Jang, *Adv. Funct. Mater.*, **2007**, 17, 431.





## 저작자표시-비영리-변경금지 2.0 대한민국

이용자는 아래의 조건을 따르는 경우에 한하여 자유롭게

- 이 저작물을 복제, 배포, 전송, 전시, 공연 및 방송할 수 있습니다.

다음과 같은 조건을 따라야 합니다:



저작자표시. 귀하는 원저작자를 표시하여야 합니다.



비영리. 귀하는 이 저작물을 영리 목적으로 이용할 수 없습니다.



변경금지. 귀하는 이 저작물을 개작, 변형 또는 가공할 수 없습니다.

- 귀하는, 이 저작물의 재이용이나 배포의 경우, 이 저작물에 적용된 이용허락조건을 명확하게 나타내어야 합니다.
- 저작권자로부터 별도의 허가를 받으면 이러한 조건들은 적용되지 않습니다.

저작권법에 따른 이용자의 권리는 위의 내용에 의하여 영향을 받지 않습니다.

이것은 [이용허락규약\(Legal Code\)](#)을 이해하기 쉽게 요약한 것입니다.

[Disclaimer](#)

工學博士學位論文

**Fabrication of Polyaniline/Organic • Inorganic Composites  
for Supercapacitor Electrodes**

폴리아닐린/유기물 • 무기물 복합체 제조와 이의 슈퍼커패시터  
전극으로의 응용

2016年 2月

서울대학교 大學院

化學生物工學部

金 玟 奎

**Fabrication of Polyaniline/Organic • Inorganic Composites  
for Supercapacitor Electrodes**

폴리아닐린/유기물 • 무기물 복합체 제조와 이의 슈퍼커패시터  
전극으로의 응용

指導教授: 張 正 植

이 論文을 工學博士 學位論文으로 提出함

2015年 11月

서울대학교 大學院

化學生物工學部

金 玟 奎

金玟奎의 工學博士 學位論文을 認准함

2015年 11月

委 員 長 \_\_\_\_\_ (인)

副委員長 \_\_\_\_\_ (인)

委 員 \_\_\_\_\_ (인)

委 員 \_\_\_\_\_ (인)

委 員 \_\_\_\_\_ (인)

**Fabrication of Polyaniline/Organic • Inorganic Composites  
for Supercapacitor Electrodes**

by

Minkyu Kim

Submitted to the Graduate School of Seoul National University

in Partial Fulfillment of the Requirements

for the Degree of Doctor of Philosophy

February, 2016

Thesis Adviser: Jyongsik Jang

## ABSTRACT

A supercapacitor has widely been utilized in diverse vehicles needing rapid energy delivery because of its high power density: within automobile, trams, light-rails, and cranes. As smaller forms, they have also been utilized as memory backup for static random-access memory. Materials used for supercapacitor electrode possess their pros and cons. For example, carbon materials show a good cycling stability, but specific capacitance is relatively low. In the case of conducting polymers (CPs), in contrast to carbon materials, they possess high specific capacitance, but the cycling stability is relatively poor due to their poor mechanical strength. Thus, large efforts have been made to fabricate supercapacitor with high capacitance and good cycling stability.

In this dissertation, three different polyaniline (PANI)/organic • inorganic composites were prepared using self-stabilized dispersion polymerization (SSDP) method to achieve supercapacitors with high capacitance and good electrochemical stability. First, PANI/silicon dioxide ( $\text{SiO}_2$ ) nanocomposite was fabricated by SSDP method. Produced PANI/ $\text{SiO}_2$  nanocomposite exhibited improved electrochemical performances (specific capacitance: *ca.* 305 F g<sup>-1</sup>, cycling stability: maintaining 72 % of initial gravimetric capacitance

after 500 cycles) compared with PANI/SiO<sub>2</sub> nanocomposite synthesized by conventional polymerization method and other previously reported PANI nanomaterials owing to high electrical conductivity (*ca.* 25.6 S cm<sup>-1</sup>), large specific surface area (*ca.* 170 m<sup>2</sup> g<sup>-1</sup>), and improved crystallinity. Second, PANI/ molybdenum disulfide (MoS<sub>2</sub>) nanocomposite, synthesized by SSDP method, showed enhanced specific capacitance (*ca.* 400 F g<sup>-1</sup>) in comparison with both PANI (*ca.* 232 F g<sup>-1</sup>) and MoS<sub>2</sub> nanosheet (*ca.* 3 F g<sup>-1</sup>) due to high electrical conductivity (*ca.* 28.6 S cm<sup>-1</sup>) and pseudo capacitive characteristics of PANI and MoS<sub>2</sub>. Additionally, PANI/MoS<sub>2</sub> nanosheet exhibited good cycling stability (84 % after 500 cycles) due to honeycomb-like structured PANI on MoS<sub>2</sub> nanosheet and incorporation of MoS<sub>2</sub> nanosheet possessing good mechanical properties. Lastly, PANI/reduced graphene oxide (RGO) film was fabricated through solution processing for highly scalable and flexible supercapacitor electrodes. Produced PANI/RGO film exhibited extremely high electrical conductivity of *ca.* 906 S cm<sup>-1</sup> due to improved crystallinity. In the electrochemical tests, PANI/RGO film exhibited enhanced capacitance (*ca.* 431 F g<sup>-1</sup>) and cycling stability (74 % after after 500 cycles) in comparison with

pure PANI film (specific capacitance: *ca.* 256 F g<sup>-1</sup>, cycling stability: 60 % after 500 cycles). The PANI/RGO film also demonstrated excellent performance ability as a scalable and flexible electrode material. The strategies and specific synthetic methods described here can be useful tool for fabricating supercapacitor electrodes with high capacitance and good electrochemical stability.

**KEYWORDS:** Polyaniline; Silicon dioxide; Molybdenum disulfide; Graphene; Composite; Self-stabilized dispersion polymerization; Supercapacitors

**STUDENT NUMBER:** 2011–21015

## **List of Abbreviations**

Ag : silver

AgCl : silver chloride

APS : ammonium persulfate

Ar : argon

BET : Brunauer–Emmett–Teller

C<sub>area</sub> : area capacitance

CHCl<sub>3</sub> : chloroform

C<sub>m</sub> : gravimetric capacitance

CP : conducting polymer

CP-MAS : cross-polarization and magic-angle spinning

CSA : (±)-10-camphorsulfonic acid

Cu : copper

CV : cyclic voltammetry

De- : de-doped

EB : emeraldine base

EDL : electrical double layer



EDX : energy dispersive x-ray spectroscopy

ES : emeraldine salt

FE- : Field-Emission

FT-IR : Fourier-transform infrared

GO : graphite oxide

$\text{H}^+$  : proton

$\text{H}_2\text{O}$  : water

$\text{H}_2\text{O}_2$  : hydrogen peroxide

$\text{H}_2\text{SO}_4$  : sulfuric acid

$\text{HCl}$  : hydrochloric acid

$\text{K}_2\text{S}_2\text{O}_8$  : potassium persulfate

$\text{KMnO}_4$  : potassium permanganate

Mo : molybdenum

$\text{MoS}_2$  : molybdenum disulfide

$\text{NaNO}_3$  : sodium nitrate

Ni : nickel

NMP : N-methyl-2-pyrrolidone

NMR : nuclear magnetic resonance

NP : nanoparticle

P<sub>2</sub>O<sub>5</sub> : phosphorus pentoxide

PANI : polyaniline

PARG : polyaniline/reduced graphene oxide

Pt : platinum

PTFE : poly(tetrafluoroethylene)

R : internal resistance

Re- : re-doped

RGO : reduced graphene oxide

S : sulphur

SEM : scanning electron microscope

SiO<sub>2</sub> : silicon dioxide

SP1 : polyaniline/silicon dioxide nanocomposite synthesized by self-stabilized  
dispersion polymerization

SP2 : polyaniline/silicon dioxide nanocomposite synthesized by conventional  
polymerization

SSDP : self-stabilized dispersion polymerization

TEM : transmission electron microscope

TGA : thermo-gravimetric analysis

XPS : X-ray photoelectron spectra

XRD : X-ray diffraction

## List of Figures

**Figure 1.** a) Schematic of a commercial spirally wound electric double layer (EDL) capacitor C); b) Assembled supercapacitors device; c) A small button cell supercapacitors; d) Specific power against specific energy, also called a Ragone plot, for various electrical energy storage devices. [1].

**Figure 2.** Schematic of two different charge storage mechanisms *via* a) EDL capacitor and b) pseudocapacitor. [2].

**Figure 3.** A typical cyclic voltammetry (CV) curve of polyaniline (PANI) in hydrochloric acid (HCl, pH 1) showing two sets of redox couples. The direction of potential scan is shown with the arrows. [7].

**Figure 4.** a) A schematic illustration of the synthesis of PANI nanofibers. 1) The oxidant (open circles) dopant solution is added into the aniline (solid circles) dopant solution and mixed. 2) A homogenous solution is obtained where all the aniline and oxidant molecules are evenly distributed, thus leading to fast polymerization across the entire solution. 3) PANI nanofibers are formed; b) A photopaper

image of the emblem of Seoul National University, printed with an inkjet printer using PANI–poly(4-styrenesulfonate) aqueous solution as ink; c) A scanning electron microscope (SEM) images of PANI nanomaterials synthesized at various initiator/aniline weight ratios. [8–10].

**Figure 5.** Diagram of the self-stabilized dispersion polymerization (SSDP) of PANI. [17].

**Figure 6.** Illustrations of the sequential steps for synthesis of PANI/SiO<sub>2</sub> nanocomposite.

**Figure 7.** Illustrations of the sequential steps for synthesis of PANI/SiO<sub>2</sub> nanocomposite.

**Figure 8.** FE-SEM images and TEM images (inset) of SP1 with the average size of a) 18 nm, b) 35 nm, c) 63 nm, and d) 130 nm. The scale bars of inset images represent 15 nm.

**Figure 9.** Size distribution histograms of SP1 with different diameters.

**Figure 10.** a) FT-IR spectra, b) XRD patterns, and c) Solid-state <sup>13</sup>C NMR spectra of the EB-state SP1 (red line) and SP2 (blue line).

**Figure 11.** Nitrogen adsorption/desorption isotherms of different sized SP1: 18 nm (red line), 35 nm (green line), 63 nm (black line), and 130 nm (purple line).

**Figure 12.** TEM image of the bulk PANI prepared by conventional polymerization method. Its diameter is *ca.* 1  $\mu\text{m}$ .

**Figure 13.** Cyclic voltammograms of SP1 (18, 35, 63, 130 nm) and SP2 (18 nm) at 30  $\text{mV s}^{-1}$  between 0 and 0.8 V in 1M  $\text{H}_2\text{SO}_4$  solution; b) Galvanostatic charge/discharge curve of SP1 (18 nm) at current density of 2.6  $\text{A g}^{-1}$  in 1M  $\text{H}_2\text{SO}_4$  solution; c) Specific capacitances of SP1 (18 nm) and SP2 (18 nm) as a function of cycle number at a current density of 2.6  $\text{A g}^{-1}$  in 1 M  $\text{H}_2\text{SO}_4$  solution; d) Specific capacitances of SP1 (18, 35, 63, 130 nm) and SP2 (18 nm) at 30  $\text{mV s}^{-1}$  between 0 and 0.8 V in 1M  $\text{H}_2\text{SO}_4$  solution.

**Figure 14.** SEM images of a)  $\text{MoS}_2$  nanosheets and b) PANI/ $\text{MoS}_2$  nanocomposite.

**Figure 15.** Raman spectra of a)  $\text{MoS}_2$  nanosheets, b) PANI, and c) PANI/ $\text{MoS}_2$  nanocomposite.

**Figure 16.** Electrical conductivity of the MoS<sub>2</sub> nanosheets, PANI, and PANI/MoS<sub>2</sub> nanocomposite.

**Figure 17.** SEM image of pure PANI synthesized by SSDP.

**Figure 18.** a) Cyclic voltammograms of MoS<sub>2</sub> nanosheet, PANI, and PANI/MoS<sub>2</sub> nanocomposite at a scan rate of 5 mV s<sup>-1</sup>, b) galvanostatic charge/discharge curves of MoS<sub>2</sub> nanosheet, PANI, and PANI/MoS<sub>2</sub> nanocomposite at a current density of 0.6 A g<sup>-1</sup>, c) gravimetric capacitances of MoS<sub>2</sub> nanosheet, PANI, and PANI/MoS<sub>2</sub> nanocomposite at a current density of 0.6 A g<sup>-1</sup>, and d) cycling stability of MoS<sub>2</sub> nanosheets, PANI, and PANI/MoS<sub>2</sub> nanocomposite at a current density of 0.6 A g<sup>-1</sup>.

**Figure 19.** CV curve of pristine MoS<sub>2</sub> nanosheet at a scan rate of 5 mV s<sup>-1</sup>.

**Figure 20.** Galvanostatic charge/discharge curve of pristine MoS<sub>2</sub> nanosheet at a current density of 0.6 A g<sup>-1</sup>.

**Figure 21.** Schematic illustration of the sequential steps for fabricating large-scale Re-PARG film.

**Figure 22.** Digital camera images of (left) electronic device (10.5 cm x 5.5 cm,

4.7 inch) and (right) Re-PARG film (16 cm x 13 cm, 8 inch) with a ruler below the electronic device and film for scale. The scale bars of ruler represent mm.

**Figure 23.** SEM images of a) Pristine RGO, b) PARG, c) Cross sectional view of Re-PANI film and d) Re-PARG film.

**Figure 24.** TEM images of a) Pristine RGO, b) PARG.

**Figure 25.** a) Raman spectra of GO, RGO, Re-PARG film, De-PARG, PARG and PANI (ES state), b) N 1s XPS spectra of PANI (ES state), PARG, De-PARG and Re-PARG film.

**Figure 26.** TGA curves of RGO, De-PARG 1-3 composites with different weight percentage of De-PANI, and De-PANI.

**Figure 27.** a) Electrical conductivity of Re-PANI film, Re-PARG 1-3 films, and RGO displayed as function of the weight percentage of PANI component; b) XRD patterns of graphite, GO, and RGO; c) XRD patterns of Re-PARG 1-3 films and Re-PANI film.

**Figure 28.** a) TGA curves of Re-PARG 2 powder, as-prepared Re-PARG 2 film and Re-PARG 2 film after storing for 150 days and b) XRD patterns



of as-prepared Re-PARG 2 film and Re-PARG 2 film after storing for 150 days.

**Figure 29.** Schematic representation of interaction between RGO and PANI chains leading to compact packing of the PANI chains with RGO and extensive three-dimensional delocalization of the charge.

**Figure 30.** a) CV curves of Re-PARG film, Re-PANI film and RGO electrodes at a scan rate of  $5 \text{ mV s}^{-1}$  between 0 and 0.8 V in 1M  $\text{H}_2\text{SO}_4$  solution; b) Galvanostatic charge/discharge curves of Re-PARG film, Re-PANI film and RGO electrodes at current density of  $0.45 \text{ A g}^{-1}$  in 1M  $\text{H}_2\text{SO}_4$  solution; c) Gravimetric capacitances of RGO, Re-PANI film and Re-PARG film electrodes at current density of  $0.45 \text{ A g}^{-1}$ ; d) Internal resistances of RGO, Re-PANI film and Re-PARG film electrodes estimated from the IR drop at a current density of  $0.45 \text{ A g}^{-1}$ ; e) Comparison of CV curves between different sized ( $1.2$  and  $36 \text{ cm}^2$ ) Re-PARG film electrodes at a scan rate of  $5 \text{ mV s}^{-1}$ ; f) Cyclic stability of Re-PARG film and Re-PANI film electrodes as a function of cycle number at a current density of  $0.45 \text{ A g}^{-1}$ .

**Figure 31.** a) Digital photographs of flexible Re-PARG film. The top image exhibits the folding characteristics of the film. The bottom images illustrate the high flexibility (bending and twisting) of the film; b) CV curves of Re-PARG film electrodes with two different bending angles of 0 ° and 180 ° at a scan rate of 5 mV s<sup>-1</sup>.

## List of Tables

**Table 1.** Weight ratio of the pristine  $\text{SiO}_2$  NPs and PANI/ $\text{SiO}_2$  nanocomposite measured by EDX.

**Table 2.** Electrical conductivities of the PANI/ $\text{SiO}_2$  nanocomposites.

## Table of Contents

<b>Abstract.....</b>	<b>i</b>
<b>List of Abbreviations.....</b>	<b>iv</b>
<b>List of Figures.....</b>	<b>viii</b>
<b>List of Tables.....</b>	<b>xv</b>
<b>Table of Contents.....</b>	<b>xvi</b>
<b>1. INTRODUCTION.....</b>	<b>1</b>
<b>1.1. Background.....</b>	<b>1</b>
1.1.1. Supercapacitors .....	1
1.1.2. PANI.....	5
1.1.2.1. Synthetic methods of PANI.....	5
<b>1.2. Objectives and Outlines.....</b>	<b>10</b>
1.2.1. Objectives.....	10
1.2.2. Outlines .....	10
<b>2. EXPERIMENTAL DETAILS .....</b>	<b>14</b>
<b>2.1. PANI/SiO<sub>2</sub> nanocomposite for supercapacitor electrodes .....</b>	<b>14</b>
2.1.1. Fabrication of PANI/SiO <sub>2</sub> nanocomposite .....	14
2.1.2. Supercapacitors based on PANI/SiO <sub>2</sub> nanocomposites .....	17
<b>2.2. PANI/MoS<sub>2</sub> nanocomposite for supercapacitor electrodes .....</b>	<b>19</b>
2.2.1. Fabrication of PANI/MoS <sub>2</sub> nanocomposite .....	19
2.2.2. Supercapacitor based on PANI/MoS <sub>2</sub> nanocomposite .....	20

<b>2.3. PANI/graphene film for flexible supercapacitor electrodes .....</b>	<b>22</b>
2.3.1. Fabrication of PANI/RGO film .....	22
2.3.2. Flexible supercapacitor based on PANI/RGO film .....	26
 <b>3. RESULTS AND DISCUSSION .....</b>	<b>29</b>
 <b>3.1. PANI/SiO<sub>2</sub> nanocomposite for supercapacitor electrodes .....</b>	<b>29</b>
3.1.1. Fabrication of PANI/SiO <sub>2</sub> nanocomposite .....	29
3.1.2. Supercapacitors based on PANI/SiO <sub>2</sub> nanocomposite .....	44
<b>3.2. PANI/MoS<sub>2</sub> nanocomposite for supercapacitor electrodes .....</b>	<b>50</b>
3.2.1. Fabrication of PANI/MoS <sub>2</sub> nanocomposite .....	50
3.2.2. Supercapacitor based on PANI/MoS <sub>2</sub> nanocomposite .....	57
<b>3.3. PANI/graphene film for flexible supercapacitor electrodes .....</b>	<b>65</b>
3.3.1. Fabrication of PANI/RGO film .....	65
3.3.2. Flexible supercapacitor based on PANI/RGO film .....	88
 <b>4. CONCLUSIONS .....</b>	<b>99</b>
 <b>REFERENCES .....</b>	<b>103</b>

# **1. INTRODUCTION**

## **1.1. Background**

### **1.1.1. Supercapacitors**

A supercapacitors have widely been utilized in diverse vehicles needing rapid energy delivery because of its high power density (Figure 1) [1]: within automobile, trams, light-rails, and cranes. As smaller forms, they have also been utilized as memory backup for static random-access memory. Supercapacitors can be classified into two types depending on their energy storage mechanisms: electric double layer (EDL) capacitor and pseudocapacitor (Figure 2) [1,2]. EDL capacitor stores electrical energy by electrostatically charging charge ions in electrical double layers generated on electrode surface. As electrode material for EDL capacitor, various carbon materials such as activated carbons and graphene have been employed. In case of pseudocapacitor, it stores electrical energy by charging the electron in the electrode through the fast reversible redox reaction. CPs (e.g., PANI, polypyrrole, and polythiophene), transition metal sulfides (e.g., MoS<sub>2</sub>, copper monosulfide, and nickel sulfide), transition metal oxides (e.g., manganese dioxide, cobalt oxide, and nickel oxide) belong to pseudocapacitor electrode material. Materials used for EDL capacitor and pseudocapacitor possess their pros and cons. For example, carbon materials show a good cycling stability

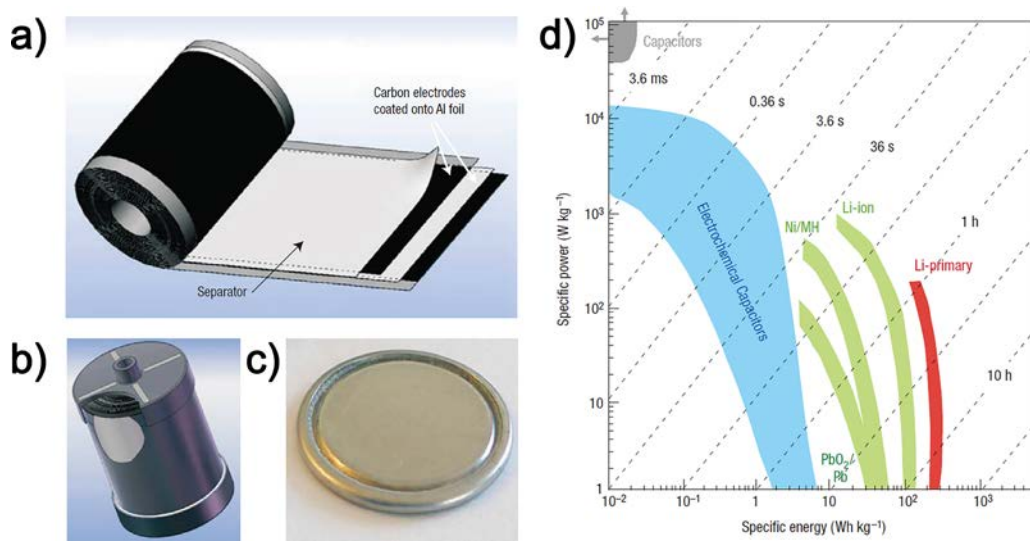


**Figure 1.** a) Schematic of a commercial spirally wound electric double layer (EDL) capacitor C); b) Assembled supercapacitors device; c) A small button cell supercapacitors; d) Specific power against specific energy, also called a Ragone plot, for various electrical energy storage devices. [1].

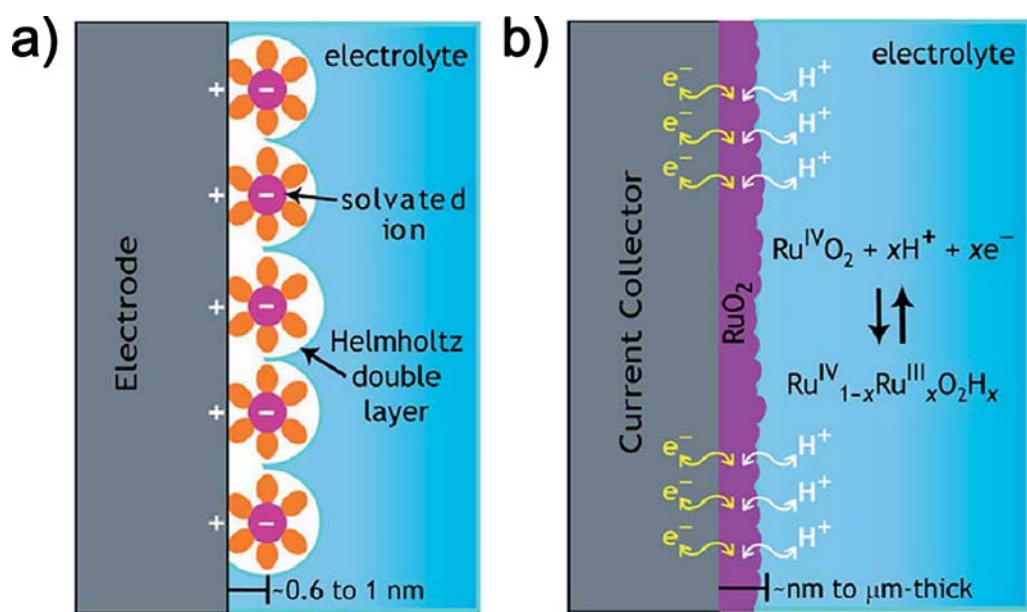


**Figure 2.** Schematic of two different charge storage mechanisms *via* a) EDL capacitor and b) pseudocapacitor. [2].



owing to its good mechanical properties, but specific capacitance is relatively low. In the cases of CPs, in contrast to carbon materials, they possess high specific capacitance, but cycling stability is relatively poor due to their poor mechanical strength [1,2]. Thus, large efforts have been made to fabricate supercapacitor with high capacitance and good cycling stability [1–6].

To achieve large capacitances from electrode materials, following three factors are needed to be considered: 1) energy storage-mechanisms. As described above, pseudo capacitive materials can obtain higher specific capacitances than EDL capacitive materials because larger charge ions can react with pseudo capacitive materials than EDL capacitive materials. 2) specific surface area. 3) electrical conductivity. Meanwhile, following factors must be considered to obtain good cycling stability from electrodes: 1) mechanical properties. 2) morphology. For CPs, they are repeatedly swelled and shrunk during cycling stability test, leading to cracking and breaking of polymer chains, gradual loss in electrical conductivity, and decrease in capacitance. In the case swelling/shrinkage volume is insufficient, the cracking and breaking of polymer chains accelerate, leading to rapid decrease in specific capacitance. Therefore, sufficient void volume must be needed to improve electrochemical stability of electrodes [1].

### 1.1.2. PANI

The PANI, a typical CP, has attracted great attention as supercapacitor electrode materials due to their fascinating properties such as pseudo capacitive characteristic, high electrical conductivity depending on synthetic method, controllable synthesis (e.g., morphology and specific surface area), mechanical flexibility, facile synthesis, and lower synthetic cost compared to other CPs (Figure 3 and 4) [1–3,7–10].

#### 1.1.2.1. Synthetic methods of PANI

Conventional PANI has been synthesized according to the MacDiarmid *et al.*, which includes the chemical oxidation of aniline in an acidic medium [11–15]. In the conventional method, the polymerization of aniline randomly occurs at the interfaces of growing PANI, swollen PANI, and aqueous medium, which making the obtained PANI to be vulnerable to the *ortho*-coupling and Michael reductive reactions. To prepare high-performance PANI without the undesirable reactions, an attempt that polymerizing aniline in a biphasic solvent system composed of aqueous and organic phases (distilled water (H<sub>2</sub>O)/chloroform (CHCl<sub>3</sub>) phase) has been made [16]. Lee *et al.* reported self-stabilized dispersion polymerization (SSDP) that the protonated anilinium ions, oligomers, and grown PANI chains serve as self-stabilizers: when the

temperature of the reaction solution dropped to  $-9\text{ }^{\circ}\text{C}$ , the solubility of the anilinium hydrochloride in the aqueous phase decreased and became distributed in both the aqueous (water) and organic (chloroform) phases. With both a hydrophilic part (amine group) and a hydrophobic part (phenyl ring), anilinium hydrochloride monomers acted as surfactant. After injection of water-soluble initiator, the growing PANI chains moved toward the interface between the aqueous and organic phases as result of insolubility in both aqueous and organic phases (Figure 5) [16]. This leads to *para*-directed polymerization and lower defects and higher conductivity of PANI compared to PANI prepared using conventional polymerization methods. In the case PANI synthesized by SSDP is secondary doped with  $(\pm)$ -10-camphorsulfonic acid (CSA) in *m*-Cresol/chloroform solution, and then, transformed to thin-film, it can exhibit high electrical conductivity as high as  $600\text{ S cm}^{-1}$  [16]. Although PANI synthesized by SSDP method possesses high electrical conductivity and pseudo capacitive characteristics, specific surface area is still low and the morphology is not suitable for swelling and shrinkage of PANI. Additionally, mechanical strength is still weak compared with EDL materials. Thus, to achieve high capacitance and good cycling stability, other factors such as specific surface area, morphology, and mechanical strength must be improved.

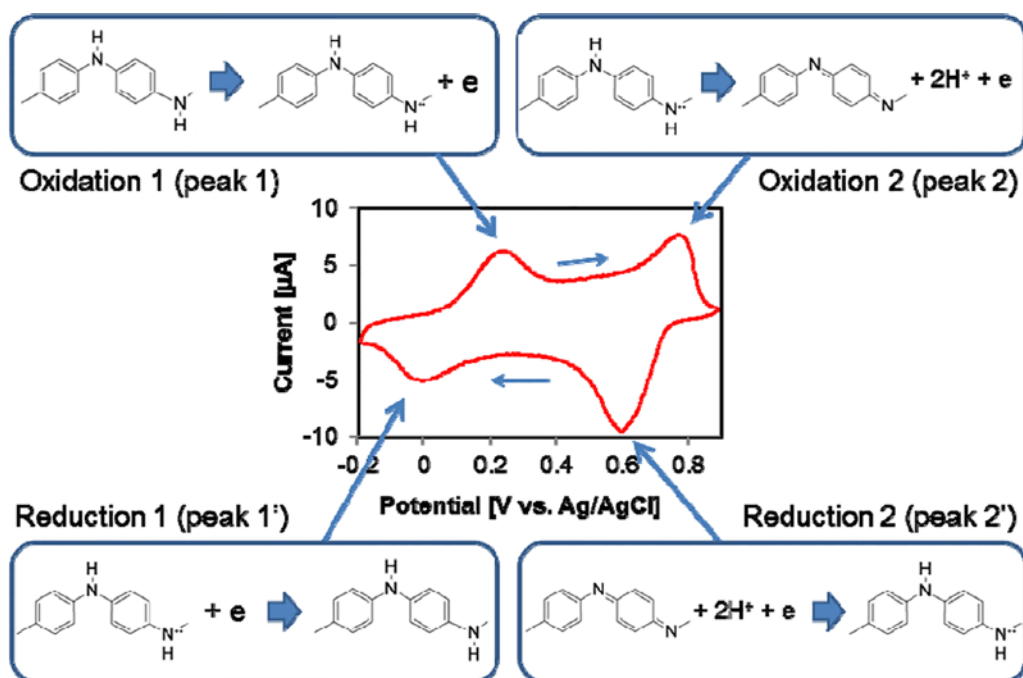


**Figure 3.** A typical cyclic voltammetry (CV) curve of polyaniline (PANI) in hydrochloric acid (HCl, pH 1) showing two sets of redox couples. The direction of potential scan is shown with the arrows. [7].

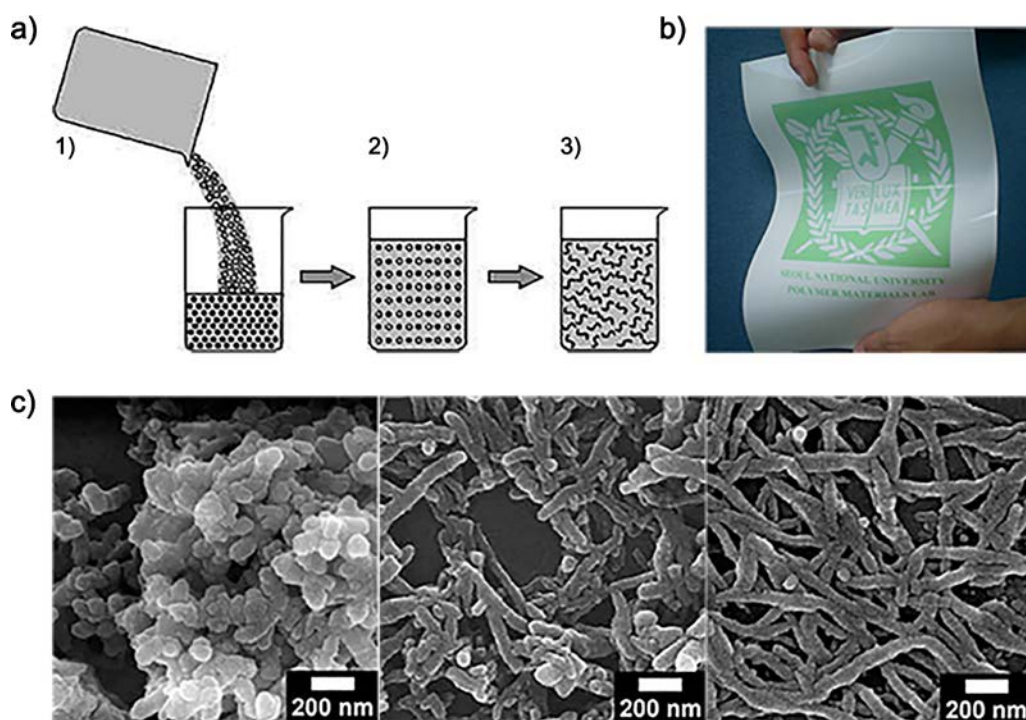


**Figure 4.** a) A schematic illustration of the synthesis of PANI nanofibers. 1) The oxidant (open circles) dopant solution is added into the aniline (solid circles) dopant solution and mixed. 2) A homogenous solution is obtained where all the aniline and oxidant molecules are evenly distributed, thus leading to fast polymerization across the entire solution. 3) PANI nanofibers are formed; b) A photopaper image of the emblem of Seoul National University, printed with an inkjet printer using PANI-poly(4-styrenesulfonate) aqueous solution as ink; c) A scanning electron microscope (SEM) images of PANI nanomaterials synthesized at various initiator/aniline weight ratios. [8–10].

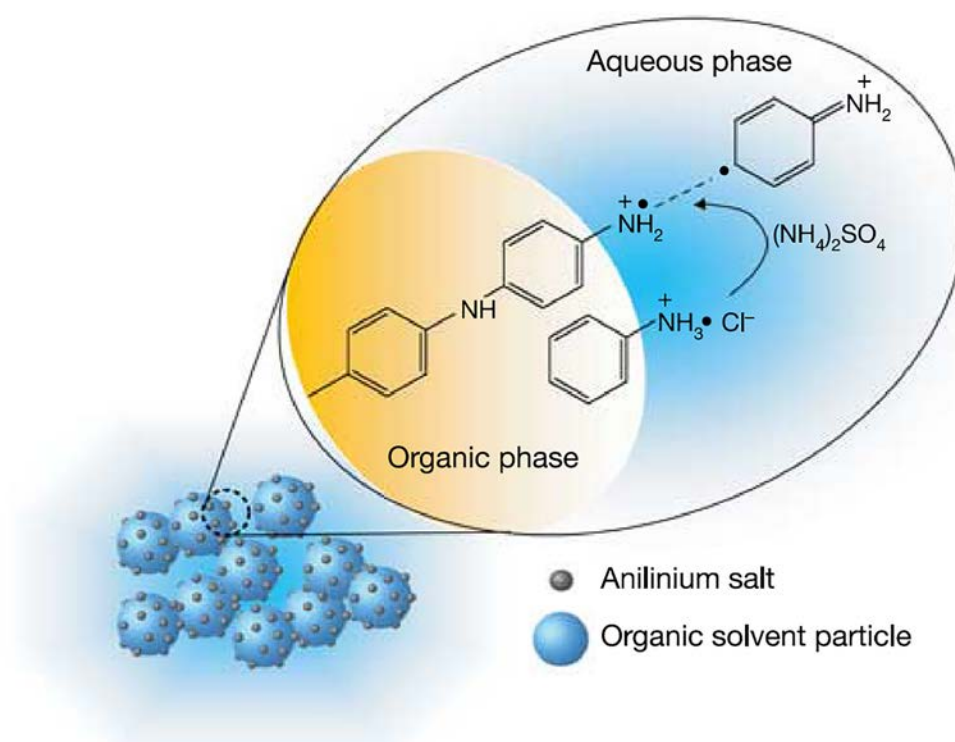


**Figure 5.** Diagram of the self-stabilized dispersion polymerization (SSDP) of PANI. [17].

## **1.2. Objectives and Outlines**

### **1.2.1. Objectives**

The aim of this dissertation is to fabricate supercapacitors with high capacitance and good electrochemical stability by synthesizing diverse PANI/organic inorganic • composite *via* SSDP method with considering five conditions for producing a high-performance supercapacitor. The morphological, spectroscopic, electrical, and electrochemical properties of the PANI/organic • inorganic composite are systematically and deeply studied.

### **1.2.2. Outlines**

This dissertation involves the following subtopics:

- I. PANI/SiO<sub>2</sub> nanocomposite for supercapacitor electrodes
  - 1. Fabrication of PANI/SiO<sub>2</sub> nanocomposite
  - 2. Supercapacitors based on PANI/SiO<sub>2</sub> nanocomposite
- II. PANI/MoS<sub>2</sub> nanocomposite for supercapacitor electrodes
  - 1. Fabrication of PANI/MoS<sub>2</sub> nanocomposite
  - 2. Supercapacitors based on PANI/MoS<sub>2</sub> nanocomposite
- III. PANI/graphene film for flexible supercapacitor electrodes
  - 1. Fabrication of PANI/RGO film
  - 2. Flexible supercapacitor based on PANI/RGO film

A detailed outline of the study is as follows:

1.1 Highly conductive PANI/SiO<sub>2</sub> nanocomposites were synthesized in various diameters (from 18 nm to 130 nm) using SSDP method. The polymerization was carried out in an aqueous/organic liquid system at -30 °C. In this system, biphasic solution plays a key role in directing *para*-direction oriented polymerization of the PANI on the surface of SiO<sub>2</sub> nanoparticles (NPs). Due to its *para*-direction polymerized structure, the synthesized PANI/SiO<sub>2</sub> nanocomposite exhibited enhanced electrical conductivity (ca. 25.6 S cm<sup>-1</sup>) compared with PANI/SiO<sub>2</sub> nanocomposite (ca. 1.4 S cm<sup>-1</sup>) prepared by homogeneous polymerization. The conductivities and Brunauer-Emmett-Teller (BET) surface areas were ca. 25.6 S cm<sup>-1</sup>/170 m<sup>2</sup> g<sup>-1</sup> (18 nm in diameter), ca. 22.5 S cm<sup>-1</sup>/111 m<sup>2</sup> g<sup>-1</sup> (35 nm in diameter), ca. 18.3 S cm<sup>-1</sup>/78 m<sup>2</sup> g<sup>-1</sup> (63 nm in diameter), and ca. 16.4 S cm<sup>-1</sup>/53 m<sup>2</sup> g<sup>-1</sup> (130 nm in diameter). In this series, increased *para*-coupling along the polymer backbone was elucidated using several characterization techniques, including Fourier-transform infrared (FT-IR), X-ray diffraction (XRD), and nuclear magnetic resonance (NMR) spectroscopy. Synthesized PANI/SiO<sub>2</sub> nanocomposite exhibited improved capacitance (ca. 305 F g<sup>-1</sup>) and enhanced cycle-life performance (maintains 72 % of initial gravimetric capacitance after 500 cycles)



compared to PANI/SiO<sub>2</sub> nanocomposite prepared by conventional polymerization method (ca. 112 F g<sup>-1</sup> and 60 % after 500 cycles).

2.1 PANI/MoS<sub>2</sub> nanocomposite was prepared using SSDP method.

Synthesized PANI/MoS<sub>2</sub> nanocomposite demonstrated remarkably high electrical conductivity of ca. 28.6 S cm<sup>-1</sup>. Additionally, PANI/MoS<sub>2</sub> nanocomposite showed high capacitance (ca. 400 F g<sup>-1</sup>) and good cycling stability (84 % after 500 cycles).

3.1 With developments in technology, tremendous effort has been devoted to produce flexible, scalable, and high-performance supercapacitor electrode material. This report presents a novel fabrication method of highly flexible and scalable electrode material for high-performance supercapacitors using solution-processed PANI/RGO hybrid film. Scanning electron microscope (SEM), transmission electron microscope (TEM), Raman, and X-ray photoelectron spectra (XPS) analyses showed that the PANI/RGO film was successfully synthesized. The percentages of the PANI component in the film were controlled (88, 76, and 60 %), and the maximum electrical conductivity (ca. 906 S cm<sup>-1</sup>) was observed at the PANI percentage of 76 %. Notably, electrical conductivity of the PANI/RGO film (ca. 906 S cm<sup>-1</sup>) was larger than both PANI (ca. 580 S cm<sup>-1</sup>) and RGO (ca. 46.5 S cm<sup>-1</sup>) components. XRD analysis demonstrated that the strong  $\pi$ - $\pi$  interaction

between the RGO and the PANI caused more compact packing of the PANI chains by inducing more fully expanded conformation of the PANI chains in the solution, leading to increase in the electrical conductivity and crystallinity of the film. The PANI/RGO film also displayed diverse advantages as a scalable and flexible electrode material (e.g., controllable size and great flexibility). During the electrochemical tests, the film exhibited high capacitance of ca. 431 F g<sup>-1</sup> and enhanced cycling stability (74 % after after 500 cycles) in comparison with pure PANI film synthesized by SSDP method (ca. 256 F g<sup>-1</sup> and 60 % after 500 cycles).

## 2. EXPERIMENTAL DETAILS

### 2.1. PANI/SiO<sub>2</sub> nanocomposite for supercapacitor electrodes

#### 2.1.1. Fabrication of PANI/SiO<sub>2</sub> nanocomposite

*Materials:* Aniline (C<sub>6</sub>H<sub>7</sub>N, ≥99.5%), ammonium persulfate (APS) ([NH<sub>4</sub>]<sub>2</sub>S<sub>2</sub>O<sub>8</sub>, 98%), hydrochloric acid (HCl, 37%), ammonia solution (28–30%), chloroform (CHCl<sub>3</sub>, ≥99.8%), and poly(tetrafluoroethylene) (PTFE; [C<sub>2</sub>F<sub>4</sub>]<sub>n</sub>, 60 wt % dispersion in H<sub>2</sub>O) were purchased from Aldrich Chemical Co. Deionized water was used as a chemical solvent for aniline. SiO<sub>2</sub> NPs (diameter: 12 nm and 22 nm) were purchased from Aldrich Chemical Co. The 50 and 100 nm SiO<sub>2</sub> NPs were synthesized using tetraethyl ortho silicate and ammonia solution.

*Fabrication of PANI/SiO<sub>2</sub> nanocomposite (SPI):* At first, the SiO<sub>2</sub> NPs (3.8 mmol) was added to deionized water (40 mL). An anilinium solution, aniline (2.1 mmol) and HCl (8.2 mmol) were added in deionized water (11 mL), was injected to the above-prepared solution under vigorous stirring condition (with magnetic stirring bar) and reaction proceeded for 1h at 0 °C. Then, the mixed solution was injected to the chloroform solution (80 mL) in Erlenmeyer flask with mechanical stirrer at −30 °C. Subsequently, APS solution (0.854 M, 2 mL) was injected to the mixture as initiator in a dropwise fashion. The reaction was performed until the color of the solution changed from opaque to

dark-green, which represents chemically doped PANI:emeraldine salt (ES). After the polymerization, PANI/SiO<sub>2</sub> nanocomposites were precipitated by centrifugal precipitation and washed with distilled water, ethanol, and acetone to remove residual agents. The size of PANI/SiO<sub>2</sub> nanocomposites were controlled by varying size of SiO<sub>2</sub> cores (from 12 to 100 nm). In each procedure, other reaction conditions are identical to those described above.

*Conventional polymerization for SP2 and bulk PANI:* SiO<sub>2</sub> NPs (3.8 mmol) was added to distilled water (40 mL). An anilinium solution, aniline (2.1 mmol) and HCl (8.2 mmol) were dissolved in deionized water (11 mL), was added as dropwise to the above-prepared solution, and stirred for 1 h under vigorous stirring. An APS solution (0.854 M, 2 mL) was added to the aniline/SiO<sub>2</sub> solution. The polymerization of aniline was carried out at room temperature (25 °C) for 12 h. After the polymerization, a dispersion solution of the PANI/SiO<sub>2</sub> nanocomposite was obtained by centrifugation and re-dispersion in distilled water, ethanol, and acetone. The size of the PANI/SiO<sub>2</sub> nanocomposites were controlled by varying the size of SiO<sub>2</sub> cores (from 12 to 100 nm). In each procedure, other reaction conditions are identical to those described above.

In the case of bulk PANI, aniline (0.01 M) was dissolved in HCl (0.9 M, 35 mL) solution at room temperature (25 °C) by magnetic stirring for 15 min. An

APS solution (0.5 M, 10 mL) was added to the solution which was magnetically stirred for 15 min and then stirring was kept for 6 h. The polymerization was stopped when the color of the solution changed to dark-green, which represents the ES states of chemically doped PANI. The prepared PANI was precipitated by centrifugal precipitation and washed with distilled water, ethanol, and acetone to remove residual agents. Finally the green colored PANI nanofibers were obtained.

*Instrumentation:* Photographs of TEM were obtained with a LIBRA 120 (Carl Zeiss, Germany). In the sample preparation, nanomaterials diluted in ethanol were cast onto a copper (Cu) grid. A JEOL 6700 (JEOL, Japan) was used to obtain Field-Emission SEM (FE-SEM) images and energy dispersive x-ray spectroscopy (EDX) graphs. The XRD was recorded on a New D8 Advance (Bruker, Germany). The FT-IR spectrum was recorded on a MB 100 spectroscope (Bomem, Canada) in the absorption mode. Avance II (Bruker, Germany) was used to obtain solid-state  $^{13}\text{C}$  NMR spectra. The measurement of the electrical conductivity was carried out with a KEITHLY 2400 by a four-probe method (KEITHLY, USA). Nitrogen adsorption/desorption isotherms were measured using Micromeritics ASAP 2000 at 77 K. The electrochemical measurements were performed with a Wonatech WBCS3000 potentiostat, which was measured in a conventional three-electrode beaker type cell in 1 M

sulfuric acid (H<sub>2</sub>SO<sub>4</sub>) solution as electrolyte at 25 °C.

### 2.1.2. Supercapacitors based on PANI/SiO<sub>2</sub> nanocomposites

*Electrochemical measurements:* The electrode for the supercapacitor was prepared as follows. The 2.2 mg of PANI/SiO<sub>2</sub> nanocomposite was mixed with polymeric binder (PTFE, 0.22 mg) and carbon black (0.22 mg). The mixture was coated on a stainless steel mesh (1 x 1 cm<sup>2</sup>) which is known to be stable in acidic condition. The coated mixture was rolled by a bar-coater to form a sheet type. Subsequently, the molded electrode was dried at 25 °C for 12 h before use. Cyclic voltammetry (CV) experiment was performed in the standard three-electrode system; silver (Ag)/silver chloride (AgCl) is used as the reference electrode, and a platinum (Pt) wire (6 cm) is used as the counter electrode in 1 M H<sub>2</sub>SO<sub>4</sub> solution as electrolyte at a sweep rate of 30 mV s<sup>-1</sup>. The galvanostatic charge/discharge tests at the current densities of 2.6 A g<sup>-1</sup> were performed within potential from 0 to 0.8 V in 1 M H<sub>2</sub>SO<sub>4</sub>. The specific capacitances of the electrodes were calculated according to the following equation from CV curves:

$$C_m = \frac{\int i dV}{(\nu \times m \times V)} \quad (1)$$

,where C<sub>m</sub> is the gravimetric capacitance based on the mass of electroactive materials (F g<sup>-1</sup>), i is the response current (mA), V is the potential (V),  $\nu$  is the

potential scan rate ( $\text{V s}^{-1}$ ), and  $m$  is the mass of the active electrode materials (mg).

## **2.2. PANI/MoS<sub>2</sub> nanocomposite for supercapacitor electrodes**

### **2.2.1. Fabrication of PANI/MoS<sub>2</sub> nanocomposite**

*Materials:* Aniline (C<sub>6</sub>H<sub>7</sub>N, ≥99.5%), ammonium persulfate ([NH<sub>4</sub>]<sub>2</sub>S<sub>2</sub>O<sub>8</sub>, 98%), molybdenum disulfide (MoS<sub>2</sub>, powder, < 2 μm, 99 %), and poly(tetrafluoroethylene) (PTFE; [C<sub>2</sub>F<sub>4</sub>]<sub>n</sub>, 60 wt % dispersion in H<sub>2</sub>O) were purchased from Sigma-Aldrich Chemical Co. Hydrochloric acid (HCl, 35.0-37.0 wt. %), chloroform (CHCl<sub>3</sub>, 99.8 %), and N-methyl-2-pyrrolidone (NMP, 99.5 %) were purchased from the Samchun Chemical Co. Mortar and pestle were acquired from Samwha ceramic.

*Preparation of MoS<sub>2</sub> nanosheets:* Exfoliation of MoS<sub>2</sub> was conducted by grinding 0.8 g of MoS<sub>2</sub> powder with 0.4 mL of NMP for 30 min in a mortar. The solvents were removed in a vacuum oven from gel-like mixtures. The powders were dispersed in 20 mL of ethanol/ deionized water (45 vol % of ethanol) and sonicated for 2 hr. Unexfoliated MoS<sub>2</sub> flakes were removed by centrifugation for several times and the supernatant was collected.

*Preparation of PANI/MoS<sub>2</sub> nanocomposite:* In the first step, aniline (0.2g) and HCl (35.0-37.0 wt. %, 1g) were added to deionized water (6 g) and then stirred for 10 min. Next, as-synthesized MoS<sub>2</sub> nanosheet (0.01 g) is added to above solution and then sonicated for 2hr. Next, chloroform (12 mL) was injected to mixture and then stirred for 1 min. Subsequently, the mixture was



sonicated for 1h. After sonication, the mixture was stirred under temperature of -43 °C at 400 rpm. When the temperature of solution dropped to -9 °C, initiator solution (H<sub>2</sub>O: 2 g, ammonium persulfate: 0.24 g, 35.0-37.0 wt. % HCl: 0.1 g), was injected to the mixture. After stirring solution under -43 °C for 12 h, fabricated PANI/MoS<sub>2</sub> nanocomposite was washed, centrifuged, and dried. In the case of pure PANI, it was prepared *via* identical synthetic procedure with PANI/MoS<sub>2</sub> nanocomposite except incorporation of MoS<sub>2</sub> nanosheet.

*Instrumentation:* FE-SEM images of samples were taken using a JSM-6701F (JEOL, Japan). Raman spectra of samples were obtained using a T64000 Raman spectrometer (Horiba Jobin Yvon, Japan) with a 514 nm argon (Ar) laser as the excitation source. The electrical conductivity measurements of samples were conducted with four-in-line probe method using a LORESTA-GP/MCP-T610 (MITSUBISHI, Japan).

### **2.2.2. Supercapacitor based on PANI/MoS<sub>2</sub> nanocomposite**

*Electrochemical measurements:* All electrochemical tests (CV and galvanostatic charge/discharge tests) were conducted in a three-electrode system (the reference and counter electrodes were Ag/AgCl and Pt, respectively) in 1 M H<sub>2</sub> SO<sub>4</sub> solution at a potential window of 0.0-0.8V. The working electrodes were prepared as follows. Firstly, The 1.5 mg of active

material (MoS<sub>2</sub> nanosheet, PANI, or PANI/MoS<sub>2</sub> nanocomposite) was mixed with PTFE (0.18 mg) and carbon black (0.18 mg). Next, the mixture was coated on stainless steel mesh (1 cm × 1 cm). Then, coated electrode was dried in at 25 °C for 24 h. The accurate gravimetric capacitance ( $C_m$ ) and internal resistance ( $R$ ) were calculated from galvanostatic charge/discharge curves using following equations.  $C_m$  (F g<sup>-1</sup>) = (I × t) / (m × V), where I is discharging current (mA), t is discharging time (s), m is mass of active material (mg), and V is potential window during discharging process (V).  $R$  (Ω g) = V / (I/g), where V is IR drop and (I/g) is discharging current density (A g<sup>-1</sup>).

## 2.3. PANI/graphene film for flexible supercapacitor electrodes

### 2.3.1. Fabrication of PANI/RGO film

*Materials:* Graphite powder (325 mesh), sodium nitrate ( $\text{NaNO}_3$ , 99 %), hydrazine monohydrate ( $\text{N}_2\text{H}_4\cdot\text{H}_2\text{O}$ , 98 %), aniline ( $\text{C}_6\text{H}_5\text{NH}_2$ ,  $\geq 99.5$  %), poly(tetrafluoroethylene) (PTFE;  $[\text{C}_2\text{F}_4]_n$ , 60 wt % dispersion in  $\text{H}_2\text{O}$ ), ( $\pm$ )-10-camphorsulfonic acid (CSA;  $\text{C}_{10}\text{H}_{16}\text{O}_4\text{S}$ , 98 %), and ammonium persulfate ( $[\text{NH}_4]_2\text{S}_2\text{O}_8$ , 98 %) were purchased from the Sigma-Aldrich Co. Sulfuric acid ( $\text{H}_2\text{SO}_4$ , 95 %), hydrogen peroxide ( $\text{H}_2\text{O}_2$ , 30~35.5 %), hydrochloric acid ( $\text{HCl}$ , 35~37 %), ammonia solution ( $\text{NH}_4\text{OH}$ , 28~30 %), and chloroform ( $\text{CHCl}_3$ , 99%) were purchased from the Samchun Chemical Co. Potassium permanganate ( $\text{KMnO}_4$ , 99.3 %) and phosphorus pentoxide ( $\text{P}_2\text{O}_5$ , extra pure) were purchased from the Junsei Chemical Co. *m*-Cresol ( $\text{C}_7\text{H}_8\text{O}$ ,  $\geq 98$  %) was purchased from the Tokyo Chemical Industry Co. Stainless steel mesh (SUS 304) was purchased from the Nilaco Corp. Potassium persulfate ( $\text{K}_2\text{S}_2\text{O}_8$ , 99 %) was purchased from the Kanto Chemical Co.

*Preparation of RGO:* Initially, graphene oxide solution was prepared by slightly modified Hummer's method. Before actual oxidation, graphite powder (5 g),  $\text{P}_2\text{O}_5$  (2.5 g) and  $\text{K}_2\text{S}_2\text{O}_8$  (2.5 g) were dissolved in  $\text{H}_2\text{SO}_4$  solution (30 ml) in a flask and the whole solution was heated at 80 °C for 6hr. The solution was filtered through mixed cellulose acetate filter (ADVANTEC) with excess

deionized water and remaining powder was kept in vacuum oven for 24 h. The  $\text{NaNO}_3$  (2.5g) was dissolved in  $\text{H}_2\text{SO}_4$  solution (115 ml) with vigorous stirring. The dried graphite powder was poured into well mixed  $\text{NaNO}_3/\text{H}_2\text{SO}_4$  solution with vigorous stirring, while kept in ice bath. In this state,  $\text{KMnO}_4$  (15g) was slowly poured into the solution in 10 min, keeping the temperature lower than  $20^\circ\text{C}$ . After 30 min, ice bath was removed and whole solution was heated at  $45^\circ\text{C}$  for 12hr, turning the color of solution to brownish gray paste. Then deionized water (230 ml) was poured into the paste, keeping the temperature below  $40^\circ\text{C}$ . Then deionized water (700 ml) was poured again and  $\text{H}_2\text{O}_2$  (25 ml) was slowly added to the solution, forming bright yellow particles in solution. This graphite oxide (GO) solution was washed with 10 wt %  $\text{HCl}$  solution three times and deionized water for several times until the pH of solution turns into 7. This solution was ultrasonicated for 1hr to exfoliate graphitic oxide into graphene oxide. Then the solution was centrifugated at 4000 rpm for 30 min to exclude residue. The graphene oxide solution was dried in vacuum oven and graphene oxide powder was obtained. The graphene oxide powder was dissolved in deionized water (3 mg/ml) and hydrazine monohydrate was added to the solution (the volume ratio of hydrazine monohydrate : water = 1 : 1000). And this solution was heated at  $80^\circ\text{C}$  for 12hr. After reduction process, the RGO solution was filtered by filter paper with

excess deionized water and was dried in vacuum oven, as in powder form, for further use.

*Preparation of PANI/RGO film:* As-prepared RGO powder was added to HCl solution (2.5 M, 40 ml) in Erlenmeyer flask. The solution was sonicated for 24 hr and aniline monomer was added, keeping vigorous stirring. After that, chloroform (60 ml) was added to the mixture, leading to the phase separation (chloroform phase at the bottom, aqueous phase on the top). Then the initiator, APS (the weight ratio of APS : aniline = 1.2:1) in HCl solution (3.75 M, 16 ml), was added to the above bi-phase solution and stirred for 24 hr at - 40 °C, resulting in the low-temperature interfacial polymerization. After polymerization process, the solution was centrifuged and dried. The feeding weight ratio of aniline to RGO was changed as 16:1, 12:1, and 8:1, and the obtained composites were named as PANI/RGO (PARG) 1, PARG 2, and PARG 3, respectively. The PARG powder was dispersed in ammonia solution (1.2 M, 215 ml) and vigorously stirred for 24 hr to de-dope the PANI chains on the RGO, resulting in de-doped PARG (De-PARG). This solution was centrifuged again and dried to collect powder. The real weight percentages of the PANI component in the De-PARG 1, 2 and 3 composites were calculated as 88 % for De-PARG 1, 76 % for De-PARG 2, and 60 % for De-PARG 3, respectively. The De-PARG powder was mixed with the CSA (the mole ratio of

PANI : CSA = 2:1) to re-dope the PANI chains on RGO, resulting in re-doped PARG (Re-PARG). The Re-PARG powder was added to the *m*-Cresol/chloroform solution (the volume ratio of *m*-cresol : chloroform = 7:3) to be as 2.38 wt % of total mass of solution and stirred for 3 hr and sonicated for 24 hr. The Re-PARG solution was drop-casted onto glass substrate and was annealed at 40 °C for 16 hr. Finally, the free standing film was obtained by detaching the annealed film from the glass substrate in the water. The Re-PARG films which were prepared by the De-PARG 1, 2 and 3 were named as the Re-PARG film 1, 2 and 3, respectively. The synthetic procedures of the PANI, De-PANI, and Re-PANI film were identical to those of the PARG, De-PARG, and Re-PARG film except incorporation of the RGO.

*Instrumentation:* SEM and TEM images were obtained with a JSM-6701F (JEOL, Japan) and LIBRA 120 (Carl Zeiss, Germany), respectively. Raman spectra were recorded using a Horiba-Jobin Yvon LabRam Aramis spectrometer with a 514 nm Ar-ion laser as the excitation source. The XPS were collected on Sigma probe (ThermoVG, U.K). Thermo-gravimetric analysis (TGA) was performed on a Perkin Elmer Pyris 6 TGA analyzer (USA) with a heating rate of 10 °C min<sup>-1</sup> under air flow of 20 ml min<sup>-1</sup>. The direct-current electrical conductivity measurements of samples were carried out with the four-probe method

using a KEITHLY 2400 (KEITHLY, USA). The XRD patterns were taken with a D8 Advance (Bruker, Germany) equipped with nickel (Ni)-filtered Cu K $\alpha$  radiation source ( $\lambda$ = 0.15406 nm).

### **2.3.2. Flexible supercapacitor based on PANI/RGO film**

*Electrochemical measurements:* The CV and galvanostatic charge/discharge tests were performed on a Wonatech WBCS 3000 potentiostat/galvanostat instrument to assess the electrochemical performances of the samples. All of the electrochemical measurements were performed in a three-electrode system in H<sub>2</sub>SO<sub>4</sub> solution (1 M) as the electrolyte at 25 °C, where the counter and reference electrodes were Pt and Ag/AgCl, respectively. The potential ranges for CV and galvanostatic charge/discharge tests were 0.0 to 0.8 V. The Re-PARG film and Re-PANI film were directly employed as the working electrodes. The pristine RGO was prepared for the working electrode as follows. The mixtures of the RGO (95 %) and PTFE (5 %) were coated onto the stainless steel mesh (1 x 1 cm<sup>2</sup>) and then dried in air at 25 °C for 24 h. The electrochemical behavior was first characterized by the CV test at a scan rate of 5 mV s<sup>-1</sup>. After that, the galvanostatic charge/discharge test was carried out at a current density of 0.45 A g<sup>-1</sup> to precisely evaluate the gravimetric capacitance, C<sub>m</sub> (F g<sup>-1</sup>), and internal resistance, R ( $\Omega$  g). The

mass of the Re-PARG film, Re-PANI film, and RGO for the CV and galvanostatic charge/discharge tests were 2 mg. The gravimetric capacitances ( $C_m$ ) were calculated by using the equation  $C_m = (i \times \Delta t) / (m \times \Delta V)$ , where  $C_m$  is the gravimetric capacitance in  $F g^{-1}$ ,  $i$  is the constant discharge current in mA,  $\Delta t$  is the discharge time in sec,  $m$  is the total mass of the active material in mg,  $\Delta V$  is the potential window in V. The internal resistances ( $R$ ) were estimated according to the  $R = \Delta V / (i/g)$ , where,  $R$  is the internal resistance in  $\Omega g$ ,  $\Delta V$  is the “IR drop (vertical voltage drop at the beginning of the discharge curve)” in V and  $(i/g)$  is the discharge current density in  $A g^{-1}$ . In order to study the electrochemical performance of the Re-PARG film depending on the size, the CV test was performed to the 2 and 60 mg of the Re-PARG film with the two different sizes (1.2 and 36  $cm^2$ ) in  $H_2SO_4$  (1M) solution at the scan rate of 5  $mV s^{-1}$ . The area capacitances,  $C_{area}$  ( $F cm^{-2}$ ), were calculated according to the following equation from the CV curves  $C_{area} = (\int i dV) / (v \times \Delta V)$ , where,  $C_{area}$  is the area capacitance in  $F cm^{-2}$ ,  $i$  is the response current density during the discharging in  $A cm^{-2}$ ,  $v$  is the scan rate in  $V s^{-1}$ , and  $\Delta V$  is the potential window in V. The cycle stability of the Re-PARG film (2 mg) and Re-PANI film (2 mg) were measured by the galvanostatic charge/discharge test at a current density of 0.45  $A g^{-1}$ .



in  $\text{H}_2\text{SO}_4$  solution (1M). For investigating the supercapacitor performance of the Re-PARG film under bending condition, the CV test was performed to the 6 mg of the Re-PARG films with two different bending angles of  $0^\circ$  and  $180^\circ$  at a scan rate of  $5 \text{ mV s}^{-1}$ .

### **3.1. PANI/SiO<sub>2</sub> nanocomposite for supercapacitor electrodes**

#### **3.1.1. Fabrication of PANI/SiO<sub>2</sub> nanocomposite**

PANI/SiO<sub>2</sub> nanocomposite (SP1) were synthesized by SSDP, as illustrated in Figure 6. First, SiO<sub>2</sub> NPs were dispersed in aqueous solution to serve as templates for adsorption of aniline monomers. Then, anilinium hydrochloride monomer ions were added to the SiO<sub>2</sub> NP solution. The monomer ions preferentially located on the surface of the SiO<sub>2</sub> NPs due to charge–charge interactions between the positively charged amine of the monomer and the negatively charged silica surface. After stirring for 1 h, chloroform was added to the monomer-impregnated SiO<sub>2</sub> NP solution to lower the melting temperature of the solution. When the temperature of the reaction solution dropped to –9 °C, the solubility of the anilinium hydrochloride in the aqueous phase decreased and became distributed in both the aqueous (water) and organic (chloroform) phases. [16]. Thus, through the  $\pi$ – $\pi$  stacking, additional anilinium hydrochloride monomer was adsorbed onto the surface of SiO<sub>2</sub> where monomer ions were pre-located [18,19]. After injection of APS as a water-soluble initiator, polymerization of monomer was initiated near the surface of the SiO<sub>2</sub> NPs. The growing PANI chains moved toward the interface between the aqueous and organic phases as result of insolubility in both aqueous and organic phases [20,21,22]. With both a hydrophilic part (amine

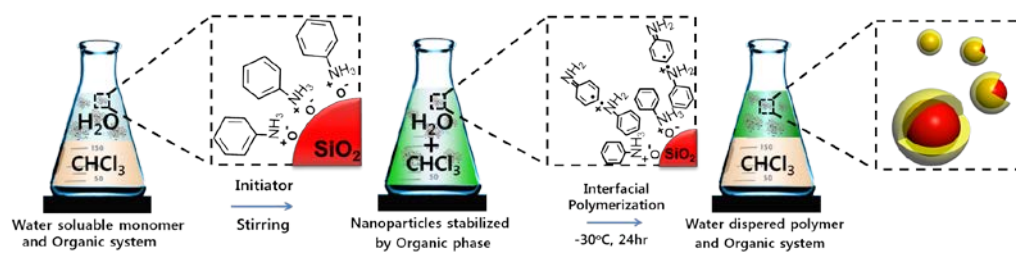


**Figure 6.** Illustrations of the sequential steps for synthesis of PANI/SiO<sub>2</sub> nanocomposite.

group) and a hydrophobic part (phenyl ring), anilinium hydrochloride monomers acted as surfactant [16,17,23]. Because the monomers and growing polymer chains acted as interfacial stabilizers, the organic phase could be well dispersed in the aqueous reaction medium. Additionally, the organic phase tended to separate the aniline monomers and grown PANI chains from the reactive ends of the chains in the aqueous phase. As a result, undesirable side reactions, such as ortho-coupling or Michael reductive additions, were suppressed, and the polymerization proceeded mainly in the para-direction (Figure 7) [16,21,22]. After 24 h of polymerization at  $-30\text{ }^{\circ}\text{C}$ , green SP1 was obtained.

Figure 8 shows FE-SEM and TEM images of SP1 particles of various diameters (*ca.* 18, 35, 63, and 130 nm). The size of the SP1 could be controlled by varying the size of SiO<sub>2</sub> NPs. The histograms of the particle size distributions are shown in Figure 9. The core/shell structure of SP1 was confirmed by TEM observation. The insets in Figure 8 clearly show that the SiO<sub>2</sub> NPs were encapsulated by a thin polymer shell. These results indicate that SiO<sub>2</sub> NPs of various sizes were successfully coated with polymer shell *via* SSDP. Based on the microscopic images, it could be considered that the SP1 has the similar shape as the previously reported PANI/SiO<sub>2</sub> nanocomposite synthesized by conventional polymerization method [20]. The compositions of

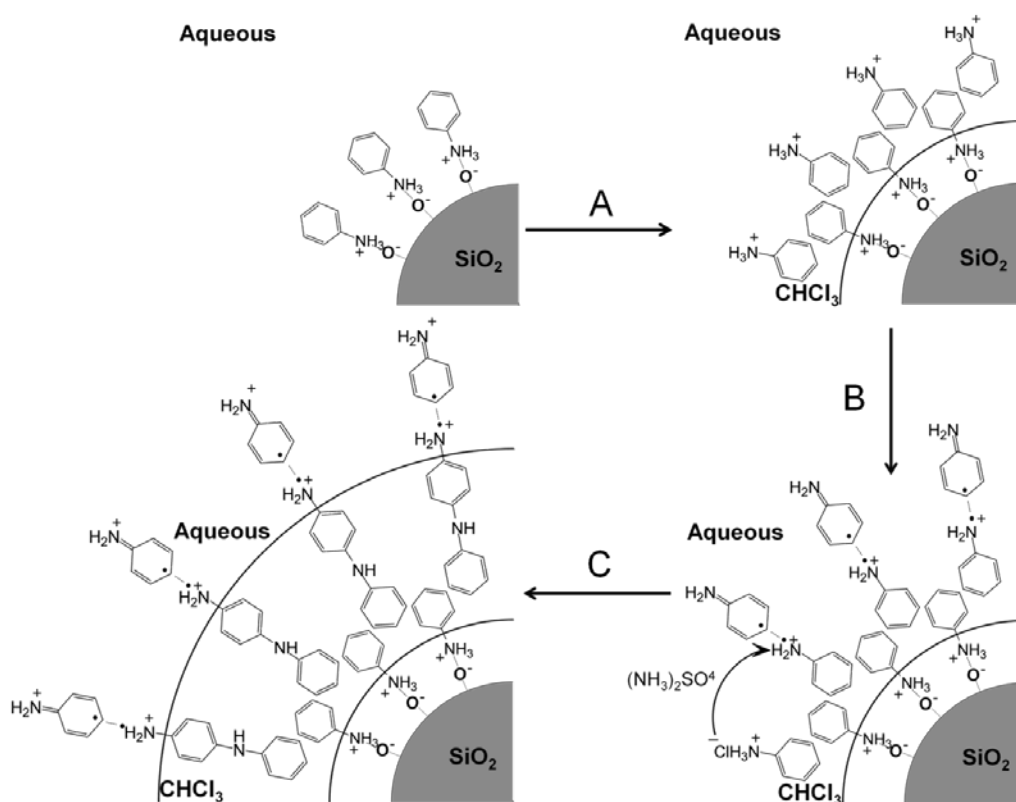


**Figure 7.** Illustrations of the sequential steps for synthesis of PANI/SiO<sub>2</sub> nanocomposite.

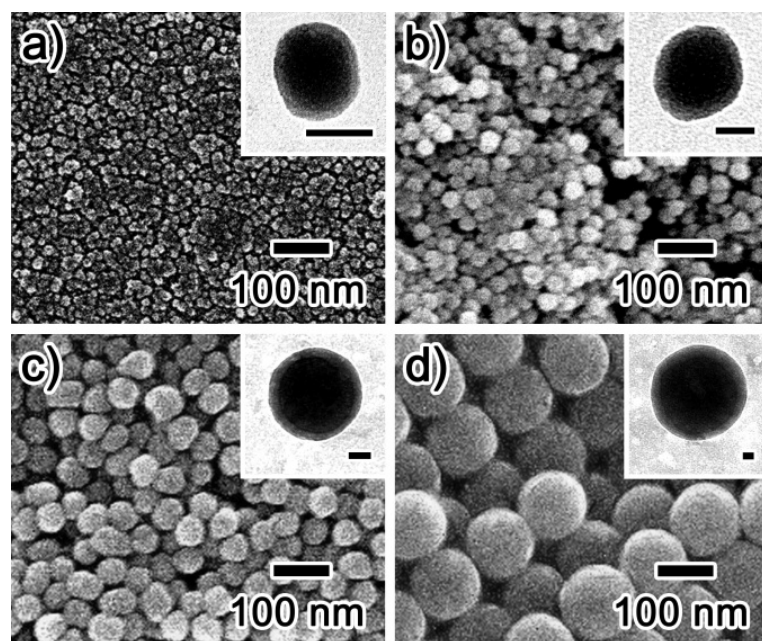


**Figure 8.** FE-SEM images and TEM images (inset) of SP1 with the average size of a) 18 nm, b) 35 nm, c) 63 nm, and d) 130 nm. The scale bars of inset images represent 15 nm.

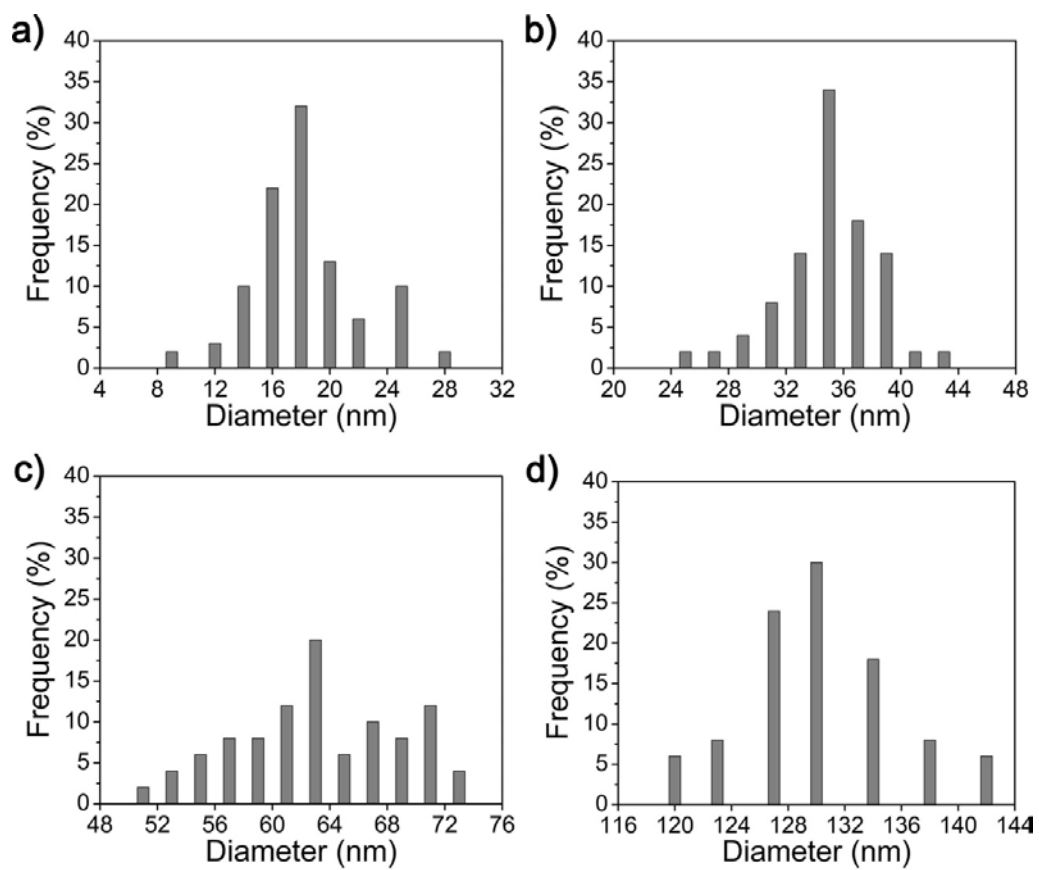


**Figure 9.** Size distribution histograms of SP1 with different diameters.

**Table 1.** Weight ratio of the pristine SiO<sub>2</sub> NPs and PANI/SiO<sub>2</sub> nanocomposite measured by EDX

Element percentage (wt%)	Pristine SiO <sub>2</sub> NPs	PANI/SiO <sub>2</sub> nanocomposite
C	7.99	37.47
O	64.69	35.98
Si	27.33	16.55
N	0.00	7.31
Cl	0.00	2.69
Totals	100	100



pristine SiO<sub>2</sub> NPs and SP1 were also investigated by EDX (Table 1). Compared to the pristine SiO<sub>2</sub> NPs, the %C values of the SP1 increased, whereas the %O and %Si values decreased due to adsorption of PANI on the silica surface. Notably, the detection of nitrogen, attributable to amine groups in PANI, confirms the existence of PANI on the surface of the SiO<sub>2</sub> NPs. In addition, the observation of chloride atoms in the SP1 indicates the hydrochloric acid doping state of the PANI. The detection of carbon in the pristine SiO<sub>2</sub> sample could be attributed to the carbon tape used for fixing the samples onto the EDX specimen mount. From these data, it was concluded that SP1 was successfully synthesized *via* the SSDP method, and the diameter of the SP1 could be controlled by varying the size of SiO<sub>2</sub> NP.

FT-IR spectroscopy of SP1 was also used to confirm the SSDP polymerization of PANI (Figure 10a). PANI/SiO<sub>2</sub> nanocomposite prepared by conventional polymerization method (SP2) were used for comparison. In the spectra of both SP1 and SP2, characteristic PANI peaks were observed at 1582, 1484, and 1310 cm<sup>-1</sup>, originating from quinone ring deformation, phenyl ring deformation, and C–N stretching of a secondary aromatic amine, respectively [21,22]. The existence of these peaks demonstrated the successful polymerization of PANI on the surface of the SiO<sub>2</sub> NPs.

XRD and NMR analyses were performed to investigate the *para*-direction

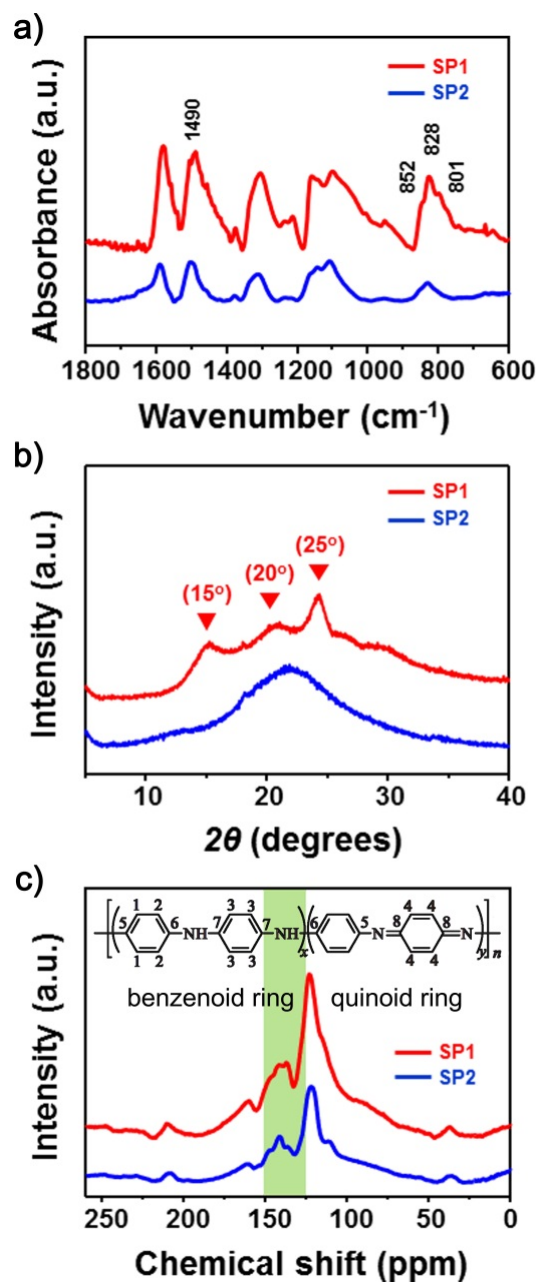


**Figure 10.** a) FT-IR spectra, b) XRD patterns, and c) Solid-state  $^{13}\text{C}$  NMR spectra of the EB-state SP1 (red line) and SP2 (blue line).

polymerization. XRD patterns of SP1 and SP2 in the emeraldine base (EB) state are shown in Figure 10b. EB-state PANI was obtained by deprotonation of the ES-state PANI using 0.8 M ammonia solution. The SP2, which was prepared *via* conventional polymerization method, exhibited a broad scattering background in its spectra, indicating that the amorphous region dominated the PANI of SP2 [17,23]. On the other hand, background peaks in the spectra of SP1 obviously decreased, and intense peaks at 15, 20, and 25° appeared. The *d*-spacing ( $\sim 3.5$  Å) associated with the diffraction peak at 25° corresponds to the face-to-face inter-chain stacking distance between phenyl rings [17,23]. Thus, the increased peak intensity at 25°, along with the decrease in background intensity, implies improved  $\pi$ - $\pi$  inter-chain stacking. These results suggest a more planar chain conformation with reduced torsion angles between the phenyl rings and the plane of the backbone, resulting in elongation of the effective conjugation length. Additionally, the increase crystallinity of SP1 also induces the improvement of conductivity. It is well known that CPs with higher conductivities are obtained in more homogeneous systems with a high degree of crystallinity [24–34]. In the conductivity model of CPs, electrons are transported along electronically isolated ordered regions through disordered regions where the electrons readily become localized. Consequently, the delocalization length of the electrons relies on the length of the ordered region

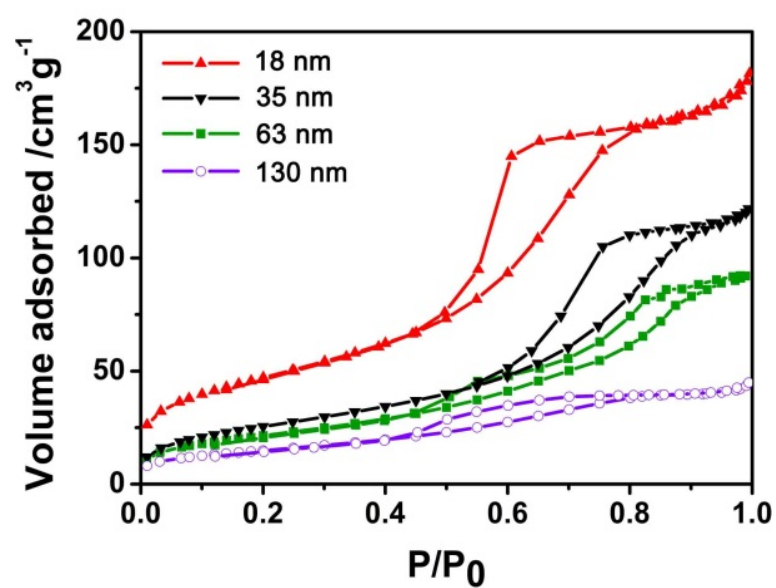
between the disordered regions. Based on previous studies [24–34] and XRD analysis, it is believed that the highly conductive and crystalline PANI was successfully fabricated on the SiO<sub>2</sub> NP.

Figure 10c shows the <sup>13</sup>C cross-polarization and magic-angle spinning NMR (<sup>13</sup>C CP–MAS NMR) spectra of the SP1 in the EB-state. The combined <sup>13</sup>C CP–MAS NMR technique is very powerful for resolving different microstructures present in the PANI shell. Four characteristic peaks were observed at 123, 137, 141, 148 (shoulder), and 158 ppm relative to tetramethylsilane. The clear peaks could be attributed to the ideal structure of PANI, as shown in the inset of Figure 10c: a peak at 158 (non-protonated carbon 8), a shoulder at 148 ppm (non-protonated carbon 5), peaks around 140 ppm (carbons 6, 7 and quinoid carbon 4), peak at 123 ppm (benzenoid carbons 1, 2), and a shoulder at 113 ppm (benzenoid carbon 3) [16]. It is important to note that the SP1 presented two distinct peaks around 137 ppm in its spectra, while the SP2 exhibited only one peak in this region. These two peaks in SP1 correspond to the idealized repeat structure of the EB-state PANI. The protonated carbons (C4) in the quinoid ring, without rotation around the bent linkage of the imine group (=N–), contributed two structures that appeared as two peaks around 137 ppm. [35,36]. In other words, the SP1 has an idealized EB repeat structure in its polymeric backbone, mainly oriented in the *para*-

direction. These results indicate that the PANI shell synthesized according to the SSDP method in this study had much greater *para*-direction-oriented aniline in its polymeric backbone compared to the PANI shell prepared by conventional polymerization method.

Nitrogen sorption experiments were performed to characterize the textural properties of different sized SP1. The nitrogen adsorption–desorption isotherms are displayed in Figure 11. The BET surface areas were *ca.* 170, 111, 78, and 53 m<sup>2</sup> g<sup>-1</sup> for diameters of 18, 35, 63, and 130 nm, respectively; thus, surface area was inversely proportional to the size of the SiO<sub>2</sub> NPs.

To investigate the electrical conductivity of the PANI, the material was pressed and prepared into disk-shape samples. The conductivity of bulk PANI (Figure 12) prepared *via* conventional polymerization was measured similarly for comparison. The electrical conductivities of the samples were measured by the four-probe method (Table 2). The electrical conductivity of the bulk PANI was found to be about 0.5 S cm<sup>-1</sup>. The conductivities of SP1 with diameters of 18, 35, 63, and 130 nm were measured to be *ca.* 25.6, 22.5, 18.3, and 16.4 S cm<sup>-1</sup>, respectively. On the other hand, the electrical conductivities of the SP2 were found to be *ca.* 1.42, 0.74, 0.58, and 0.32 S cm<sup>-1</sup> for samples with diameters of 18, 35, 63, and 130 nm, respectively. An improvement in the electrical conductivity of the SP1 samples (one order of magnitude higher than



**Figure 11.** Nitrogen adsorption/desorption isotherms of different sized SP1: 18 nm (red line), 35 nm (green line), 63 nm (black line), and 130 nm (purple line).

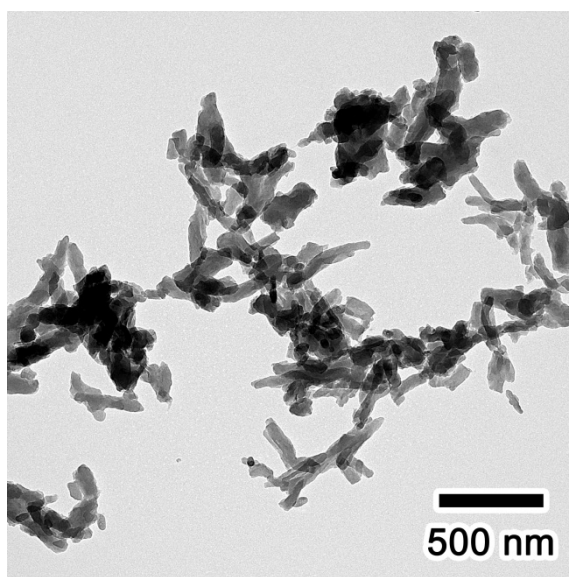


**Figure 12.** TEM image of the bulk PANI prepared by conventional polymerization method. Its diameter is *ca.* 1  $\mu\text{m}$ .

**Table 2.** Electrical conductivities of the PANI/SiO<sub>2</sub> nanocomposites.

Samples	Conductivity (S cm <sup>-1</sup> )			
	18 nm	35 nm	63 nm	130 nm
SP1 <sup>a</sup>	25.6	22.5	18.3	16.4
SP2 <sup>b</sup>	1.42	0.74	0.58	0.32

<sup>a</sup>The SSDP was applied for the fabrication of SP1 samples.

<sup>b</sup>The SP2 samples were synthesized by conventional polymerization.



for the SP2 and bulk PANI) was achieved by increasing the purity of the materials and by aligning the polymer chains. The electrical conductivity of CPs is strongly affected by the molecular structure and the polymer chain alignment [17,23]. Intramolecular electron transport is restricted by structural defects or impurities in conjugated structures, because CPs are principally one-dimensional systems with a typical conjugated backbone structure [17,23]. Therefore, the enhanced electrical conductivity of the SP1 originated from reduced structural defects in the polymer backbone and the *para*-direction-oriented polymerization. In addition, the electrical conductivities increased as the size of nanocomposite decreased in both SP1 and SP2 (from *ca.* 0.32 to *ca.* 1.42 S cm<sup>-1</sup> in SP1 and from *ca.* 16.4 to *ca.* 25.6 S cm<sup>-1</sup> in SP2). The smaller particles exhibited higher compactness and order when they were pressed into disks, thus leading to higher conductivity [37].

### **3.1.2. Supercapacitors based on PANI/SiO<sub>2</sub> nanocomposite**

The synthesized PANI/SiO<sub>2</sub> nanocomposite were prepared as electrodes for CV test, and galvanostatic charge/discharge was employed to evaluate the electrochemical properties and the capacitance performances. The specific capacitances of the electrodes were calculated from CV curves.

Figure 13a shows the CV curves of SP1 (18, 35, 63, 130 nm) and SP2 (18 nm) at a scan rate of 30 mV s<sup>-1</sup> in 1 M H<sub>2</sub>SO<sub>4</sub> solution. In the case of the SP1,

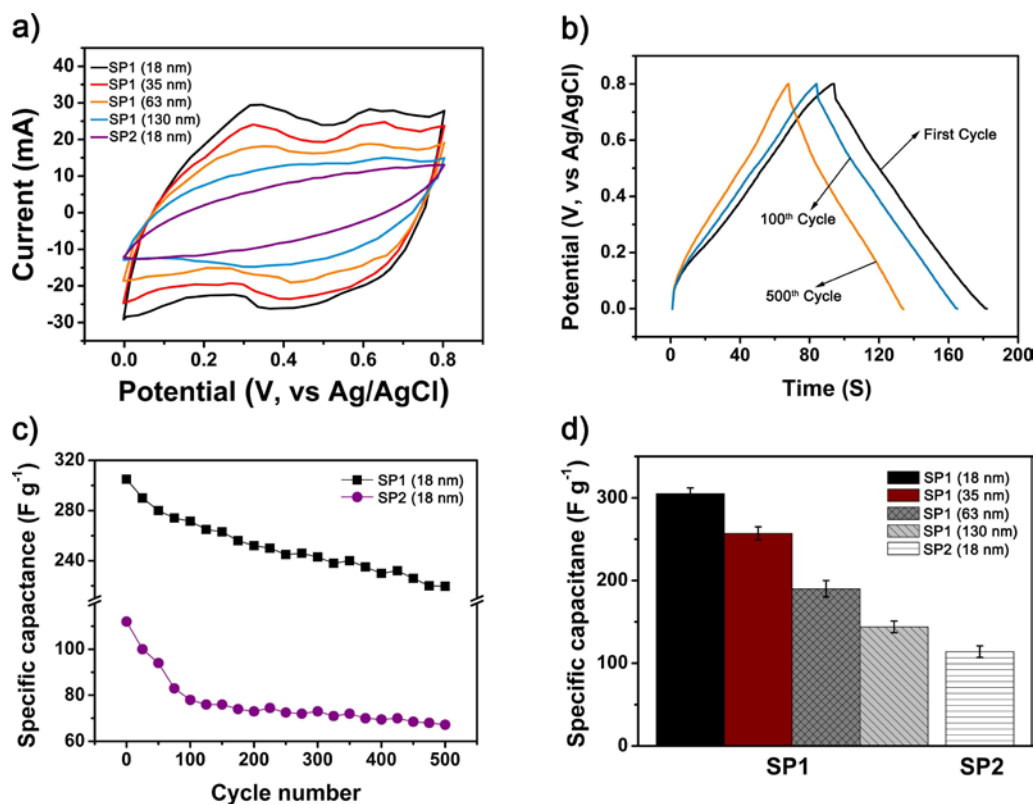


**Figure 13.** Cyclic voltammograms of SP1 (18, 35, 63, 130 nm) and SP2 (18 nm) at  $30 \text{ mV s}^{-1}$  between 0 and 0.8 V in 1M  $\text{H}_2\text{SO}_4$  solution; b) Galvanostatic charge/discharge curve of SP1 (18 nm) at current density of  $2.6 \text{ A g}^{-1}$  in 1M  $\text{H}_2\text{SO}_4$  solution; c) Specific capacitances of SP1 (18 nm) and SP2 (18 nm) as a function of cycle number at a current density of  $2.6 \text{ A g}^{-1}$  in 1 M  $\text{H}_2\text{SO}_4$  solution; d) Specific capacitances of SP1 (18, 35, 63, 130 nm) and SP2 (18 nm) at  $30 \text{ mV s}^{-1}$  between 0 and 0.8 V in 1M  $\text{H}_2\text{SO}_4$  solution.

there are two pairs of redox peaks, indicating the pseudo-capacitive characteristic of PANI. The first redox peak originated from the redox transition of PANI from a semiconducting state (leucoemeraldine state) to a conducting ES-state. Faradaic transformation from emeraldine to pernigraniline is ascribed to the second redox peak [38]. However, the SP2 (18 nm) exhibited a CV curve without obvious redox peaks, because the SP2 (18 nm) had relatively low conductivity, which reduced the conducting network available for facile redox reaction of PANI [39]. The CV curves for SP1 samples exhibited large rectangular areas and high current response, suggesting that SP1 supercapacitors could be made to have large capacitance [40]. Specific capacitance values of SP1 samples, calculated using equation 1, were found to be *ca.* 305, 257, 190, and 144 F g<sup>-1</sup> for materials with diameters of 18, 35, 63, and 130 nm respectively. The smaller (more conductive) SP1 exhibited higher specific capacitance. The high capacitance and capacitance tendency of SP1 samples were attributed to the following two factors: first, the smaller size of SP1 provided larger electrode/electrolyte interface areas, which could provide electrochemical accessibility to the electrolyte through the interface of PANI.<sup>46</sup> Thus, SP1 with large surface area could present the high capacitance performance by effective access of electrolyte to electrode in the redox mechanism [41]. second, the more highly conductive PANI offered a higher

conductivity path, facilitated a rapid charge/discharge process, and improved the redox activity [42]. The highly conductive path in SP1 originated from the enhanced conducting network that facilitated electron transfer in the electrode during the charge/discharge process [42]. The PANI network in SP1 is helpful for increasing electron transfer and the transport rate of electrolyte ions in the diffusion layer, both of which enhance the capacitance of the SP1 electrode [39]. Compared to SP1, the CV curve for SP2 (18 nm) exhibited small rectangular areas and a specific capacitance of  $112 \text{ F g}^{-1}$ . The SP1 (18 nm,  $305 \text{ F g}^{-1}$ ) exhibited enhanced specific capacitance compared with SP2 (18 nm,  $112 \text{ F g}^{-1}$ ). The SP1 (18 nm) presents high specific capacitance ( $305 \text{ F g}^{-1}$ ) compared to not only SP2 (18 nm,  $112 \text{ F g}^{-1}$ ) but also previously reported nanostructured-PANI [40, 42–47]. The specific capacitance of each nanocomposite studied by CV is summarized in Figure 13d.

The electrochemical stability of the SP1 (18 nm) was also investigated using cycled galvanostatic charge/discharge methods (Figure 13b). On the basis of the charge/discharge time, the charge storage capacity loss of SP1 was calculated as 12% loss after 100 cycles and 28% loss after 500 cycles. As shown in Figure 13c, the charge storage capacity of the SP2 (18 nm) decreased more rapidly (30% loss after 100 cycles and 40% loss after 500 cycles) compared with that of the SP1 (18 nm). At the cycle-life test, the dope or

dedope of  $H^+$  into or from the PANI chains on the  $SiO_2$  NP results in the mechanical degradation like a swelling, breaking, and shrinkage of the nanostructured PANI, thus, leading to fading of capacitance [48–51]. In comparison to the SP2 electrode, the better cycle life of SP1 maybe mainly caused by increase crystalline region at backbone of PANI, which provide higher density to PANI and improved resistance toward change of the nanostructure of PANI at the cycle-life test [52].

In conclusion, highly conductive and crystalline PANI was successfully coated onto various sized- $SiO_2$  NPs using the SSDP. The diameter of the nanocomposite was controlled from 18 nm to 130 nm by varying the size of the  $SiO_2$  NP. As the diameter of the PANI/ $SiO_2$  nanocomposite decreased (from 130 to 18 nm), the electrical conductivity increased (from 16.4 to 25.6  $S\ cm^{-1}$ ). When applied as potential electrode materials for supercapacitors, synthesized PANI/ $SiO_2$  nanocomposite exhibited capacity as high as 305  $F\ g^{-1}$  and had enhanced cycle-life performance compared to nanocomposite prepared by conventional polymerization method. The high conductivity and large surface area facilitated the charge/discharge of PANI, and the increased crystalline structure of PANI prevented severe deterioration of the polymer structure. The highly conductive and crystalline PANI/ $SiO_2$  nanocomposites prepared by SSDP can be used in various applications, such as batteries, sensors, actuators,

corrosion protection, electro-chromic devices, and dye-sensitized solar cells.

## **3.2. PANI/MoS<sub>2</sub> nanocomposite for supercapacitor electrodes**

### **3.2.1. Fabrication of PANI/MoS<sub>2</sub> nanocomposite**

The PANI/MoS<sub>2</sub> nanocomposite was synthesized as follows. First, prepared MoS<sub>2</sub> nanosheet was added to aniline hydrochloride solution and then sonicated for 2h. Next, chloroform was injected to mixture, and then, stirred and sonicated for 1 min and 1h, respectively. After sonication process, the mixture was stirred under temperature of  $-43^{\circ}\text{C}$ . When the temperature of solution decreased to  $-9^{\circ}\text{C}$ , initiator solution was injected to the mixture. After stirring solution for 12 h under  $-43^{\circ}\text{C}$ , as-synthesized PANI/MoS<sub>2</sub> nanocomposite was washed, centrifuged, and dried. Figure 14 depicts FE-SEM images of the MoS<sub>2</sub> nanosheets and obtained PANI/MoS<sub>2</sub> nanocomposite. Figure 14a illustrates that MoS<sub>2</sub> nanosheets possesses smooth surface. In contrast, PANI/MoS<sub>2</sub> nanocomposite shows that honeycomb-like structured PANI is polymerized on the MoS<sub>2</sub> nanosheets (Figure 14b), which is characteristic morphology of the PANI synthesized by SSDP to be distinguished from the PANI which has been polymerized by other polymerization processes [16]. This result reflects that PANI has been successfully polymerized on the MoS<sub>2</sub> nanosheet *via* SSDP. Figure 15 displays the Raman spectra of pristine MoS<sub>2</sub> nanosheets, pure PANI, and PANI/MoS<sub>2</sub> nanocomposite. The MoS<sub>2</sub> nanosheets demonstrates its characteristic peaks

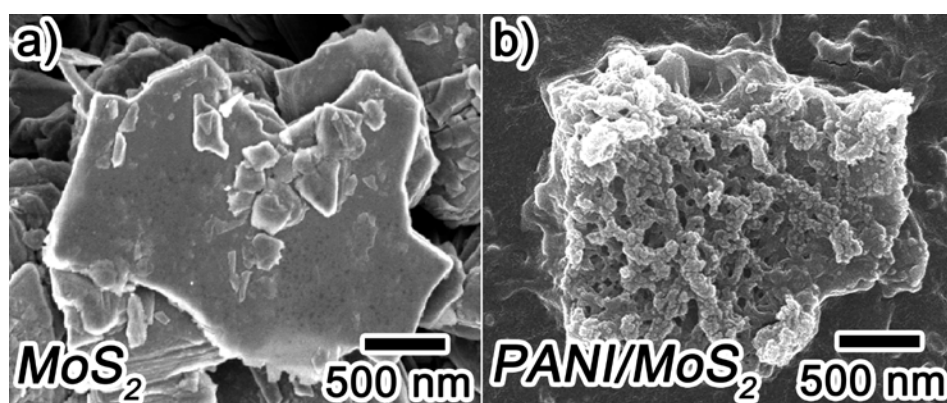


**Figure 14.** SEM images of a)  $\text{MoS}_2$  nanosheets and b)  $\text{PANI}/\text{MoS}_2$  nanocomposite.



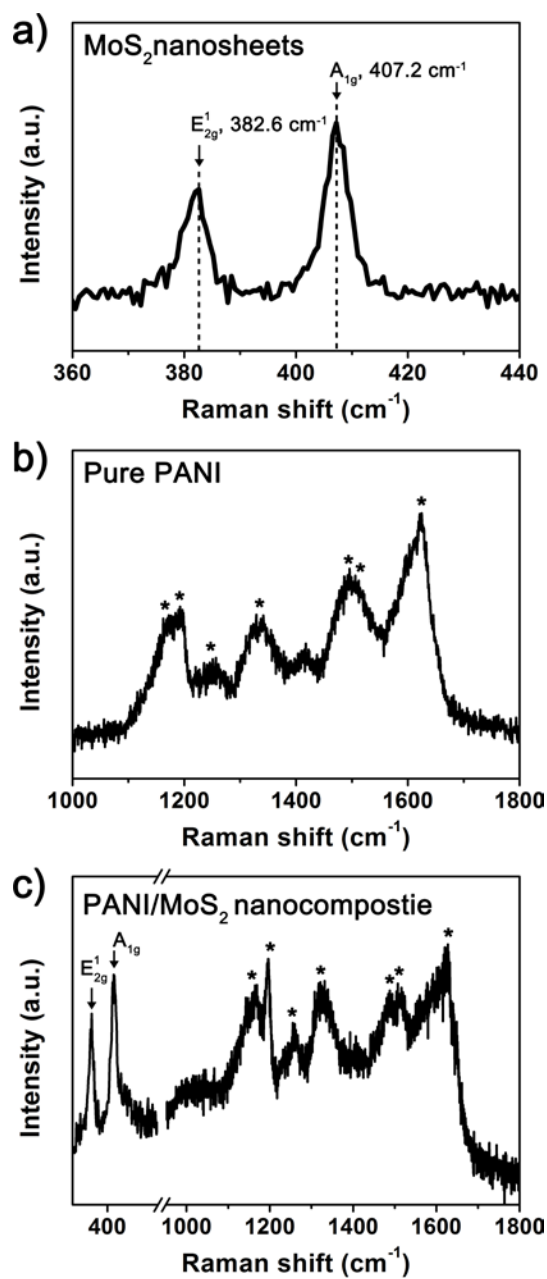


**Figure 15.** Raman spectra of a) MoS<sub>2</sub> nanosheets, b) PANI, and c) PANI/MoS<sub>2</sub> nanocomposite.

at 382.6 and 407.2  $\text{cm}^{-1}$  (Figure 15a), corresponding to  $E_{2g}^1$  mode vibration originated from in-plane vibration of molybdenum (Mo) atom and sulphur (S) atoms in opposite directions and  $A_{1g}$  mode vibration related with the out-of-plane vibration of only S atoms in opposite directions [53,54]. It has been reported that layer number of  $\text{MoS}_2$  sample can be simply determined by measuring frequency difference between  $E_{2g}^1$  and  $A_{1g}$  modes because two Raman modes are very sensitive to thickness of the  $\text{MoS}_2$  sample [53]. The frequency difference of the  $\text{MoS}_2$  nanosheets prepared here was found to be 24.6  $\text{cm}^{-1}$ , corresponding to five-to-six-layered  $\text{MoS}_2$  nanosheet. This result indicates that bulk  $\text{MoS}_2$  has been completely exfoliated to five-to-six-layered  $\text{MoS}_2$  nanosheet [53]. Pure PANI shows its own intrinsic peaks at 1169, 1192, 1253, 1343, 1495, 1516, and 1623  $\text{cm}^{-1}$  (Figure 15b), assigned to C-H bending of benzenoid ring, C-H bending of benzenoid ring, symmetric C-N stretching, C-N<sup>+</sup> stretching, C=N stretching of the quinoid ring, C=C stretching vibration of quinoid ring, and C-C bending of benzenoid ring [3,55–57]. For PANI/ $\text{MoS}_2$  nanocomposite (Figure 15c), it displays Raman peaks of both  $\text{MoS}_2$  (382.1 and 406.8  $\text{cm}^{-1}$ ) and PANI components (1169, 1192, 1253, 1343, 1495, 1516, and 1623  $\text{cm}^{-1}$ ). The frequency difference of  $\text{MoS}_2$  in the PANI/ $\text{MoS}_2$  nanocomposite was measured to 25.2  $\text{cm}^{-1}$ , corresponding to five-

to-six-layered MoS<sub>2</sub>. These peaks point out that PANI has been polymerized on the five-to-six-layered MoS<sub>2</sub> nanosheet during the polymerization process. Next, electrical conductivity and electrochemical properties of the MoS<sub>2</sub> nanosheet, pure PANI, and PANI/MoS<sub>2</sub> nanocomposite were investigated. Firstly, the electrical conductivities of the samples were measured using the four-in-line probe method (measuring the voltage differences between horizontally separated two probes by applying constant current to horizontally separated two other probes). Pristine MoS<sub>2</sub> nanosheet and pure PANI exhibited the electrical conductivities of *ca.* 5.6x10<sup>-5</sup> and *ca.* 10.6 S cm<sup>-1</sup>, respectively (Figure 16). Interestingly, after the PANI is coated on the MoS<sub>2</sub> nanosheets, PANI/MoS<sub>2</sub> nanocomposite showed increased electrical conductivity of *ca.* 28.6 S cm<sup>-1</sup> (Figure 16), which is higher electrical conductivity than those of pristine MoS<sub>2</sub> and pure PANI. It has been clearly proven that the electrical conductivity of CPs is strongly affected by the alignment of the polymer chains [23]. When electron migrates in pelletized PANI/MoS<sub>2</sub> nanocomposite sample, the electron would majorly moves along the horizontally aligned PANI chains (Figure 14b). In contrast, for the case pure PANI, electrons would evenly diffuse along the both horizontal and vertical directions because the pure PANI interconnected randomly along horizontal and vertical directions (Figure 17). In this case, the vertical direction plays a role as obstacles for electron

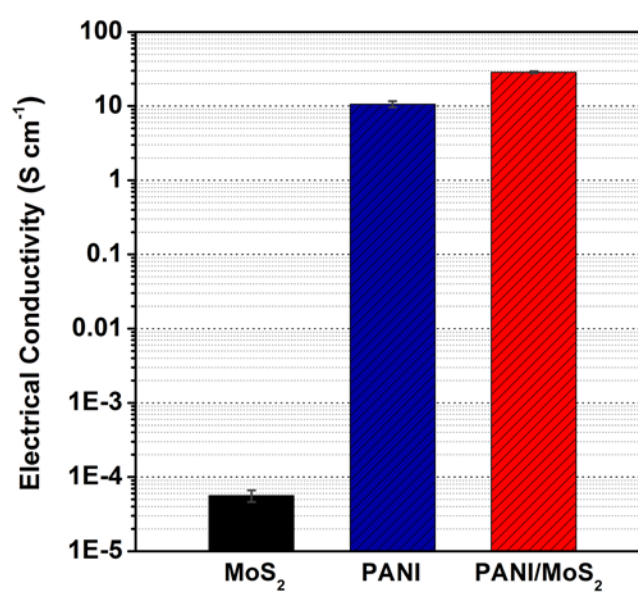


**Figure 16.** Electrical conductivity of the MoS<sub>2</sub> nanosheets, PANI, and PANI/MoS<sub>2</sub> nanocomposite.

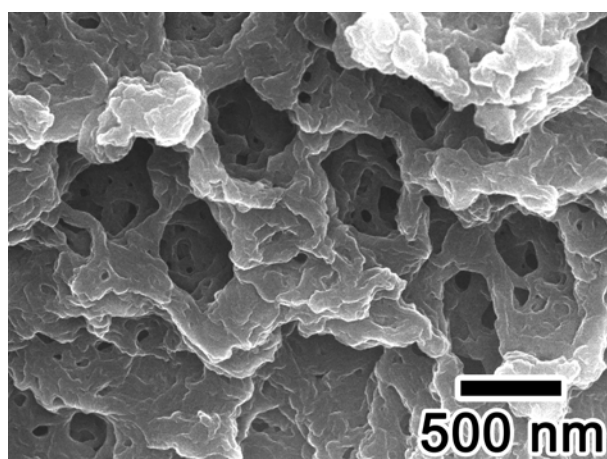


**Figure 17.** SEM image of pure PANI synthesized by SSDP.

migration in comparison with the case of PANI/MoS<sub>2</sub> nanocomposite. Thus, improved high electrical conductivity of PANI/MoS<sub>2</sub> nanocomposite might be attributed to well structural alignment of PANI chains along the horizontal direction on the flat MoS<sub>2</sub> nanosheet.

### **3.2.2. Supercapacitor based on PANI/MoS<sub>2</sub> nanocomposite**

Figure 18a presents the CV curves of MoS<sub>2</sub> nanosheet, PANI, and PANI/MoS<sub>2</sub> nanocomposite within a potential window from 0.0 to 0.8 V (vs AgCl/Ag) at a scan rate of 5 mV s<sup>-1</sup>. The MoS<sub>2</sub> nanosheet presents the low current response with distinctive peak at 0.8 V (Figure 19), reflecting low pseudo-capacitance behaviour. This peak might be attributed to the reduction of Mo atoms at the edge of the nanosheet. During the cathodic scan, holes are migrated from the electrolyte into n-type MoS<sub>2</sub> and recombined with electrons, resulting in sharp cathodic reduction peak at 0.8 V. In contrast, intensity of anodic current was very small due to the small number of holes in an n-type material MoS<sub>2</sub> [58]. In the case of the PANI, it exhibits larger current response than MoS<sub>2</sub> nanosheet with a couple of redox peaks (faradaic transformation of emeraldine to pernigraniline) [59] revealing the higher pseudo-capacitance of the PANI than MoS<sub>2</sub> nanosheet. For PANI/MoS<sub>2</sub> nanocomposite, it demonstrates highest current response with redox peaks, representing the

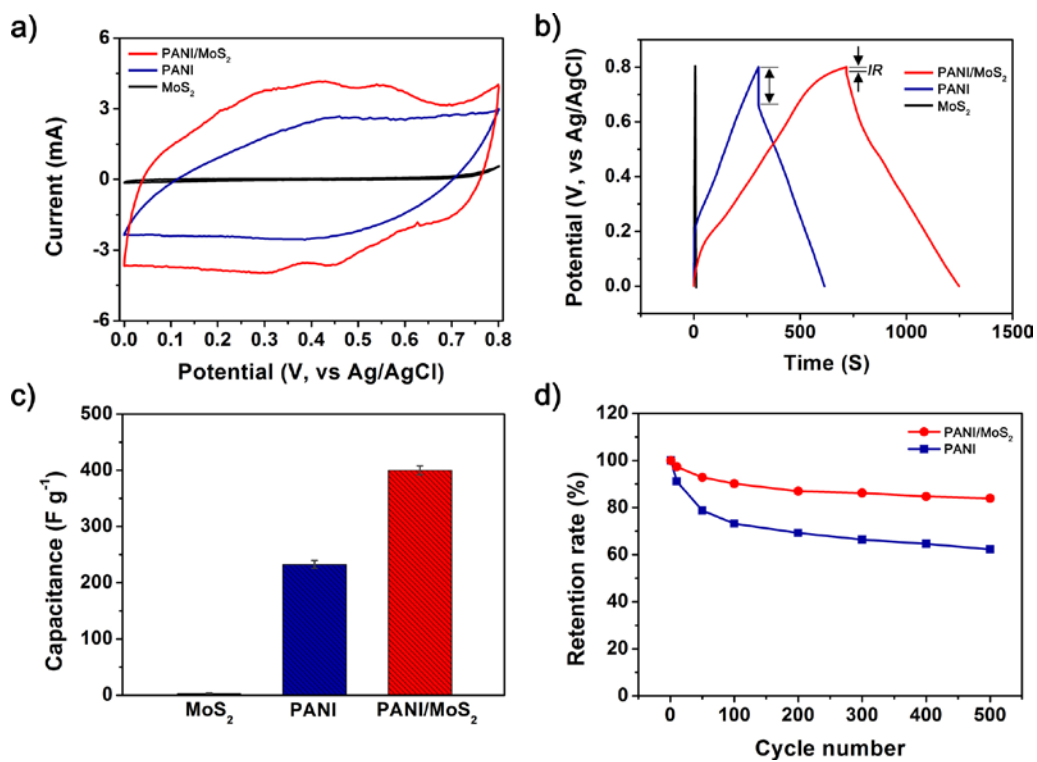


**Figure 18.** a) Cyclic voltammograms of MoS<sub>2</sub> nanosheet, PANI, and PANI/MoS<sub>2</sub> nanocomposite at a scan rate of 5 mV s<sup>-1</sup>, b) galvanostatic charge/discharge curves of MoS<sub>2</sub> nanosheet, PANI, and PANI/MoS<sub>2</sub> nanocomposite at a current density of 0.6 A g<sup>-1</sup>, c) gravimetric capacitances of MoS<sub>2</sub> nanosheet, PANI, and PANI/MoS<sub>2</sub> nanocomposite at a current density of 0.6 A g<sup>-1</sup>, and d) cycling stability of MoS<sub>2</sub> nanosheets, PANI, and PANI/MoS<sub>2</sub> nanocomposite at a current density of 0.6 A g<sup>-1</sup>.

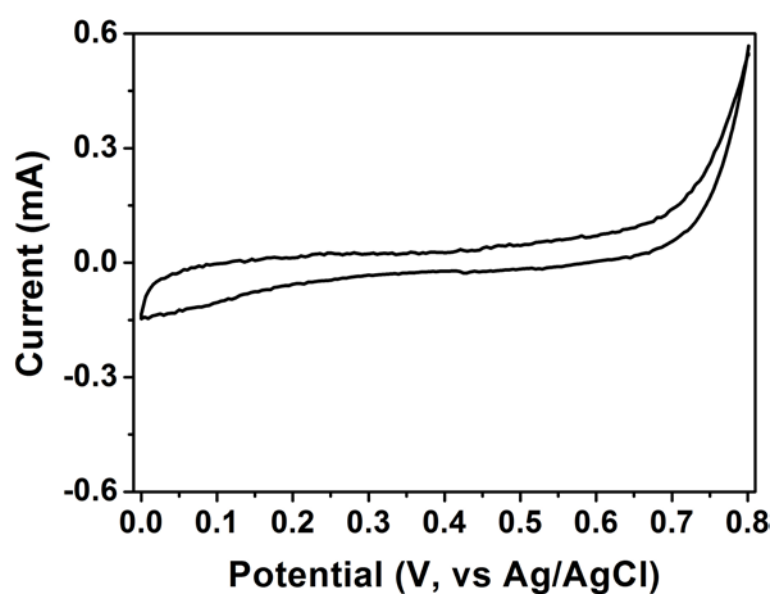


**Figure 19.** CV curve of pristine MoS<sub>2</sub> nanosheet at a scan rate of 5 mV s<sup>-1</sup>.



highest pseudo-capacitance of the PANI/MoS<sub>2</sub> nanocomposite.

Figure 18b illustrates galvanostatic charge/discharge curves of MoS<sub>2</sub> nanosheet, PANI, and PANI/MoS<sub>2</sub> nanocomposite within a potential window from 0.0 to 0.8 V (vs AgCl/Ag) at a current density of 0.6 A g<sup>-1</sup>. In accordance with the CV curves, galvanostatic charge/discharge curves show the highest capacitance of the PANI/MoS<sub>2</sub> nanocomposite and pseudo-capacitance behaviour of the all samples by representing longest discharging time of the PANI/MoS<sub>2</sub> nanocomposite and nonlinear-shaped galvanostatic charge/discharge curves of all samples (Figure 20). Additionally, galvanostatic charge/discharge curves depicts the lower “IR drop” of PANI/MoS<sub>2</sub> nanocomposite than pristine PANI, indicating that PANI/MoS<sub>2</sub> nanocomposite possesses lower internal resistance than PANI. Precise internal resistances of PANI/MoS<sub>2</sub> nanocomposite and PANI were calculated based on the “IR drop” and it was founded to be *ca.* 0.03 and 0.23 Ω g, respectively. For MoS<sub>2</sub> nanosheet, no “IR drop” was observed, indicating that internal resistance of MoS<sub>2</sub> nanosheet is extremely low. The charging and discharging process of supercapacitor electrode is related with migration of charge ions from electrolyte to the electrode and inter-electrode. During this migration, losses take place and these losses are expressed as internal resistance. [60]. From this point of view, it can be deduced that the extremely low internal resistance of

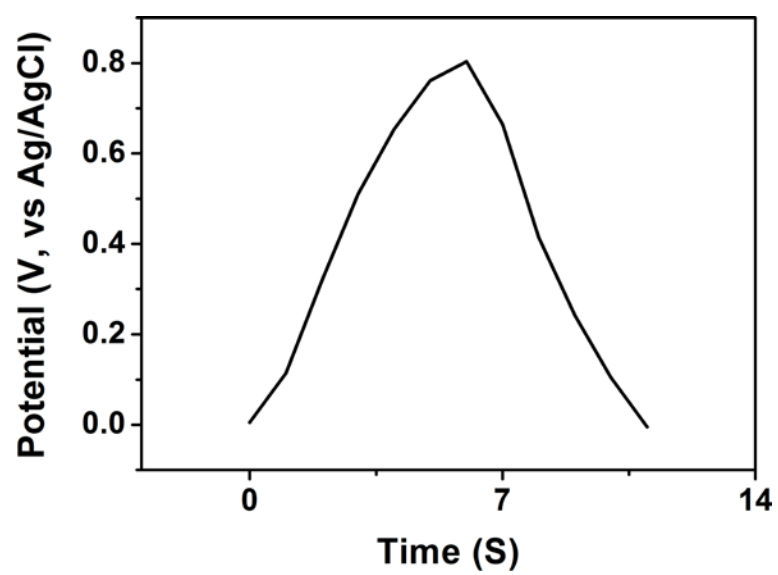


**Figure 20.** Galvanostatic charge/discharge curve of pristine MoS<sub>2</sub> nanosheet at a current density of 0.6 A g<sup>-1</sup>.

MoS<sub>2</sub> nanosheet is originated from the multilayer structure of MoS<sub>2</sub> nanosheets stacked in van der Waals force, enabling facile intercalation of proton (H<sup>+</sup>) ions [61]. In the cases for PANI/MoS<sub>2</sub> nanocomposite, the improved internal resistance would be owing to (1) well aligned honeycomb-like structure PANI on MoS<sub>2</sub> nanosheet and (2) introduce of MoS<sub>2</sub> nanosheet possessing extremely low internal resistance, both facilitating migration of charge carriers. Possessing low internal resistance is extremely important in supercapacitor electrode application for the long-lifetime. The higher internal resistance of electrode induces larger unwanted Joule-heating, resulting in short-lifetime of electrodes [42,62]. Therefore, this result implies that the PANI/MoS<sub>2</sub> nanocomposite can be suitably used as long-life time supercapacitor electrode.

In addition to internal resistance, accurate gravimetric capacitance was also measured from the galvanostatic discharging curves (Figure 18c). The MoS<sub>2</sub> nanosheet and PANI exhibited gravimetric capacitances of *ca.* 3 and *ca.* 232 F g<sup>-1</sup>, respectively. When MoS<sub>2</sub> nanosheet is combined with the PANI, PANI/MoS<sub>2</sub> nanocomposite demonstrates significantly improved gravimetric capacitance of *ca.* 400 F g<sup>-1</sup>, which is much higher value than pristine MoS<sub>2</sub> nanosheet and pure PANI. The capacitance of the supercapacitor electrode is crucially depends on following three factors: (1) types of the materials, (2)

electrical conductivity, and (3) specific surface area [1]. The PANI/MoS<sub>2</sub> nanocomposite consists of MoS<sub>2</sub> and PANI possessing pseudo-capacitance, thus, this nanocomposite possesses high potential that could exhibits large pseudo-capacitance. In this condition, highly electrical conductive PANI in the PANI/MoS<sub>2</sub> nanocomposite would provide high conductivity path to MoS<sub>2</sub> nanosheet and this would promote fast redox reaction of MoS<sub>2</sub> nanosheet, giving rise to improved high pseudo-capacitance of the PANI/MoS<sub>2</sub> nanocomposite.

Figure 18d plots cycling stabilities of the PANI, MoS<sub>2</sub> nanosheet, and PANI/MoS<sub>2</sub> nanocomposite. The retention rate of PANI decreased from 100 % to 62 % after 500 cycles. On the contrast, PANI/MoS<sub>2</sub> nanocomposite shows the improved charge retention rate of 84 %. The enhanced electrochemical stability of PANI/MoS<sub>2</sub> nanocomposite might be due to following reasons: (1) it has been known that MoS<sub>2</sub> possesses outstanding electrochemical stability like graphene, which is originated from the excellent mechanical strength of MoS<sub>2</sub> [61,63]. Consequently, improved electrochemical stability of PANI/MoS<sub>2</sub> nanocomposite might be originated from existence of highly electrochemically stable MoS<sub>2</sub> component in the PANI/MoS<sub>2</sub> nanocomposite. (2) while the PANI electrode is repeatedly charged and discharged during cycling stability test, the PANI chains are repeatedly bumped each other by

repeated swelling and shrinkage, leading to cracking and breaking of PANI chains, gradual loss in electrical conductivity, and decrease in capacitance [64]. For the case of PANI/MoS<sub>2</sub> nanocomposite, well aligned honeycomb-like structure PANI on flat MoS<sub>2</sub> nanosheet offers sufficient swelling volume along both vertical and horizontal directions, which would impede the cracking and breaking of PANI chains and enhance the cycling stability.

### **3.3. PANI/graphene film for flexible supercapacitor electrodes**

#### **3.3.1. Fabrication of PANI/RGO film**

Figure 21 shows a schematic illustration of the synthetic procedure of PANI/RGO film. First, the RGO powder was added to HCl solution and sonicated for 24 hr to obtain homogeneous dispersion. Then aniline monomer was added, keeping vigorous stirring. After stirring the above solution for 1 hr, chloroform was mixed to prevent the freezing of the reaction solution. When the temperature of the solution decreased to -9 °C in the chiller, the anilinium hydrochloride became partially insoluble in the aqueous phase and co-existed in both the aqueous and organic phase [16]. Thus, the hydrophobic part of the anilinium hydrochloride (phenyl group) adsorbed on the aromatic surface of the RGO by the  $\pi$ - $\pi$  interaction in the organic phase [65]. After addition of initiator, APS, the polymerization of aniline occurred on the surface of the RGO, and then PARG was obtained. After washing and drying, the primary dopant of ES-state PANI in PARG was removed by ammonia solution, resulting in De-PARG. After additional washing and drying, De-PARG was re-doped by CSA, and then Re-PARG was dissolved in *m*-Cresol/chloroform solvent. This secondary doping process is very helpful in changing the conformation of PANI chains from a compact coil to an expanded structure in

the solvent [66]. Furthermore, it is expected that RGO also induced the more

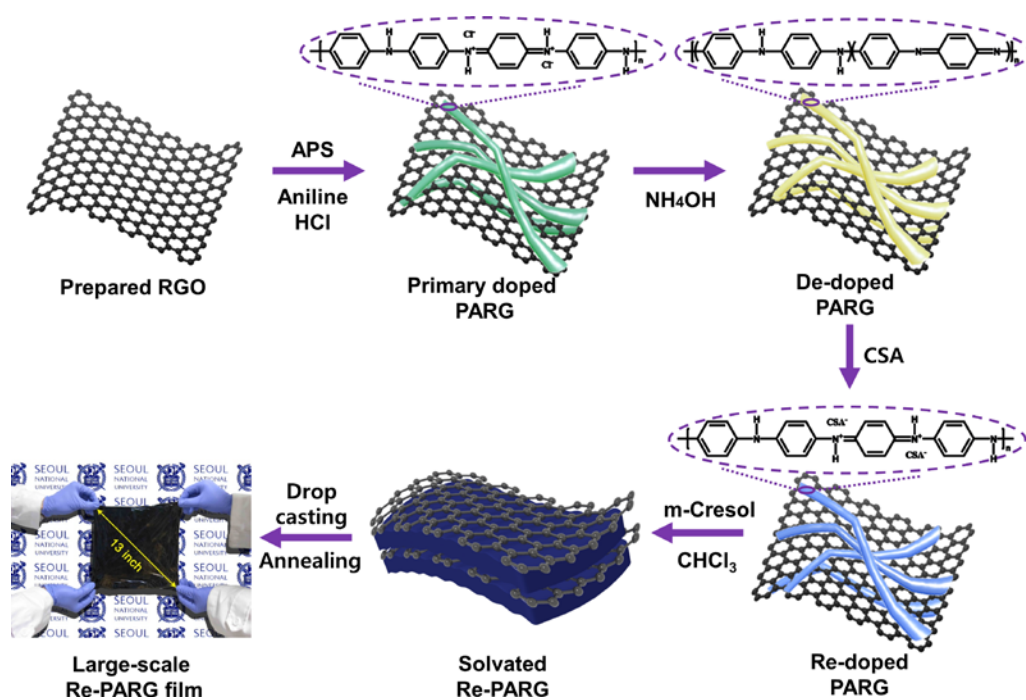


**Figure 21.** Schematic illustration of the sequential steps for fabricating large-scale Re-PARG film.

expanded coil conformation of PANI chains in the solution *via* strong  $\pi$ - $\pi$  interactions between the quinoid rings of the PANI chains and the basal planes of RGO. Finally, the prepared solution was cast onto a large-sized glass substrate (23 cm x 23 cm, 13 inch) and placed on a heat source to evaporate any residual solvent. Due to the high surface polarity and wettability of the m-cresol solvent, the prepared solution was well attached to the glass substrate [66,67]. After the annealing process, as shown in the last picture of Figure 21, we obtained the large-scale Re-PARG film (23 cm x 23 cm, 13 inch). Additionally, we were able to fabricate the smaller sized film (16 cm x 13 cm, 8 inch) easily by changing the size of the glass substrate (Figure 22), demonstrating the great advantage of the solution process for producing the scalable film.

Figure 23a–d illustrate the SEM images of pristine RGO, PARG, Re-PANI film, and Re-PARG film, respectively. As shown in Figure 23a, pristine RGO exhibits the wrinkled and silk-like structure related with the intrinsic characteristics of graphene [59,68]. The TEM images of RGO (Figure 24a) additionally show the thin and transparent two-dimensional morphology with the size of several micrometers, suggesting that few layers of RGO were utilized to synthesize the Re-PARG film. The SEM and TEM images of the



PARG (Figure 23b and Figure 24b) clearly show that the PANI was uniformly

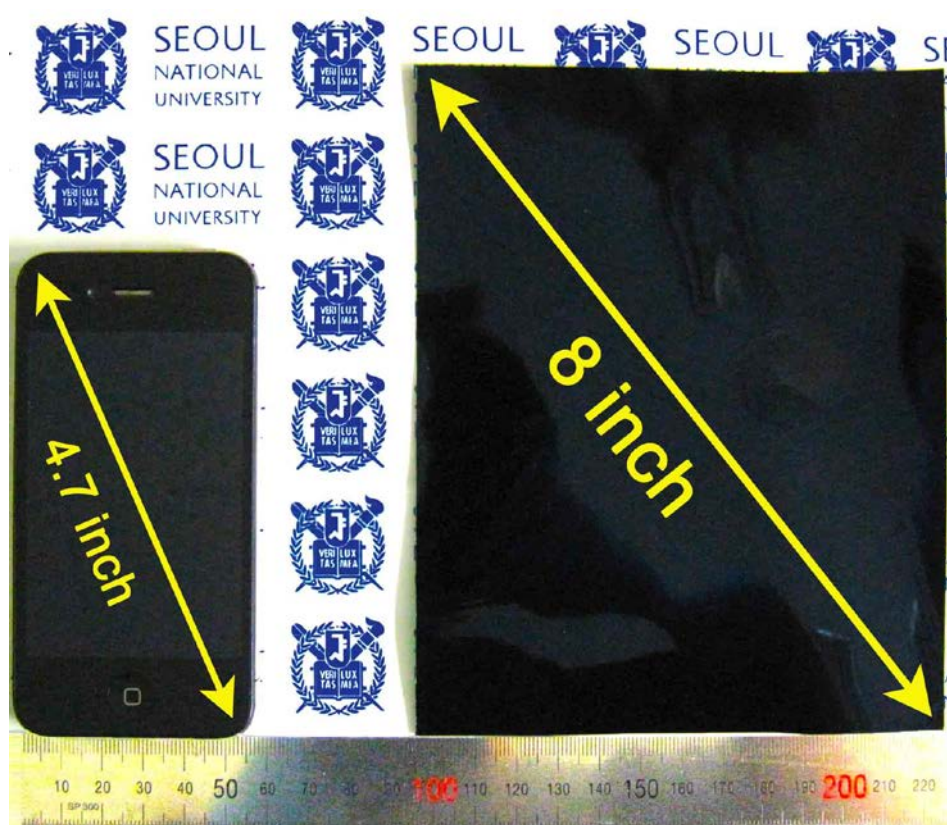


**Figure 22.** Digital camera images of (left) electronic device (10.5 cm x 5.5 cm, 4.7 inch) and (right) Re-PARG film (16 cm x 13 cm, 8 inch) with a ruler below the electronic device and film for scale. The scale bars of ruler represent mm.

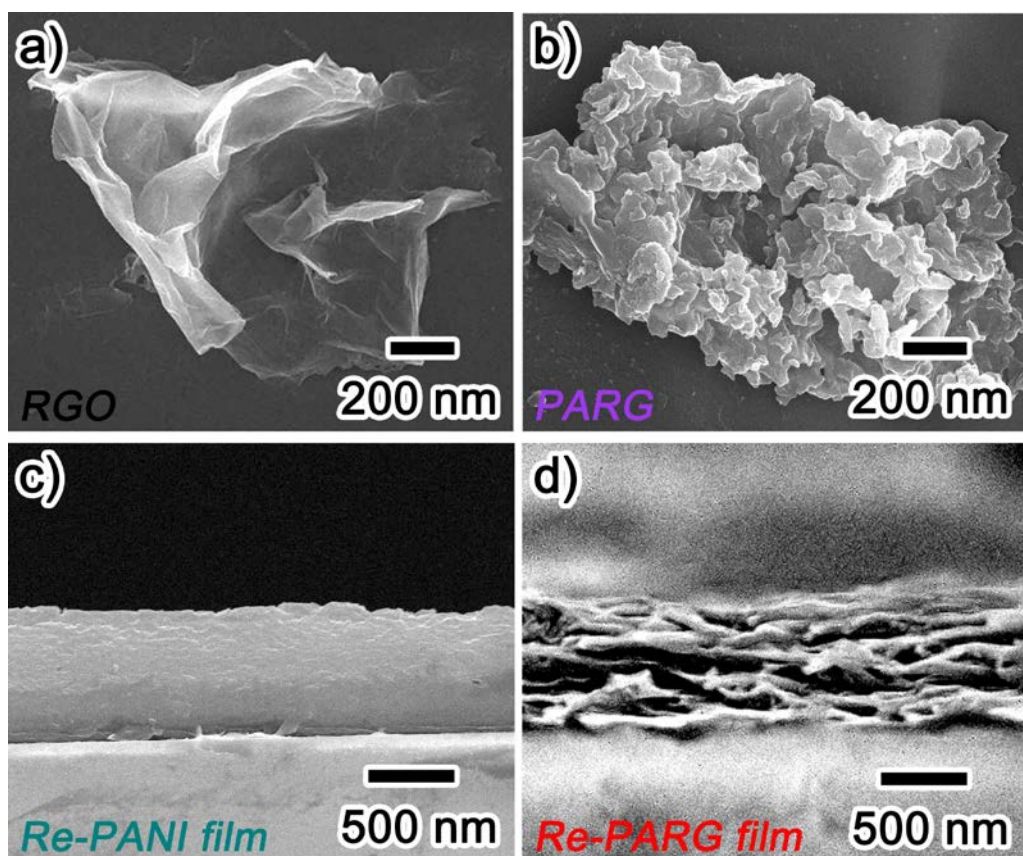


**Figure 23.** SEM images of a) Pristine RGO, b) PARG, c) Cross sectional view of Re-PANI film and d) Re-PARG film.

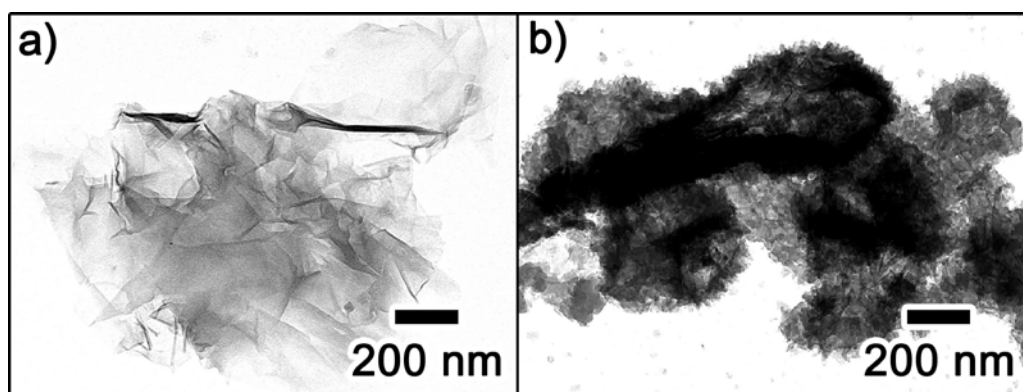


**Figure 24.** TEM images of a) Pristine RGO, b) PARC.

and successfully polymerized on the surface of the few micrometer sized-RGO, which could be beneficial for the homogeneous dispersion of the Re-PARG in the solution. The cross-sectional image of the Re-PARG film (Figure 23d) clearly shows that the RGO components are laterally intercalated with the PANI component, while the Re-PANI film displays a relatively smooth cross-section (Figure 23c). The RGO-intercalated structure of the Re-PARG film is probably attributable to the homogeneous dispersion of the Re-PARG in the solution and the strong  $\pi$ - $\pi$  interactions between the graphitic surface of the RGO and the quinoid rings of the PANI backbone.

Raman spectroscopy was used to analyse the structural changes of the PANI component during de-doping and re-doping processing and to measure the vibrational spectra of nonpolar bonds, such as carbon-carbon interactions between the PANI backbone and the basal planes of RGO. The Raman spectra of the GO, RGO, Re-PARG film, De-PARG, PARG and PANI (ES-state) samples are shown in Figure 25a (the important peaks are marked with black dots). As shown in Figure 25a, structural changes occurred during the chemical processing from GO to RGO in the exfoliation/reduction step and during the transition of PARG to Re-PARG film in the de-doping/re-doping process. Both GO and RGO display two prominent Raman-active peaks at  $1330\text{ cm}^{-1}$

assigned to D mode corresponding to the structural defects and at  $1590\text{ cm}^{-1}$

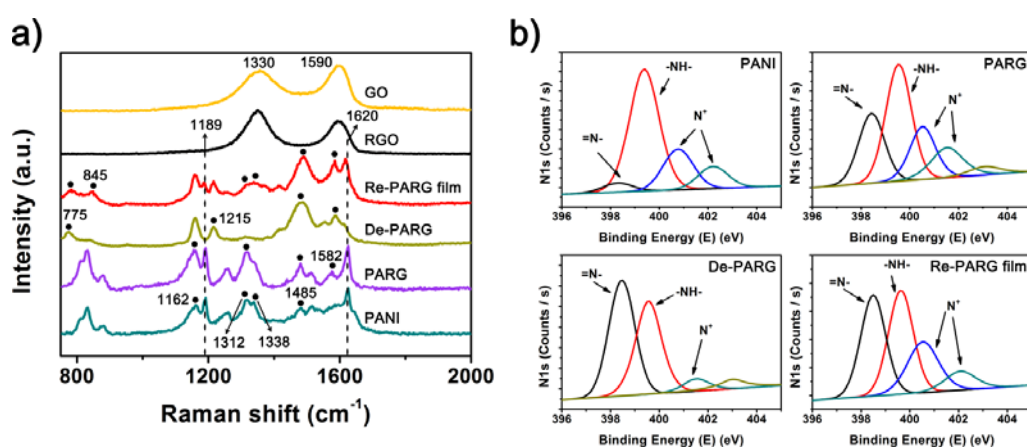


**Figure 25.** a) Raman spectra of GO, RGO, Re-PARG film, De-PARG, PARG and PANI (ES state), b) N 1s XPS spectra of PANI (ES state), PARG, De-PARG and Re-PARG film.

corresponding to the G mode related to the first-order scattering of the  $E_{2g}$  mode observed for  $sp^2$ -carbon domains [69,70]. The Raman spectra of RGO exhibit the increased intensity ratio of the D band to G band ( $I_D/I_G$ ) compared to that of GO, suggesting that the reduction process increased the defect content or edge area in RGO sheets [69]. In addition to the reduction process, the decreased size of the graphene sheets might also cause the structural defect, leading to an increase of  $I_D/I_G$  [59,69]. The Raman spectra of pure PANI show the distinctive vibrations of C-C stretching of the para-distributed benzenoid ring, C=N stretching of the quinoid ring, C=N stretching of the quinoid ring, C-N<sup>+</sup> stretching in polaron form (cationic amine units of the benzenoid ring), C-N<sup>+</sup> stretching in bipolaron form (cationic imine units of the quinoid ring), C-N stretching, C-H bending of the benzenoid ring, C-H bending of the quinoid ring, benzenoid ring deformation, and C-H bending of the quinoid ring and quinoid ring deformation at 1620  $cm^{-1}$ , 1513  $cm^{-1}$ , 1485  $cm^{-1}$ , 1338  $cm^{-1}$ , 1312  $cm^{-1}$ , 1255  $cm^{-1}$ , 1189  $cm^{-1}$ , 1162  $cm^{-1}$ , 878  $cm^{-1}$ , and 832  $cm^{-1}$ , respectively [69,71–75]. These peaks show the coexistence of quinoid and benzenoid structures in PANI ES. After aniline monomers were polymerized on the RGO, the PARG presented four distinguishable peaks that differed from those seen in pure PANI: Increase in the intensity of quinoid ring-related vibrations at 1485, 1312,

and  $1162\text{ cm}^{-1}$  corresponding to the C=N stretching of the quinoid ring, C-N<sup>+</sup> stretching in bipolaron form and C-H bending of the quinoid ring, and appearance of the C=C stretching vibrational mode of the quinoid ring at  $1582\text{ cm}^{-1}$  [73]. These peaks in the PARG probably result from the strong inter-molecular  $\pi$ - $\pi$  stacking, which causes the overlapping of P<sub>z</sub> orbitals between the basal planes of the RGO and the quinoid rings of the PANI backbone [76]. Thus, it can be assumed that the aniline monomers were successfully polymerized on the RGO *via* the strong  $\pi$ - $\pi$  stacking between RGO and PANI. In the Raman spectra of De-PARG, the peaks of C-N<sup>•+</sup> and C-N<sup>+</sup> corresponding to  $1338$  and  $1312\text{ cm}^{-1}$  almost disappeared, whereas the peaks at  $1215$  and  $775\text{ cm}^{-1}$  were newly appeared. The vibrational bands at  $1215$  and  $775\text{ cm}^{-1}$  were attributed to C-N stretching in the EB form of PANI and quinoid ring deformation. [76,77]. Additionally, it was also observed that the peak at  $1620\text{ cm}^{-1}$  corresponding to the C-C stretching of the para-distributed benzenoid ring significantly decreased, while the C=C stretching band of the quinoid ring and the C=N stretching vibration of the quinoid ring, corresponding to  $1582\text{ cm}^{-1}$  and  $1485\text{ cm}^{-1}$ , increased considerably. The EB form of PANI is known to have a higher imine/amine and quinoid ring/benzenoid ring ratio than the ES form [66,69,78–81]. Moreover, it should also be noted that PANI ES significantly losses its bipolaronic and polaronic structure by de-protonation [69,82,83].

Consequently, with the emergence of the new vibration related with the EB form of PANI ( $1215\text{ cm}^{-1}$ ), the observed peaks in De-PARG clearly reveal that the ES-state of PANI on the RGO turned to the EB-state by the de-doping process. After De-PARG was re-doped by CSA, four different features appeared in the spectra of Re-PARG film: (1) Re-emerged bands of the bipolaron and polaron form and C-H bending of the benzenoid ring at  $1310\text{--}1340$  and  $1189\text{ cm}^{-1}$ ; (2) New appearance of an amine deformation peak at  $845\text{ cm}^{-1}$ ; (3) Increase in the intensity of the C-C stretching vibrational mode of the para-distributed benzenoid ring and the C=C stretching band of the quinoid ring at  $1620$  and  $1582\text{ cm}^{-1}$ ; (4) Up-shifted peaks of the C=N stretching of the quinoid ring and quinoid ring deformation at  $1489$  and  $782\text{ cm}^{-1}$  from the peaks at  $1485$  and  $775\text{ cm}^{-1}$ . The re-emerged benzenoid ring peak ( $1189\text{ cm}^{-1}$ ), newly appeared amine deformation peak ( $845\text{ cm}^{-1}$ ), [71] and increased benzenoid ring peak ( $1620\text{ cm}^{-1}$ ) obviously reflect the increased doping level of PANI in the Re-PARG film. Additionally, the re-emerged bipolaron and polaron bands provide crucial evidence of the successful re-protonation of the PANI component in the Re-PARG film. Thus, it can be assumed that the up-shift of the two quinoid ring vibrations at  $782$  and  $1489\text{ cm}^{-1}$  can be attributed to the changed backbone structures of PANI in the Re-PARG film. It is known that the quinoid ring and imine nitrogen atoms in the PANI backbone are substantially converted to



benzenoid ring and amine nitrogen atoms when the EB state of the PANI turns to the ES state. [66,79,80] However, the quinoid ring vibrations at 1582, 1489, 1162 and 782  $\text{cm}^{-1}$  did not disappear even after the re-doping process, but dominated the overall Raman spectrum of the Re-PARG film. Furthermore, the peak at 1582  $\text{cm}^{-1}$  corresponding to the C=C stretching band of the quinoid ring was slightly increased. As described above, the graphitic surface of the RGO interacts strongly with the quinoid ring of the PANI through the  $\pi$ - $\pi$  stacking. Consequently, the overlapping of the  $P_z$  orbitals of the quinoid rings of the PANI with the aromatic surface of RGO would result in the strong quinoid ring peaks in the Re-PARG film.

XPS analysis was also conducted to investigate the structural change of PANI in the de-doping/re-doping process and the specific interaction between RGO and the PANI backbone (Figure 25b). In this study, N1s spectra of PANI (ES state), PARG, De-PARG and Re-PARG film samples were collected. In the N1s spectra of PANI sample, the peak at 398.5 eV (black line) corresponds to quinoid imine (-N=), and the more prominent peak at 399.5 eV (red line) corresponds to benzenoid amine (-NH-) in the PANI backbone [84,85]. An additional two minor peaks at 400.8 eV and 402.2 eV (blue and dark cyan lines) correspond to positively charged imine in the bipolaron state and protonated amine in the polaron state [86,87]. These spectra demonstrate the

typical structure of the PANI in ES form.

After the polymerization of PANI on RGO, some structural changes were observed in the PARG. Increased XPS peak signal area of the quinoid imine peak at 398.4 eV, from 0.38 % of the overall PANI signal area to 1.57 % of the PARG signal area, was observed. The peak at 400.5 eV, which represents charged imine, is also slightly increased. The strong  $\pi$ - $\pi$  stacking between the PANI backbone and RGO might have caused an increase in the quinoid imine peaks.

The N1s spectra of De-PARG sample shows increased peak at 398.5 eV and diminished peak at 399.5 eV, which correspond to quinoid imine and benzenoid amine in the backbone, while only one minor peak at 401.5 eV for the protonated amine part [69] is shown. Increased imine peak is due to the ammonium hydroxide addition and following de-protonation of amine in the PANI ES backbone [66,69,78–81]. Additionally, when the ES form of PANI changed to the EB form, it possessed almost no charge in the backbone [69,82,83], resulting in the disappearance of the positively charged imine peak at 400.5 eV and the attenuated peak of protonated amine at 401.5 eV.

After De-PARG was re-doped by CSA, the XPS analysis on the Re-PARG film suggests that the charged bipolaron structure (re-emerged blue peak at 400.5 eV) and polaron structure (increased dark cyan peak at 402.2 eV) were

restored. Thus, it could be assumed that the ES form of the PANI backbone was successfully re-established [82,88]. The re-doping of the EB state of PANI is known to induce a substantial transition of imine nitrogen atoms to amine nitrogen atoms in the PANI backbone [66,79,80]. However, the quinoid imine (-N=) peak at 398.5 eV considerably remained even after the re-doping process. Therefore, this result suggests that the specific  $\pi$ - $\pi$  interaction between the quinoid ring of the PANI and the graphitic surface of the RGO exists and the interaction leads to preservation of the quinoid imine structure in the Re-PARG sample, which is in accordance with the previous Raman analysis.

As described above, it has been found that PANI chains re-doped by CSA could change their molecular conformation possessing the mobility with its counter-ion in the *m*-Cresol/chloroform co-solutions [66]. Additionally, it is known that when the interaction between polymer and solvent is larger than the interaction between polymer and polymer, more linear polymer chain conformation is preferred due to the increased possibility that the polymer chains will interact with the solvent [66]. Thus, considering these facts, it is expected that the strong interaction between the PANI and RGO ( $\pi$ - $\pi$  interaction) effectively helps PANI chains possess the more linear conformation, leading to increased crystallinity along with improved electrical conductivity. In the next step, we measure the electrical conductivity and

crystalline structure of the films to achieve an in-depth insight into the role of the RGO in determining the conformation of PANI chains and overall crystalline structure and electrical conductivity of the films.

In order to elucidate the role of the RGO in determining the electrical properties and crystalline structure of the composite film, the De-PARG samples (De-PARG 1-3) were first prepared with various mass ratio of De-PANI to RGO. The prepared De-PARG 1-3 samples were used in producing the Re-PARG 1-3 films without any weight ratio change of either component. TGA was performed to assess the precise weight percentages of the PANI component in the De-PARG 1-3 samples under air flow at a heating rate of  $10\text{ }^{\circ}\text{C min}^{-1}$  (Detailed description in Figure 26). Based on these TGA data, the weight percentage of PANI component was calculated as 88, 76 and, 60 % for De-PARG 1, 2, and 3, respectively. The four-probe method was conducted to measure the electrical conductivity of the samples. The Re-PANI film and RGO were prepared as control materials. Figure 27a presents the electrical conductivities of the Re-PARG films and control samples. The electrical conductivities of Re-PANI film, Re-PARG 1 film, Re-PARG 2 film, Re-PARG 3 film, and RGO were measured as *ca.* 580, 762, 906, 298, and  $46.5\text{ S cm}^{-1}$ , respectively. Starting from the Re-PANI film, the electrical conductivity of the film increased to the maximum of  $906\text{ S cm}^{-1}$  (Re-PARG 2 film) as the weight

percentage of the RGO increased to 24 %, while decreased value of

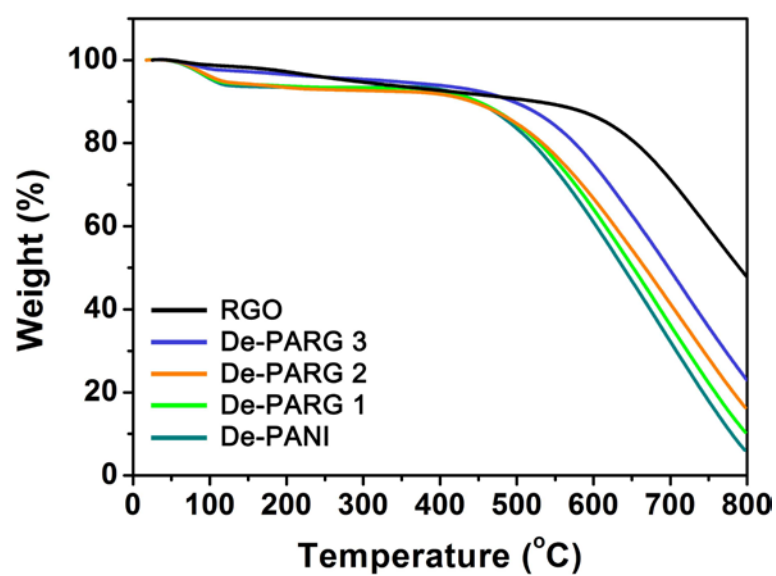


**Figure 26.** TGA curves of RGO, De-PARG 1-3 composites with different weight percentage of De-PANI, and De-PANI.

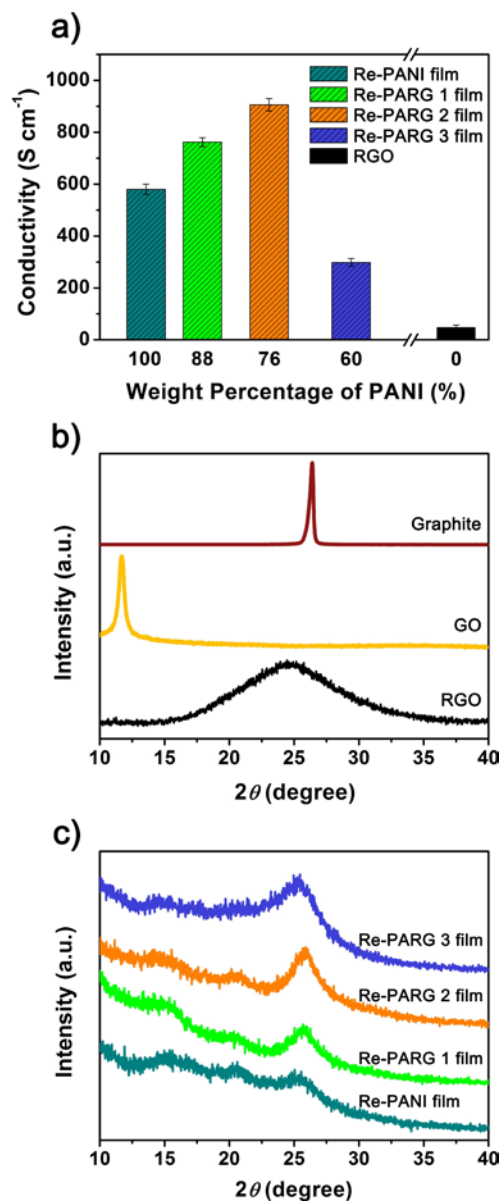


**Figure 27.** a) Electrical conductivity of Re-PANI film, Re-PARG 1-3 films, and RGO displayed as function of the weight percentage of PANI component; b) XRD patterns of graphite, GO, and RGO; c) XRD patterns of Re-PARG 1-3

films and Re-PANI film.

conductivity was measured in Re-PARG 3 film. Additional TGA and XRD analysis were conducted to measure the remaining solvent in the film and ascertain the effect of the solvent evaporation on the electrical performance of the film over time. The as-prepared Re-PARG 2 film and Re-PARG 2 film after keeping for 150 days were used in both TGA and XRD analysis and the Re-PARG 2 powder before mixing with m-cresol and chloroform was used as a control in TGA test (Detailed description in Figure 28). The weight percentage of the as-prepared Re-PARG 2 film and the Re-PARG 2 film after keeping for 150 days were measured to be as *ca.* 1.25 wt % and *ca.* 0 wt %, indicating that negligible amount of solvent was remained on the film after annealing process and solvent evaporation is occurred with time. The XRD analysis illustrates that enhanced crystalline structure of the film was maintained even after storing for 150 days. Therefore, it is considered that crystalline structure was not affected by solvent evaporation and performance of the material is well maintained over time.

Figure 27b shows the XRD patterns of the graphite, GO and RGO. The XRD pattern of graphite presented a typical (002) narrow peak [89] at  $2\theta = 26.5^\circ$ , corresponding to a d-spacing of *ca.* 3.36Å. In the case of GO, a sharp diffraction peak was observed at  $2\theta = 11.65^\circ$  (d-spacing = *ca.* 7.59Å), which

can be assigned to the (001) reflection peak [59]. The increase in the interlayer

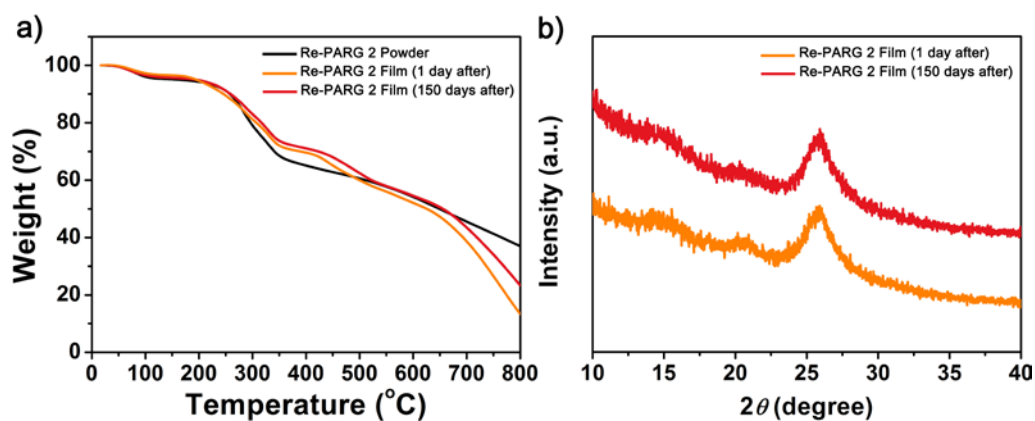


**Figure 28.** a) TGA curves of Re-PARG 2 powder, as-prepared Re-PARG 2 film and Re-PARG 2 film after storing for 150 days and b) XRD patterns of as-prepared Re-PARG 2 film and Re-PARG 2 film after storing for 150 days.



distance from *ca.* 3.36 Å for graphite to *ca.* 7.59 Å for GO reflects successful oxidation of graphite [70]. After ultra-sonication and reduction steps, the (001) reflection peak of GO disappeared, and one broad peak centered at 24.58° (d-spacing = *ca.* 3.62Å) appeared in the XRD spectra of RGO, illustrating that the GO was efficiently reduced into RGO [64].

Figure 27c represents the XRD patterns of Re-PARG 1-3 films and Re-PANI film. The Re- PANI film shows three peaks centered at  $2\theta = 15.3^\circ$ ,  $20.5^\circ$ , and  $25.6^\circ$  (d-spacings= *ca.* 5.8, 4.3, and 3.5 Å) on the broad background, revealing the semi-crystalline nature of the PANI. By increasing the weight percentage of RGO from 0 % (Re-PANI film) to *ca.* 12 % (Re-PARG 1 film), the peaks at  $15.3^\circ$  and  $20.5^\circ$  decreased along with the decrease in the broad background, whereas the peak at  $25.6^\circ$  increased. When the weight percentage of RGO reached 24 % (Re-PARG 2 film), with the maximum electrical conductivity ( $906 \text{ S cm}^{-1}$ ) among the films, the peaks at  $15.3^\circ$ ,  $20.4^\circ$  and the broad background mostly disappeared and the diffraction pattern of the Re-PARG 2 film was dominated by the peak at  $25.6^\circ$ . This indicates an increase in the crystalline phase of the film and strengthened stacking along the specific direction. More specifically, these results have following three implications. First, the disappearance of the intrinsic peak of RGO ( $24.58^\circ$ ) in the XRD

patterns of the Re-PARG 1 and 2 films clearly indicates that the RGO is properly intercalated into PANI chains. Second, it is known that the d-spacing of *ca.* 3.5 Å (25.6°) is the face-to-face  $\pi$ - $\pi$  stacking distance between neighboring phenyl rings in the crystalline structure of the PANI [17,90]. Thus, the increase in the intensity of the peak at 25.6° along with the decrease in the intensity of the peaks at 15.3°, 20.5° and the broad background reflect that  $\pi$ - $\pi$  inter-chain stacking between the phenyl rings of the PANI chains was intensified. Third, based on the strengthened peak (25.6°) of the Re-PARG 1 and 2 films with the increase of RGO contents, it is considered that the basal planes of RGO and phenyl rings also form  $\pi$ - $\pi$  stacking with a distance of 3.5 Å. Considering these results, the mechanism of improved electrical conductivity of Re-PARG 1 and 2 films could be explained in the following manner: The chemical structure of the micro-meter sized RGO consists of a number of aromatic rings. Thus, when PANI and RGO co-exist in the solution, it is expected that the PANI chains would strongly interact with the aromatic structure of RGO by the  $\pi$ - $\pi$  overlapping of the basal planes of the RGO and the quinoid rings of the PANI, resulting in more expanded coil conformation of the PANI chains. Then, the PANI chains expanded by the RGO would induce more planar stacking with nearby PANI chains sequentially. In this way, the PANI chains would form the more planar chain conformation and compact

packing structure. This compact packing of PANI chains would inhibit the considerable ring rotations ( $\pi$ -conjugation defects) of the phenyl rings from the plane of the backbone, leading to the improved  $\pi$ - $\pi$  interactions, extensive three-dimensional delocalization of charge, and increase in the crystallinity and electrical conductivity [66,88]. This compact crystalline structure of PANI chains with RGO is proposed as a pictorial scheme in Figure 29 where PANI chains are located between RGO.

However, as the weight percentage of RGO further increase to 40 % in the Re-PARG 3 film, the XRD pattern showed an increase in broad background, re-emerged peaks at  $15.3^\circ$  and  $20.5^\circ$ , and a weak change in peak intensity at  $25.6^\circ$ . This indicates that an overall decrease in the crystallinity of the film has occurred, and the PANI chains are not aligned in one direction after the specific weight percentage of RGO (40%). Based on the highly disordered crystalline structure of the pristine RGO (Figure 27b), the increase in the amorphous region in the Re-PARG 3 film is considered as a result of the increased influence of the poorly ordered structure of the RGO. This increase in the amorphous region of the film would result in a shorter mean free path and worsened carrier transport, leading to the decrease in the electrical conductivity of the film [23,90]. Consequently, the XRD analysis demonstrates that RGO in the composite favorably or unfavorably changes the crystalline structure of

PANI depending on PANI/RGO weight ratios, leading to the increase or

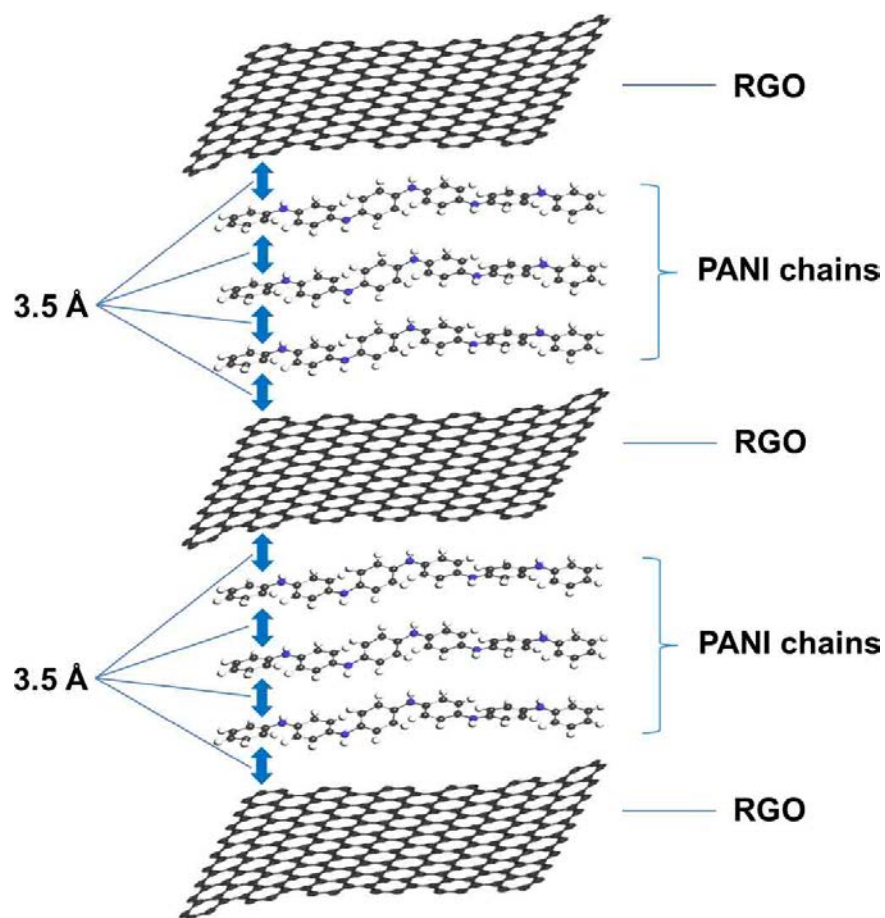


**Figure 29.** Schematic representation of interaction between RGO and PANI chains leading to compact packing of the PANI chains with RGO and extensive three-dimensional delocalization of the charge.

decrease in the electrical conductivities of PANI/RGO hybrid films. Most interesting part of XRD analysis is that the strong  $\pi$ - $\pi$  interactions of RGO with the quinoid rings of the PANI chains increase the electrical conductivity and crystallinity of the PANI/RGO hybrid film, which is greater than both RGO and PANI. To investigate the advantages of enhanced electrical conductivity and crystallinity of Re-PARG film as a supercapacitor electrode, electrochemical analysis was performed to the Re-PARG 2 film.

### **3.3.2. Flexible supercapacitor based on PANI/RGO film**

CV and galvanostatic charge/discharge analysis were conducted in 1 M  $\text{H}_2\text{SO}_4$  electrolyte with three-electrode system to evaluate electrode performance. For a comparison, the Re-PANI film and pristine RGO were also used as electrodes for supercapacitor. Figure 30a illustrates the CV curves of the Re-PARG film, Re-PANI film and RGO at a scan rate of  $5 \text{ mV s}^{-1}$  from 0 to 0.8 V. The CV curve of RGO shows the rectangular shape without any redox peaks, reflecting the good charge propagation and EDL capacitance of the carbon materials [40,64,69]. On the contrary, two pairs of broad redox peaks were observed for the Re-PARG and Re-PANI films, revealing the existence of the pseudo-capacitive PANI component in the Re-PARG film. [69]. The two observed redox peaks originated from its redox transitions between the

leucoemeraldine form (semiconducting state), the ES form (conducting state)

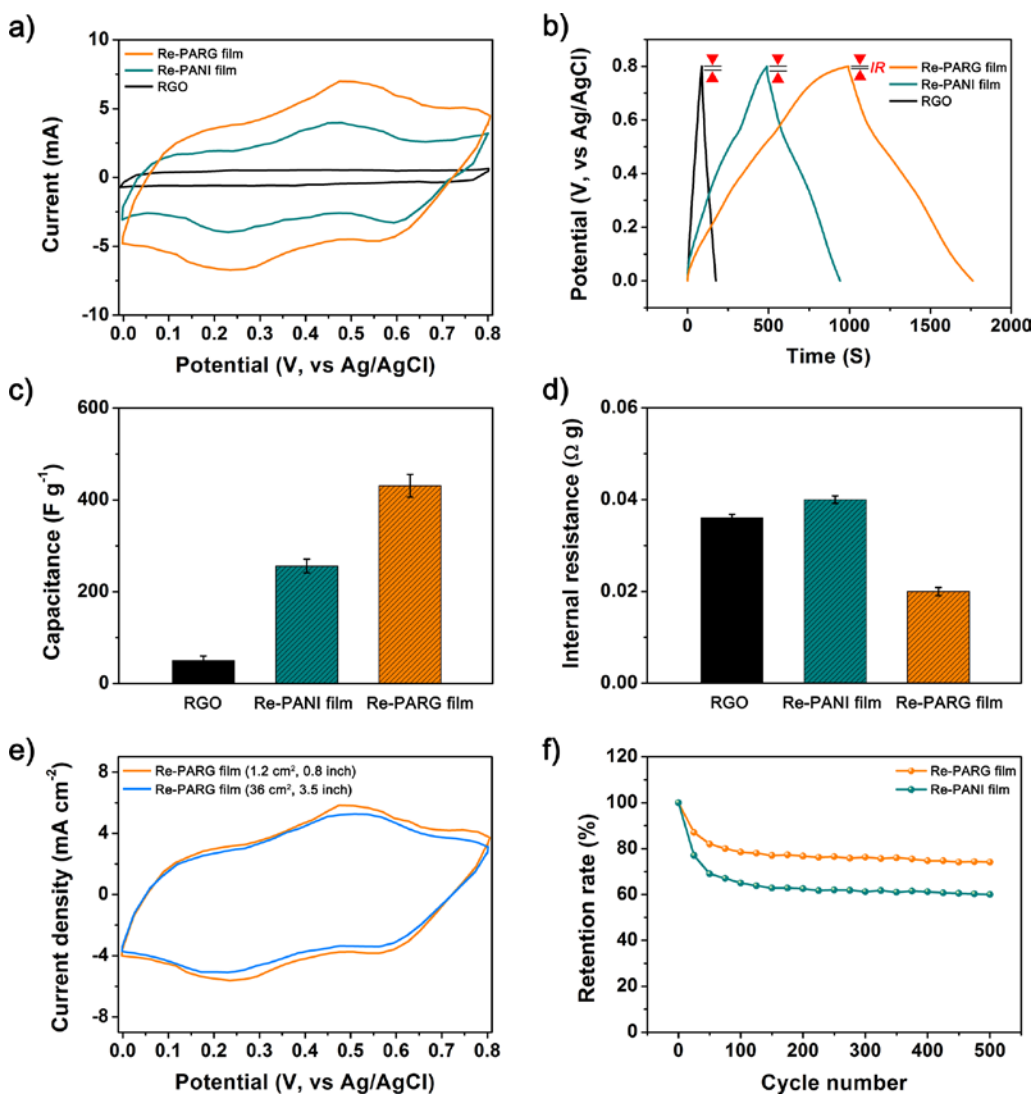


**Figure 30.** a) CV curves of Re-PARG film, Re-PANI film and RGO electrodes at a scan rate of  $5\ mV\ s^{-1}$  between 0 and 0.8 V in 1M  $H_2SO_4$  solution; b) Galvanostatic charge/discharge curves of Re-PARG film, Re-PANI film and

RGO electrodes at current density of  $0.45 \text{ A g}^{-1}$  in  $1\text{M H}_2\text{SO}_4$  solution; c) Gravimetric capacitances of RGO, Re-PANI film and Re-PARG film electrodes at current density of  $0.45 \text{ A g}^{-1}$ ; d) Internal resistances of RGO, Re-PANI film and Re-PARG film electrodes estimated from the IR drop at a current density of  $0.45 \text{ A g}^{-1}$ ; e) Comparison of CV curves between different sized ( $1.2$  and  $36 \text{ cm}^2$ ) Re-PARG film electrodes at a scan rate of  $5 \text{ mV s}^{-1}$ ; f) Cyclic stability of Re-PARG film and Re-PANI film electrodes as a function of cycle number at a current density of  $0.45 \text{ A g}^{-1}$ .

and the Faradic transformation of emeraldine/permanganine [59,64,90]. Additionally, the CV curve of the Re-PARG film showed the largest CV loop area with the highest current response, demonstrating the larger specific capacitance of the Re-PARG film than the RGO and the Re-PANI film [40,91]. This phenomenon suggests that the RGO in the Re-PARG film is a crucial factor for enhanced capacitance compared with that of the RGO and the Re-PANI film.

To further elucidate the electrochemical behavior of the Re-PARG film, Re-PANI film and RGO, the galvanostatic charge/discharge test was carried out at a current density of  $0.45 \text{ Ag}^{-1}$  from 0 to 0.8 V in 1M  $\text{H}_2\text{SO}_4$  electrolyte. As shown in Figure 30b, the galvanostatic charge/discharge curve of the RGO exhibits a symmetric triangular shape, indicating that its capacitance originates from the EDL capacitance, [42] as described above. In contrast, the discharge curve of the Re-PARG film exhibits two distinct voltage stages: *ca.* 0.8–0.6 V and *ca.* 0.6–0 V, respectively. The first stage, with a relatively short discharging duration, is attributed to EDL capacitance, whereas the second stage, with a much longer discharging duration, is due to the combination of EDL and faradaic capacitances of the PANI component in the film [42]. The discharge curve of the Re-PANI film also represents a shape similar to that of



the Re-PARG film. However, the Re-PARG film exhibits a much longer discharging time and less vertical voltage drop at the beginning of the discharge curve than the Re-PANI film, indicating that the Re-PARG film possesses much higher specific capacitance and smaller internal resistance than the Re-PANI film [90,92]. Possessing low internal resistance as a supercapacitor is a crucial factor for improving the capacitance of the materials and reducing unwanted power consumption [68,93].

The precise gravimetric capacitances (Figure 30c) and internal resistances (Figure 30d) of all samples were calculated from the galvanostatic discharge curves [64,94] and vertical voltage drop at the initial point of each discharge curve [90] (Detailed description in experimental section). The RGO, Re-PANI film, and Re-PARG film exhibit the gravimetric capacitances of 50, 256, and 431 F g<sup>-1</sup> and internal resistances of 0.036, 0.04, and 0.02 Ω g, respectively. The Re-PARG film and the Re-PANI film show much higher gravimetric capacitances than the RGO electrode. Generally, pseudo-capacitance is much higher than EDL capacitance, because pseudo-capacitive materials take advantage of fast redox reactions by utilizing whole mass [1,95–97]. Thus, though the RGO displays lower internal resistance than the Re-PANI film electrode, the RGO illustrates the lowest gravimetric capacitance among all the samples due to the absence of pseudo-capacitive materials [42]. Interestingly,

without any specific nanostructure, the Re-PANI film shows a relatively small internal resistance and a high gravimetric capacitance. This high gravimetric capacitance and low internal resistance of the Re-PANI film are perhaps due to its high electrical conductivity, [40,98] which is one of the highest among those reported in the literature [16,23,40]. Notably, when the PANI component is incorporated with the RGO in film form, the Re-PARG film exhibits the highest gravimetric capacitance and the lowest internal resistance among all the samples, indicating the synergistic effect of PANI and RGO. This effect originates from the following two factors: (1) the combining effect of the EDL and faradaic capacitances, [92,93] in agreement with the two voltage stages of *ca.* 0.8–0.6 V and 0.6–0 V and (2) the extremely high electrical conductivity [40] from improved conducting networks of PANI chains by the RGO and the strong  $\pi$ – $\pi$  interactions between the RGO and the PANI chains. PANI, in its leucoemeraldine or pernigraniline form, is an insulator; accordingly, the supercapacitors possessing the PANI component suffer from large internal resistance, as it is close to the fully charged or discharged state [42,59,64,90]. However, the Re-PARG film possesses the RGO component, which could act as a good current collector, and the strong  $\pi$ – $\pi$  interactions between the RGO and the PANI chains in the Re-PARG film could provide a good conducting network even though PANI is close to the insulating form,

which facilitates the redox reaction of PANI and leads to the increase in the pseudo-capacitance [40,42,94]. Concurrently, the Re-PARG film with enhanced conducting networks decrease the internal resistance, leading to the improvement in effective energy storage by reducing the energy consumption caused by internal resistance [93].

The CV test was also performed on the Re-PARG film of two different sizes in 1M H<sub>2</sub>SO<sub>4</sub> at a scan rate of 5 mV s<sup>-1</sup> (Figure 30e). The size of one film (36 cm<sup>2</sup>, 3.5 inch) was 30 times larger than that of the other one (1.2 cm<sup>2</sup>, 0.8 inch). Both films were light-weight (2 and 60 mg) and thin (14.5 μm). Remarkably, even after the size of the film was increased 30 times, the larger sized film demonstrated an area capacitance of 0.655 F cm<sup>-2</sup> (393 F g<sup>-1</sup>), which is only 9 % smaller than that of the smaller sized film (0.718 F cm<sup>-2</sup>, 431 F g<sup>-1</sup>), suggesting a promising electrochemical property for large-scale supercapacitors.

The typical poor long-term stability of supercapacitors based on the CPs during cycling is one of the greatest obstacles in producing low-cost electrode materials for commercially available supercapacitors [46]. As shown in Figure 30f, the Re-PANI film shows a rapid initial drop on capacitance retention and maintains 60 % of initial gravimetric capacitance (from 256 to 153 F g<sup>-1</sup>) after 500 charging/discharging cycles at a current density of 0.45 A g<sup>-1</sup> because

PANI suffers from swelling and shrinkage during charging/discharging cycling [42,46,64,93]. The capacitance retention of the Re-PARG film also displays a rapid initial drop due to the large portion of PANI component (76 wt %) in the Re-PARG film. However, in the case of the Re-PARG film, it exhibits improved capacitance retention of 74 % (from 431 to 318 F g<sup>-1</sup>) after 500 charging/discharging cycles under the same conditions, due to suppression of the shrinking and swelling of the PANI chains by the mechanically strong RGO [94]. In addition to the enhanced mechanical property of the film by RGO, the enhanced cycling stability of the film is probably attributed to the increased electrical conductivity of the Re-PARG film. It is known that low electrical conductivity of a device causes the large resistance and joule heating while the device is working, which substantially diminishes the life of the organic device [23]. Therefore, for the Re-PARG film, increased electrical conductivity would lead to the improved cycling stability of the film by reducing the large resistance and joule heating of the electrode during the charging/discharging cycling. To obtain the film with less initial drops on capacitance retention and more enhanced capacitance retention, following method could be used in current PANI-graphene composite system. It has been reported that improvement in mechanical properties of graphene (e.g., from graphene oxide to reduced graphene oxide) could increase the retention rate of

PANI-graphene composite by enhancing the restraint of shrinkage and swelling of PANI chains during charging/discharging processes [69]. From this point of view, possible improvement can be realized by using mechanically stronger single-layer graphene sheet (e.g., fabricated by chemical vapor deposition or arc-discharge method) [70,99] or graphene nanoribbon [100] than RGO prepared by Hummers' method. The enhanced mechanical resilience by mechanically stronger graphene sheet or graphene nanoribbon might result in cycling performance improvement with the enhanced electrical conductivity and crystallinity due to the  $\pi$ - $\pi$  stacking between PANI structure and graphitic surface of single-graphene sheet or graphene nanoribbon. Using this method, the cyclability of the PANI-RGO system electrode can probably be increased even in long cycles. Finally, all of these results suggest the great potential of the PANI/RGO film to be used as an electrode material for high-performance scalable supercapacitors.

Figure 31a depicts the great flexibility of the Re-PARG film, which can endure bending, twisting, and even folding without any destruction. This high flexibility of the Re-PARG film is attributed to the inherent flexibility of the CPs [23,40,101,102]. Additionally, in order to test the supercapacitor performance of the Re-PARG film under bending conditions, the CV test was also performed on the films with two different bending angles of  $0^\circ$  and  $180^\circ$  at

a scan rate of  $5 \text{ mV s}^{-1}$ . As shown in Figure 31b, the Re-PARG films represent

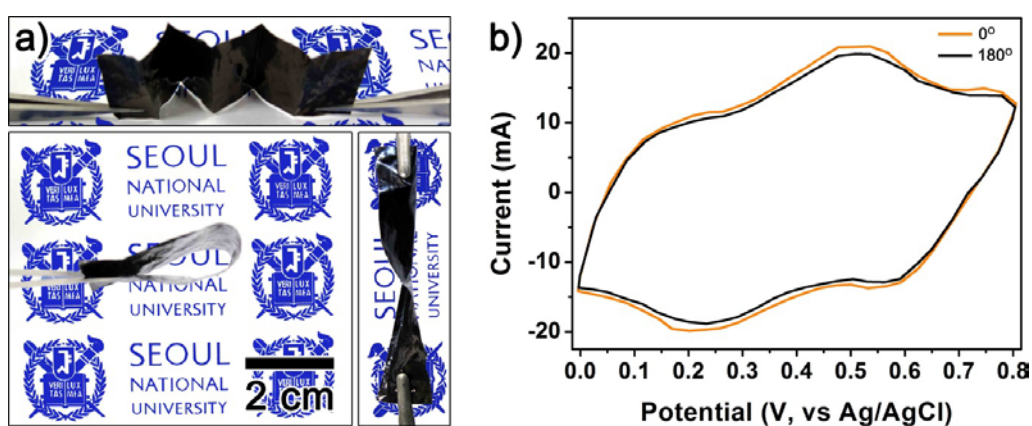


**Figure 31.** a) Digital photographs of flexible Re-PARG film. The top image exhibits the folding characteristics of the film. The bottom images illustrate the high flexibility (bending and twisting) of the film; b) CV curves of Re-PARG film electrodes with two different bending angles of  $0^\circ$  and  $180^\circ$  at a scan rate of  $5 \text{ mV s}^{-1}$ .

the non-substantial difference between the CV curves with bending angles of  $0^\circ$  and  $180^\circ$ , indicating the superior performance ability of the Re-PARG film as a flexible supercapacitor. Therefore, the Re-PARG film can potentially be applied in producing flexible electronic equipment such as bendable displays, intelligent clothes, and various flexible devices.

#### 4. CONCLUSIONS

1. Highly conductive PANI/SiO<sub>2</sub> nanocomposites with large surface area have been made using the SSDP method. The diameter of the nanocomposites were controlled from 18 nm to 130 nm by varying the size of the SiO<sub>2</sub> NPs. As the diameter of the PANI/SiO<sub>2</sub> nanocomposite decreased (from 130 to 18 nm), the electrical conductivity increased (from 16.4 to 25.6 S cm<sup>-1</sup>). When applied as electrode materials for supercapacitors, PANI/SiO<sub>2</sub> nanocomposite prepared by SSDP method exhibited improved specific capacitance (*ca.* 305 F g<sup>-1</sup>) and cycle-life performance (72 % after 500 cycles) compared to PANI/SiO<sub>2</sub> nanocomposite (*ca.* 112 F g<sup>-1</sup> and 60 % after 500 cycles) synthesized by conventional polymerization method. The high conductivity and large surface area facilitated the charge/discharge of PANI, and the increased crystalline structure of PANI prevented severe deterioration of the polymer structure. The highly conductive and crystalline PANI/SiO<sub>2</sub> nanocomposite prepared by SSDP can be used in various applications, such as batteries, sensors, actuators, corrosion protection, electro-optics, electro-chromic devices, and dye-sensitized solar cells.
2. PANI/MoS<sub>2</sub> nanocomposite has been prepared using SSDP and electrical and electrochemical properties of PANI/MoS<sub>2</sub> nanocomposite have been



revealed. Produced PANI/MoS<sub>2</sub> nanocomposite demonstrated remarkably high electrical conductivity of *ca.* 28.6 S cm<sup>-1</sup>. In the electrochemical tests, PANI/MoS<sub>2</sub> nanocomposite demonstrated high capacitance of *ca.* 400 F g<sup>-1</sup> and good cycling stability (84 % after 500 cycles). All these results suggest great potential of the PANI/MoS<sub>2</sub> nanocomposite as practical supercapacitor electrode.

3. Flexible PANI/RGO film was successfully fabricated through solution processing. The strong  $\pi$ - $\pi$  interactions of RGO with the quinoid rings of the PANI chains in the solution induced the more expanded conformation of the PANI chains, leading to the extremely high electrical conductivity of the film (*ca.* 906 S cm<sup>-1</sup>) (greater than the pristine PANI film :*ca.* 580 S cm<sup>-1</sup>) and RGO (*ca.* 45.6 S cm<sup>-1</sup>)). Additionally, the film demonstrated the high capacitance of *ca.* 431 F g<sup>-1</sup> and enhanced cycling stability (74 % after after 500 cycles) in comparison with pure PANI film (*ca.* 256 F g<sup>-1</sup> and 60 % after 500 cycles). The PANI/RGO film also demonstrated excellent performance ability as a scalable and flexible electrode material for high-performance supercapacitors with various film sizes and even under bending conditions. This approach will offer a valuable and promising tool for producing highly flexible, scalable, and high-performance supercapacitor electrodes.

In summary, three different PANI/organic • inorganic composites were prepared *via* SSDP method with considering five conditions for producing a high-performance supercapacitor to achieve supercapacitors with high capacitance and good electrochemical stability. First, PANI/SiO<sub>2</sub> nanocomposite was fabricated by SSDP method. Produced PANI/SiO<sub>2</sub> nanocomposite exhibited enhanced electrochemical performances (specific capacitance: *ca.* 305 F g<sup>-1</sup>, cycling stability: maintaining 72 % of initial gravimetric capacitance after 500 cycles) compared with PANI/SiO<sub>2</sub> nanocomposite prepared by conventional polymerization method and other previously reported PANI owing to high electrical conductivity (*ca.* 25.6 S cm<sup>-1</sup>), large specific surface area (*ca.* 170 m<sup>2</sup> g<sup>-1</sup>), and improved crystallinity. Second, PANI/MoS<sub>2</sub> nanocomposite, synthesized by SSDP method, showed improved specific capacitance (*ca.* 400 F g<sup>-1</sup>) in comparison with both PANI (*ca.* 232 F g<sup>-1</sup>) and MoS<sub>2</sub> nanosheet (*ca.* 3 F g<sup>-1</sup>) due to high electrical conductivity (*ca.* 28.6 S cm<sup>-1</sup>) and pseudo capacitive characteristics of PANI and MoS<sub>2</sub>. Additionally, PANI/MoS<sub>2</sub> nanosheet exhibited enhanced cycling stability (84 % after 500 cycles) compared with pristine PANI (62 % after 500 cycles) due to honeycomb-like structured PANI on MoS<sub>2</sub> nanosheet and incorporation of MoS<sub>2</sub> nanosheet possessing good mechanical properties. Lastly, flexible PANI/RGO film was fabricated through solution processing.

Produced PANI/RGO film exhibited extremely high electrical conductivity of *ca.*  $906 \text{ S cm}^{-1}$  due to improved crystallinity. In the electrochemical tests, PANI/RGO film exhibited enhanced capacitance (*ca.*  $431 \text{ F g}^{-1}$ ) and cycling stability (74 % after after 500 cycles) compare with pristine PANI film (specific capacitance: *ca.*  $256 \text{ F g}^{-1}$ , cycling stability: 60 % after 500 cycles). The PANI/RGO film also demonstrated excellent performance ability as a scalable and flexible electrode material. The strategies and specific synthetic methods described here can be useful tool for fabricating supercapacitor electrodes with high capacitance and good electrochemical stability.

## REFERENCES

- [1] P. Simon, Y. Gogotsi, *Nat. Mater.*, **2008**, 7, 845.
- [2] M. Huang, F. Li, F. Dong, Y. X. Zhang, L. L. Zhang, *J. Mater. Chem. A*, DOI: 10.1039/C5TA05523G.
- [3] M. Kim, C. Lee, J. Jang, *Adv. Funct. Mater.*, **2014**, 24, 2489.
- [4] S. Cho, M. Kim, J. Jang, *ACS Appl. Mater. Interfaces*, **2015**, 7, 10213.
- [5] J. Jun, J. S. Lee, D. H. Shin, S. G. Kim, J. Jang, *Nanoscale*, **2015**, 7, 16026.
- [6] J. S. Lee, D. H. Shin, J. Jang, *Energy Environ. Sci.*, **2015**, 8, 3030.
- [7] E. Song, J.-W. Choi, *Nanomaterials*, **2013**, 3, 498.
- [8] J. Huang, R. B. Kaner, *Angew. Chem.*, **2004**, 116, 5941.
- [9] J. Jang, J. Ha, J. Cho, *Adv. Mater.*, **2007**, 19, 1772.
- [10] S. Cho, O. S. Kwon, S. A. You, J. Jang, *J. Mater. Chem. A*, **2013**, 1, 5679.
- [11] A. G. Macdiarmid, *Angew. Chem. Int. Ed.*, **2001**, 40, 2581.
- [12] K. Matyjaszewski, Oxidative polymerization. In *Encyclopedia of polymer science and technology*. H. Higashimura, S. Kobayashi, 4th ed., John Wiley & Sons, Inc.: New York, 2004, pp 740–764.
- [13] J. Jang, *Adv. Polym. Sci.*, **2006**, 199, 189.
- [14] H. Bai, G. Shi, *Sensors*, **2007**, 7, 267.

- [15] S. Bhadra, D. Khastgir, N. K. Singha, J. H. Lee, *Prog. Polym. Sci.*, **2009**, *34*, 783.
- [16] S. Lee, D. Lee, K. Lee, C. Lee, *Adv. Funct. Mater.*, **2005**, *15*, 1495.
- [17] K. Lee, S. Cho, S. H. Park, A. J. Heeger, C.-W. Lee, S.-H. Lee, *Nature*, **2006**, *441*, 65.
- [18] P. D. McNaughter, J. C. Bear, D. C. Steytler, A. G. Mayes, T. Nann, *Angew. Chem. Int. Ed.*, **2011**, *50*, 10384.
- [19] E. E. Lees, T. L. Nguyen, A. H. A. Clayton, P. Mulvaney, *ACS Nano*, **2009**, *3*, 1121.
- [20] J. Jang, J. Ha, B. Lim, *Chem. Commun.*, **2006**, 1622.
- [21] H. Tadokoro, S. Seki, I. Nitta, *Bull. Chem. Soc. Jpn.*, **1995**, *28*, 559.
- [22] E. Dmitrieva, L. Dunsch, *J. Phys. Chem. B*, **2011**, *115*, 6401.
- [23] B. H. Lee, S. H. Park, H. Back, K. Lee, *Adv. Funct. Mater.*, **2011**, *21*, 487.
- [24] K. Lee, in *Encyclopedia of Nanoscience and Nanotechnology* (Ed: Nalwa, H. S.), American Scientific Publications, San Diego, CA 2003.
- [25] J. Tsukamoto, *Adv. Phys.*, **1992**, *41*, 509.
- [26] M. Yamaura, K. Sato, T. Hagiwara, K. Iwata, *Synth. Met.*, **1992**, *48*, 337.
- [27] Y. Nogami, J. P. Pouget, T. Ishiguro, *Synth. Met.*, **1994**, *62*, 257.

- [28] J. Joo, Z. Oblakowski, G. Du, J. P. Pouget, E. J. Oh, J. M. Wiesinger, Y. Min, A. G. MacDiarmid, A. J. Epstein, *Phys. Rev. B*, **1994**, *49*, 2977.
- [29] J. P. Pouget, Z. Oblakowski, Y. Nogami, P. A. Albouy, M. Laridjani, E. J. Oh, Y. Min, A. G. MacDiarmid, J. Tsukamoto, T. Ishiguro, A. J. Epstein, *Synth. Met.*, **1994**, *65*, 131.
- [30] Z. H. Wang, E. M. Scherr, A. G. MacDiarmid, A. J. Epstein, *Phys. Rev. B*, **1992**, *45*, 4190.
- [31] R. Menon, C. O. Yoon, D. Moses, A. J. Heeger, Y. Cao, *Phys. Rev. B*, **1993**, *48*, 17685.
- [32] R. Menon, C. O. Yoon, D. Moses, A. J. Heeger, in Handbook of Conducting Polymers, 2nd edition (Ed: T. A. Skotheim, R. L. Elsenbaumer, J. R. Reynolds, Dekker, New York 1998).
- [33] C. O. Yoon, R. Menon, D. Moses, A. J. Heeger, *Phys. Rev. B*, **1994**, *49*, 10851.
- [34] Y. Chang, K. Lee, R. Kiebooms, A. Aleshin, A. J. Heeger, *Synth. Met.*, **1999**, *105*, 203.
- [35] A. Raghunathan, G. Rangarajan, D. C. Trivedi, *Synth. Met.*, **1996**, *81*, 39.
- [36] C. Lee, Y. H. Seo, S. H. Lee, *Macromolecules*, **2004**, *37*, 4070.
- [37] R. Gangopadhyay, A. De, *Chem. Mater.*, **2000**, *12*, 608.

- [38] J. Li, H. Xie, Y. Li, J. Liu, Z. Li, *J. Power Source*, **2011**, 196, 10775.
- [39] Y. Li, X. Zhao, Q. Xu, Q. Zhang, D. Chen, *Langmuir*, **2011**, 27, 6458.
- [40] J. Yan, T. Wei, B. Shao, Z. Fan, W. Qian, M. Zhang, F. Wei, *Carbon*, **2010**, 48, 487.
- [41] S. R. Sivakkumar, W. J. Kim, J. A. Choi, D. R. MacFarlane, M. Forsyth, D. W. Kim, *J. Power Source*, **2007**, 171, 1062.
- [42] Q. Wu, Y. Xu, Z. Yao, A. Liu, G. Shi, *ACS Nano*, **2010**, 4, 1963.
- [43] K. S. Ryu, K. M. Kim, N. G. Park, Y. J. Park, S. H. Chang, *J. Power Source*, **2002**, 103, 305.
- [44] L. Li, E. Liu, J. Li, Y. Yang, H. Shen, Z. Huang, X. Xiang, W. Li, *J. Power Source*, **2010**, 195, 1561.
- [45] J. Li, J. Fang, M. Cui, H. Lu, Z. A. Zhang, Y. A. Lai, *J. Cent. South Univ. Technol*, **2011**, 18, 78.
- [46] J. Xu, K. Wang, S. Z. Zu, B. H. Han, Z. Wei, *ACS Nano*, **2010**, 4, 5019.
- [47] Y. Zhao, H. Bai, Y. Hu, Y. Li, L. Qu, S. Zhang, G. Shi, *J. Mater. Chem.*, **2011**, 21, 13978.
- [48] L. Z. Fan, Y. S. Hu, J. Maier, P. Adelhelm, B. Smarsly, M. Antonietti, *Adv. Funct. Mater.*, **2007**, 17, 3083.
- [49] L. Li, H. Song, Q. Zhang, J. Yao, X. Chen, *J. Power Sources*, **2009**, 187, 268.

- [50] Q. Liu, M. H. Nayfeh, S. T. Yau, *J. Power Sources*, **2010**, 195, 3956.
- [51] Y. Li, X. Zhao, Q. Xu, Q. Zhang, D. Chen, *Langmuir*, **2011**, 27, 6458.
- [52] G. Y. Chen, Y. H. Cheng, Y. J. Chou, M. S. Su, C. M. Chen, K. H. Wei, *Chem. Commun.*, **2011**, 47, 5064.
- [53] C. Lee, H. Yan, L. E. Brus, T. F. Heinz, J. Hone, S. Ryu, *ACS Nano*, **2010**, 4, 2695.
- [54] H. Li, Q. Zhang, C. C. R. Yap, B. K. Tay, T. H. T. Edwin, A. Olivier, D. Baillargeat, *Adv. Funct. Mater.*, **2012**, 22, 1385.
- [55] P. Sambyal, A. P. Singh, M. Verma, M. Farukh, B. P. Singh, S. K. Dhawan, *RSC Adv.*, **2014**, 4, 12614.
- [56] R. Islam, R. Chan-Yu-King, J.-F. Brun, C. Gors, A. Addad, M. Depriester, A. Hadj-Sahraoui, F. Roussel, *Nanotechnology*, **2014**, 25, 475705.
- [57] Z. Tai, X. Yan, Q. Xue, *J. Electrochem. Soc.*, **2012**, 159, A1702.
- [58] J. M. Soon, K. P. Loh, *Electrochem. Solid State Lett.*, **2007**, 10, A250.
- [59] N. A. Kumar, H.-J. Choi, Y. R. Shin, D. W. Chang, L. Dai, J.-B. Baek, *ACS Nano*, **2012**, 6, 1715.
- [60] G. Xiong, C. Meng, R. G. Reifengerger, P. P. Irazoqui, T. S. Fisher, *Energy Technol.*, **2014**, 2, 897.



- [61] L. Cao, S. Yang, W. Gao, Z. Liu, Y. Gong, L. Ma, G. Shi, S. Lei, Y. Zhang, S. Zhang, R. Vajtai, P. M. Ajayan, *Small*, **2013**, 9, 2905.
- [62] Z. Zhou, X.-F. Wu, *J. Power Sources*, **2013**, 222, 410.
- [63] A. Castellanos-Gomez, R. van Leeuwen, M. Buscema, H. S. J. van der Zant, G. A. Steele, W. J. Venstra, *Adv. Mater.*, **2013**, 25, 6719.
- [64] K. Zhang, L. L. Zhang, X. S. Zhao, J. Wu, *Chem. Mater.*, **2010**, 22, 1392.
- [65] M. Ginic-Markovic, J. G. Matison, R. Cervini, G. P. Simon, P. M. Fredericks, *Chem. Mater.*, **2006**, 18, 6258.
- [66] A. G. MacDiarmid, A. J. Epstein, *Synth. Met.*, **1994**, 65, 103.
- [67] U. J. Lee, S.-H. Lee, J. J. Yoon, S. J. Oh, S. H. Lee, J. K. Lee, *Sol. Energy Mater. Sol. Cells*, **2013**, 108, 50.
- [68] J. Zhang, J. Jiang, H. Li, X. S. Zhao, *Energy Environ. Sci.*, **2011**, 4, 4009.
- [69] H. Wang, Q. Hao, X. Yang, L. Lu, X. Wang, *Nanoscale*, **2010**, 2, 2164.
- [70] Z.-S. Wu, W. Ren, L. Gao, J. Zhao, Z. Chen, B. Liu, D. Tang, B. Yu, C. Jiang, H.-M. Cheng, *ACS Nano*, **2009**, 3, 411.
- [71] M. -I. Boyer, S. Quillard, E. Rebourt, G. Louarn, J. P. Buisson, A. Monkman, S. Lefrant, *J. Phys. Chem. B*, **1998**, 102, 7382.
- [72] M. Jain, S. Annapoorni, *Synth. Met.*, **2010**, 160, 1727.

- [73] J. E. Pereira da Silva, D. L. A. de Faria, S. I. Córdoba de Torresi, M. L. A. Temperini, *Macromolecules*, **2000**, *33*, 3077.
- [74] G. Louarn, M. Lapkowski, S. Quillard, A. Pron, J. P. Buisson, S. Lefrant, *J. Phys. Chem.*, **1996**, *100*, 6998.
- [75] G. Niaura, R. Mažeikienė, A. Malinauskas, *Synth. Met.*, **2004**, *145*, 105.
- [76] S. Bourdo, Z. Li, A. S. Biris, F. Watanabe, T. Viswanathan, I. Pavel, *Adv. Funct. Mater.*, **2008**, *18*, 432.
- [77] R. Mažeikienė, V. Tomkutė, Z. Kuodis, G. Niaura, A. Malinauskas, *Vib. Spectrosc.*, **2007**, *44*, 201.
- [78] S. Quillard, G. Louarn, S. Lefrant, A. Macdiarmid, *Phys. Rev. B*, **1994**, *50*, 12496.
- [79] A. Ray, G. E. Asturias, D. L. Kershner, A. F. Richter, A. G. MacDiarmid, A. J. Epstein, *Synth. Met.*, **1989**, *29*, 141.
- [80] K. L. Tan, E. T. Kang, K. G. Neoh, *Polym. Adv. Technol.*, **1994**, *5*, 171.
- [81] Z. Ping, *J. Chem. Soc., Faraday Trans.*, **1996**, *92*, 3063.
- [82] M. C. Bernard, A. Hugot-Le Goff, *Electrochim. Acta*, **2006**, *52*, 595.
- [83] S. Bhadra, N. K. Singha, D. Khastgir, *Polym. Int.*, **2007**, *56*, 919.
- [84] L. Dauginet-De Pra, S. Demoustier-Champagne, *Thin Solid Films*, **2005**, *479*, 321.
- [85] E. T. Kang, K. G. Neoh, K. L. Tan, *Prog. Polym. Sci.*, **1998**, *23*, 277.

- [86] A. Belmokhtar, A. Benyoucef, A. Zehhaf, A. Yahiaoui, C. Quijada, E. Morallon, *Synth. Met.*, **2012**, *162*, 1864.
- [87] A. Meneguzzi, M. C. Pham, J.-C. Lacroix, B. Piro, A. Adenier, C. A. Ferreira, P.-C. Lacaze, *J. Electrochem. Soc.*, **2001**, *148*, B121.
- [88] J. P. Pouget, M. E. Jozefowicz, A. J. Epstein, X. Tang, A. G. MacDiarmid, *Macromolecules*, **1991**, *24*, 779.
- [89] Z. Luo, X. Ma, D. Yang, L. Yuwen, X. Zhu, L. Weng, L. Wang, *Carbon*, **2013**, *57*, 470.
- [90] H.-W. Park, T. Kim, J. Huh, M. Kang, J. E. Lee, H. Yoon, *ACS Nano*, **2012**, *6*, 7624.
- [91] X. Yan, J. Chen, J. Yang, Q. Xue, P. Miele, *ACS Appl. Mater. Interfaces*, **2010**, *2*, 2521.
- [92] Y. Zhao, H. Bai, Y. Hu, Y. Li, L. Qu, S. Zhang, G. Shi, *J. Mater. Chem.*, **2011**, *21*, 13978.
- [93] J. Yan, T. Wei, Z. Fan, W. Qian, M. Zhang, X. Shen, F. Wei, *J. Power Sources*, **2010**, *195*, 3041.
- [94] X. Lu, H. Dou, S. Yang, L. Hao, L. Zhang, L. Shen, F. Zhang, X. Zhang, *Electrochim. Acta*, **2011**, *56*, 9224.
- [95] M. D. Stoller, S. Park, Y. Zhu, J. An, R. S. Ruoff, *Nano Lett.*, **2008**, *8*, 3498.

- [96] H. Mi, X. Zhang, X. Ye, S. Yang, *J. Power Sources*, **2008**, 176, 403.
- [97] B. C. Kim, J. S. Kwon, J. M. Ko, J. H. Park, C. O. Too, G. G. Wallace, *Synth. Met.*, **2010**, 160, 94.
- [98] X.-M. Feng, R.-M. Li, Y.-W. Ma, R.-F. Chen, N.-E. Shi, Q.-L. Fan, W. Huang, *Adv. Funct. Mater.*, **2011**, 21, 2989.
- [99] H. J. Park, J. Meyer, S. Roth, V. Skákalová, *Carbon*, **2010**, 48, 1088.
- [100] L. Li, A. -R. O. Raji, H. Fei, Y. Yang, E. L. G. Samuel, J. M. Tour, *ACS Appl. Mater. Interfaces*, **2013**, 5, 6622.
- [101] J. Cho, K.-H. Shin, J. Jang, *Synth. Met.*, **2010**, 160, 1119.
- [102] H. Yoon, M. Chang, J. Jang, *Adv. Funct. Mater.*, **2007**, 17, 431.